

Image from [www.imdb.com/title/tt0298814/](http://www.imdb.com/title/tt0298814/)

# THE CORE

In view of all the uncertainties of these comparisons, either by extrapolation from high pressures to low, or from low to high, a discrepancy of 10 to 20 per cent can hardly be said to condemn the hypothesis of the iron core, especially when the density appears to be slightly smaller than we expect for iron. While it is difficult to find enough heavy elements in the cosmic chemistry to account for a density substantially greater than that of iron, any of the most abundant elements will reduce the density of iron. The effects of carbon and silicon are perhaps the most familiar, a reduction of density by 10 per cent requiring only small percentages of these elements.

Some of the recent proposals concerning the core have been considered. Ramsey's theory of a metallic phase of a magnesian silicate is rejected, as is Bullen's suggestion of an appreciable concentration of heavy elements in the inner core. New support has been found for the classical idea of a predominantly iron core, although alloying with lighter elements, conceivably including metallic hydrogen, may be required for layer *E*. The properties of the inner core are consistent with the predicted properties of crystalline iron, and there seems to be no reason to imagine a central density greater than about 15.

# CORE PHYSICS

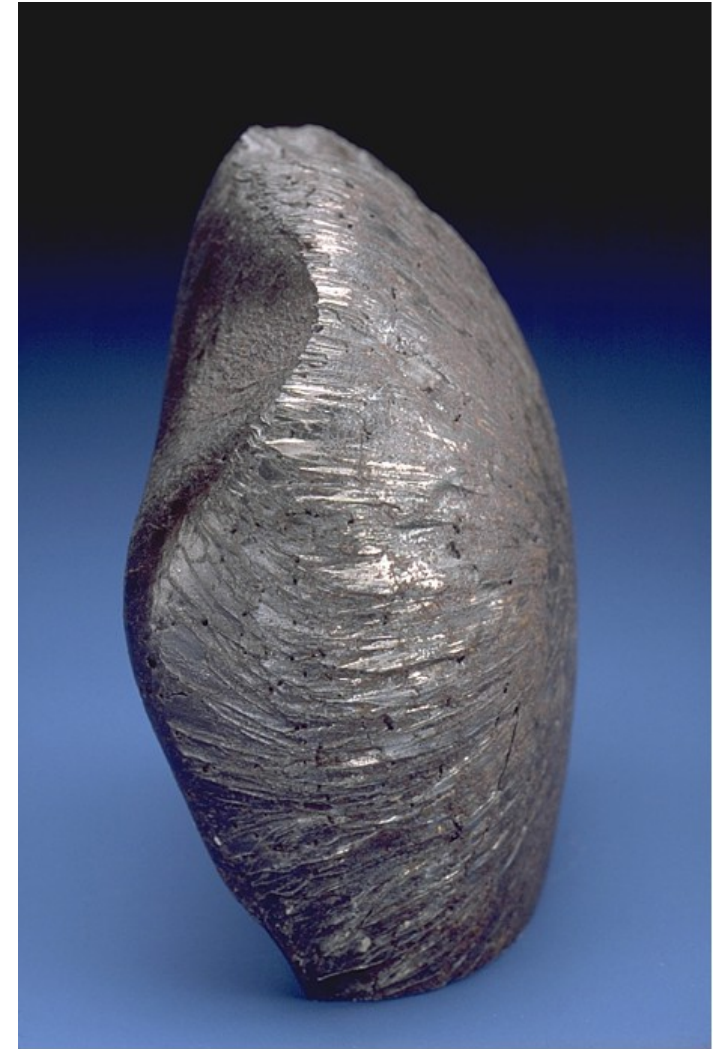


Image from Glatzmaier & Roberts, *Nature*, 1995

# EARTH AS A DIFFERENTIATED BODY



<http://meteorites.asu.edu/wp-content/uploads/henbury-big.jpg>



Grosvenor meteorite  
<http://mineralsciences.si.edu/captions/grosvenor.htm>

## **The Constitution of the Interior of the Earth, as Revealed by Earthquakes**

“Many theories of the earth have been propounded at different times: the central substance of the earth has been supposed to be fiery, fluid, solid and gaseous in turn, till geologists have turned in despair from the subject, and become inclined to confine their attention to the outermost crust of the earth, leaving its centre as a playground for mathematicians.”

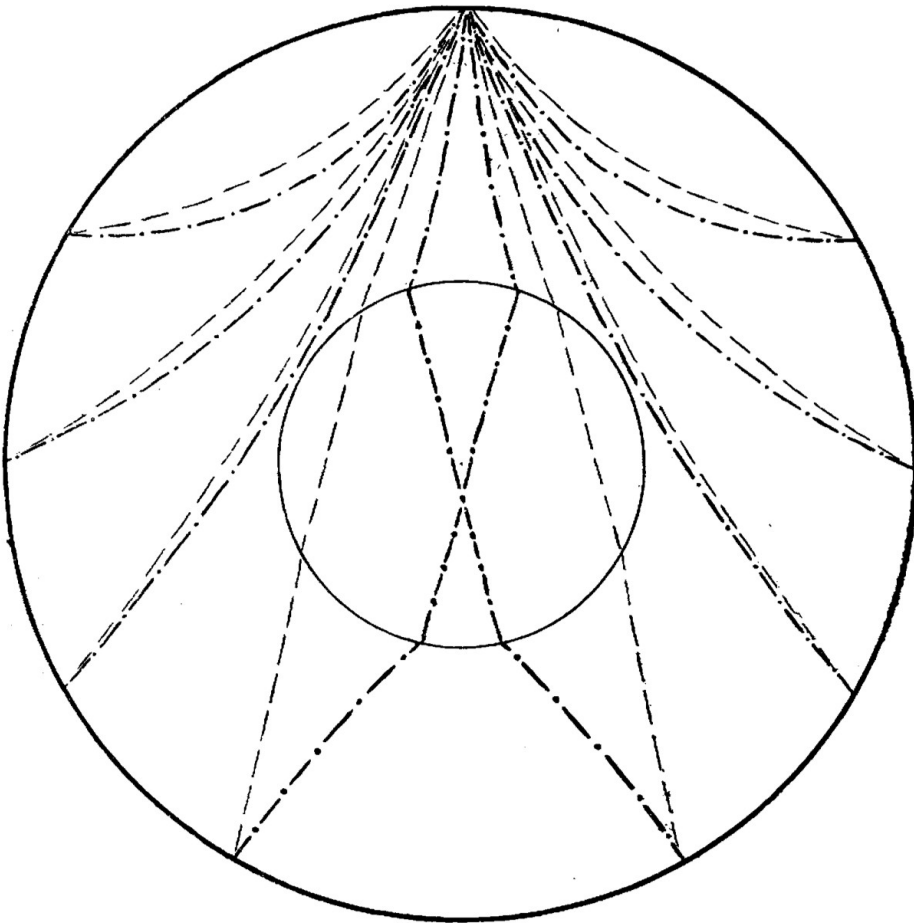
Oldham,

Quarterly Journal of the Geological Society 1906



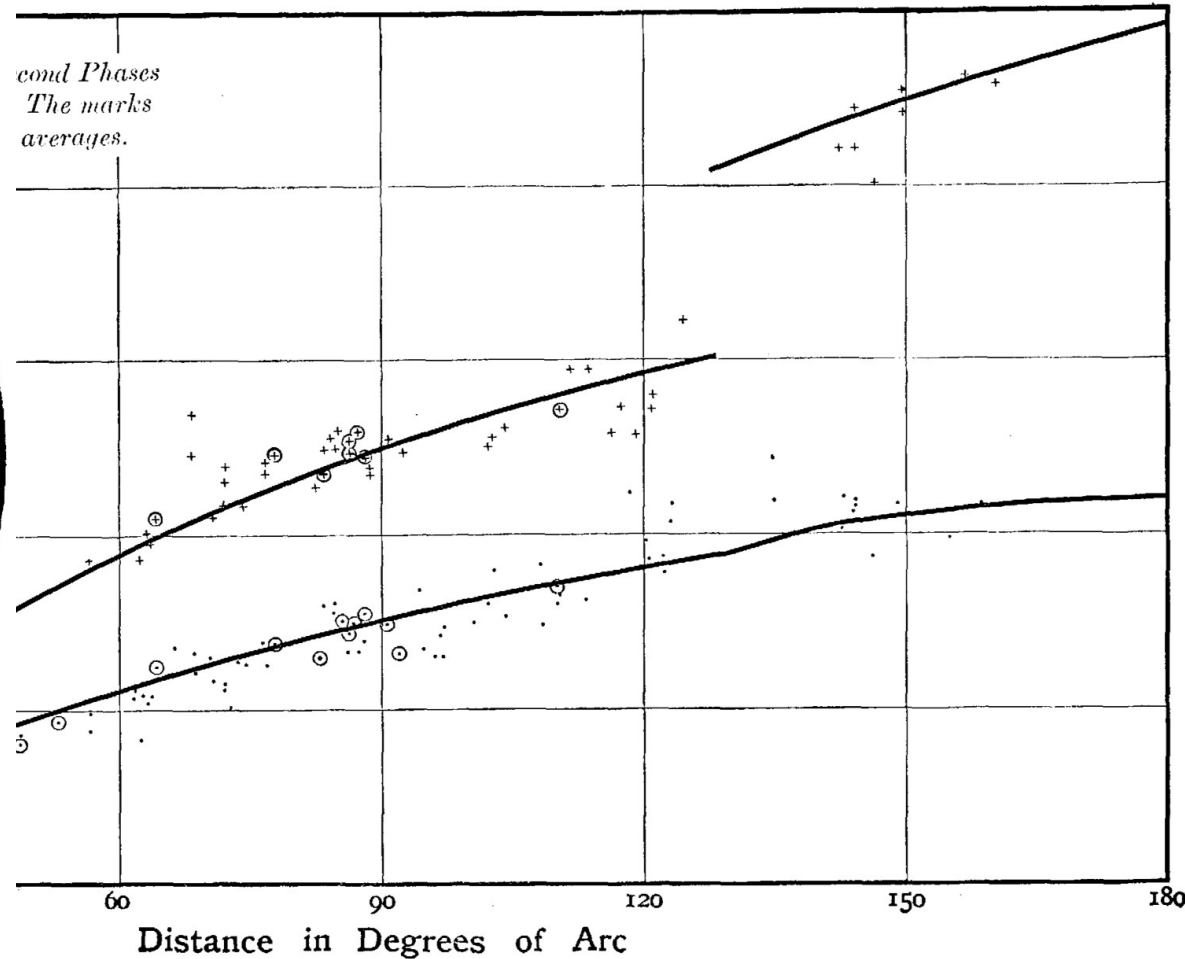
# THERE'S A CORE DOWN THERE?!

Fig. 3.



[The broken lines represent the first phase, the broken-and-dotted lines the second phase, and the continuous curve the third phase.]

Fig. 1.



Core radius  $\sim 0.4r_e$

# THERE'S A CORE DOWN THERE

Thanks to Juliane and Rene for translation assistance!

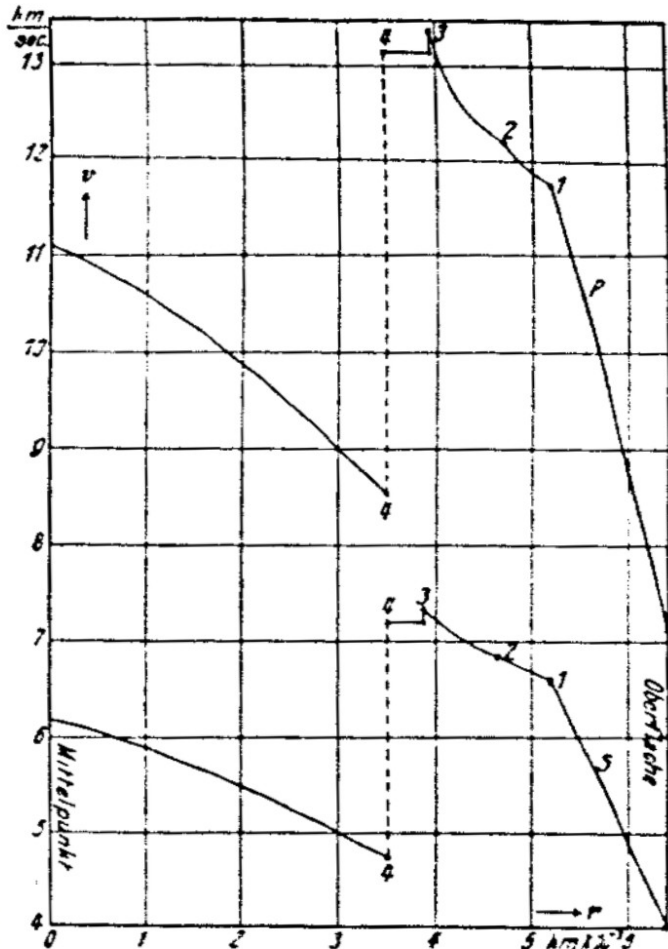
Über die Konstitution des Erdinnern, erschlossen aus Erdbebenbeobachtungen.

Von B. Gutenberg.<sup>1)</sup>



1913, Physik. Zeitschr.

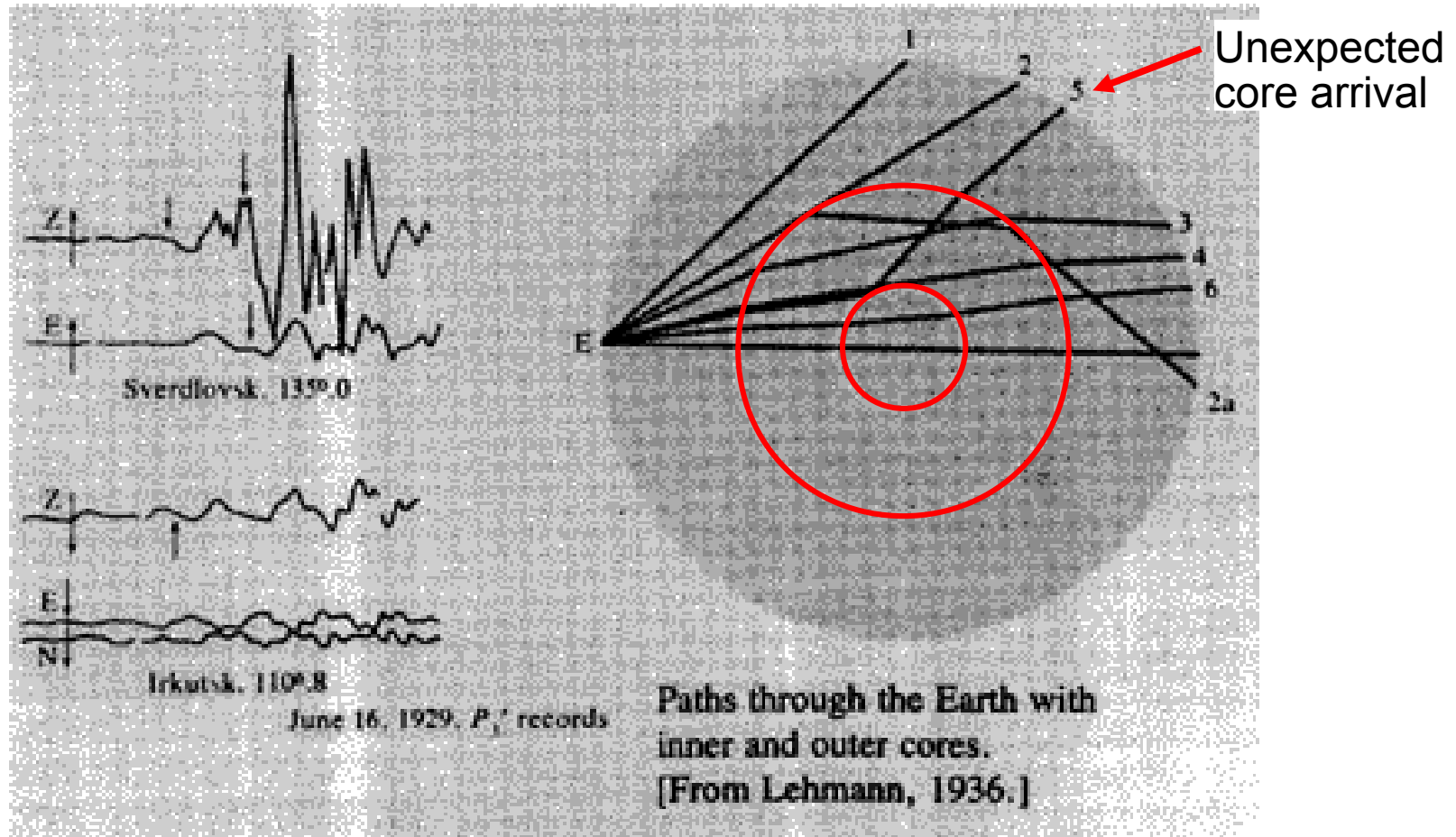
- Core radius ~ 3500km. (PREM has  $r_{\text{CMB}} = 3480$ )
- Due to velocity profile, expects to see phases like SKS.



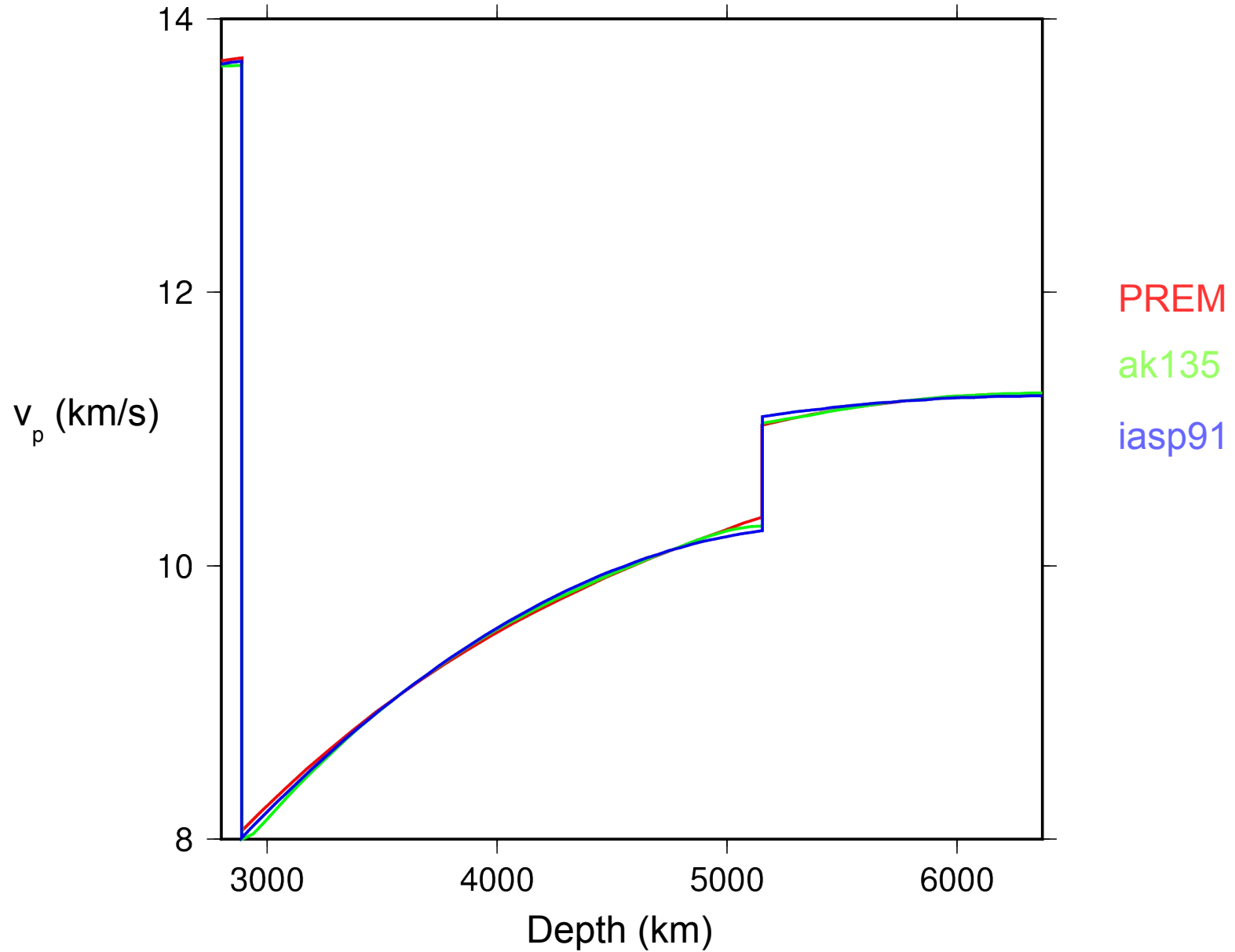
“There seems to be no reason to deny that the earth's metallic core is truly fluid.”

Jeffreys, 1926,  
Monthly notices of the RAS

# THERE'S AN INNER CORE DOWN THERE

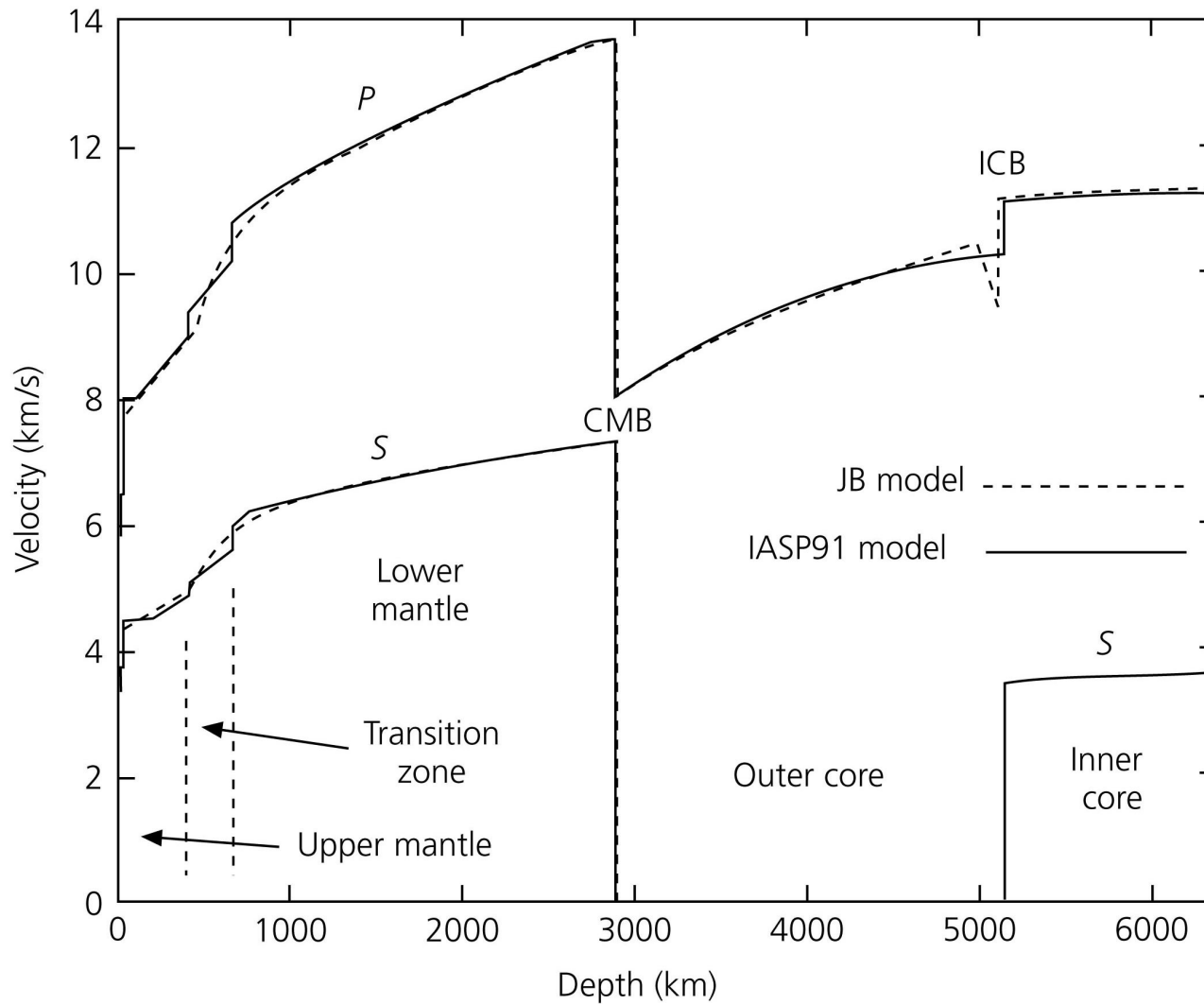


# THE CORE

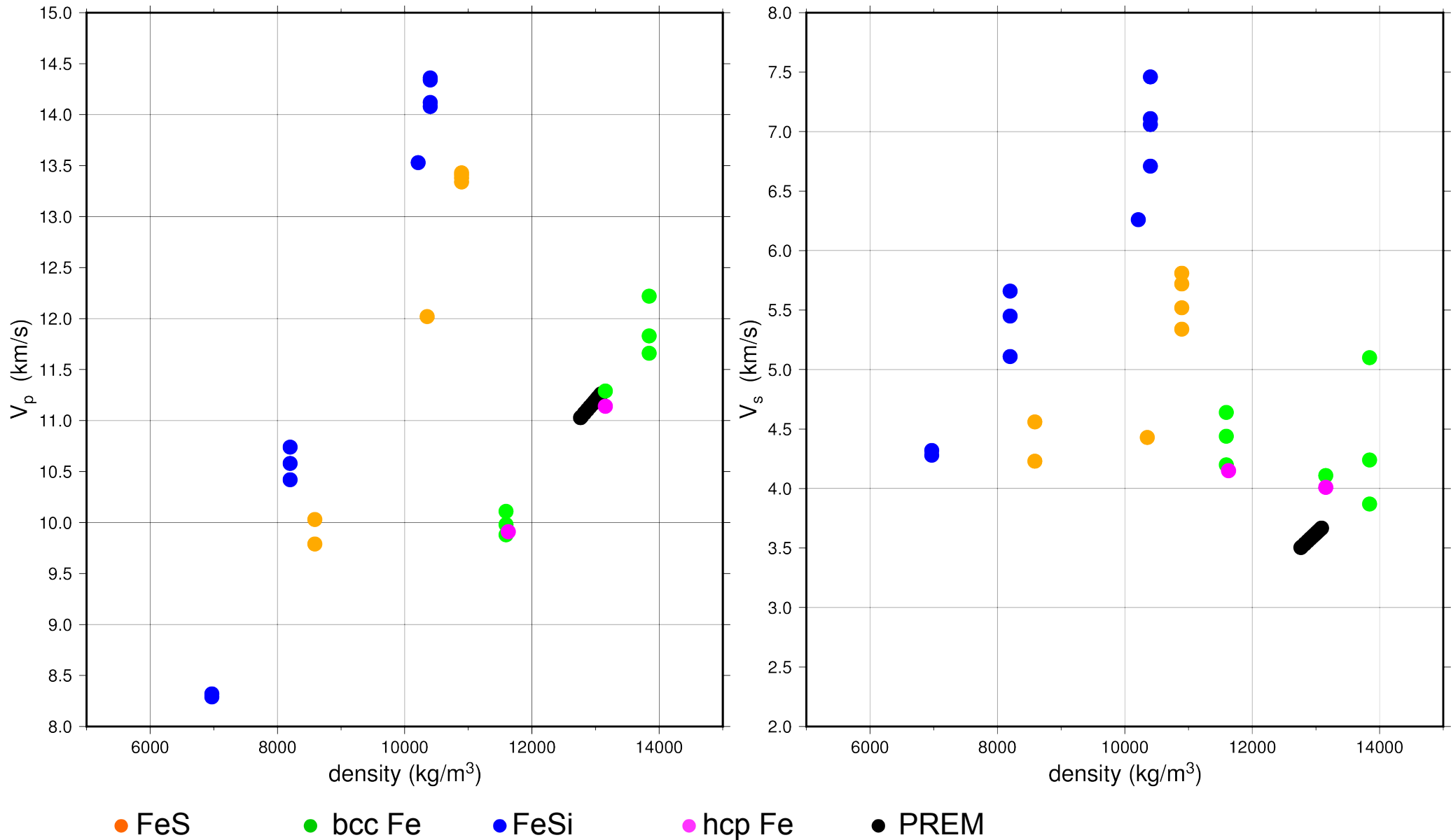


# THE CORE

**Figure 3.5-1: Comparison of the J-B and IASP91 earth models.**



# THE CORE



# THE OUTER CORE (BRIEF DETOUR)

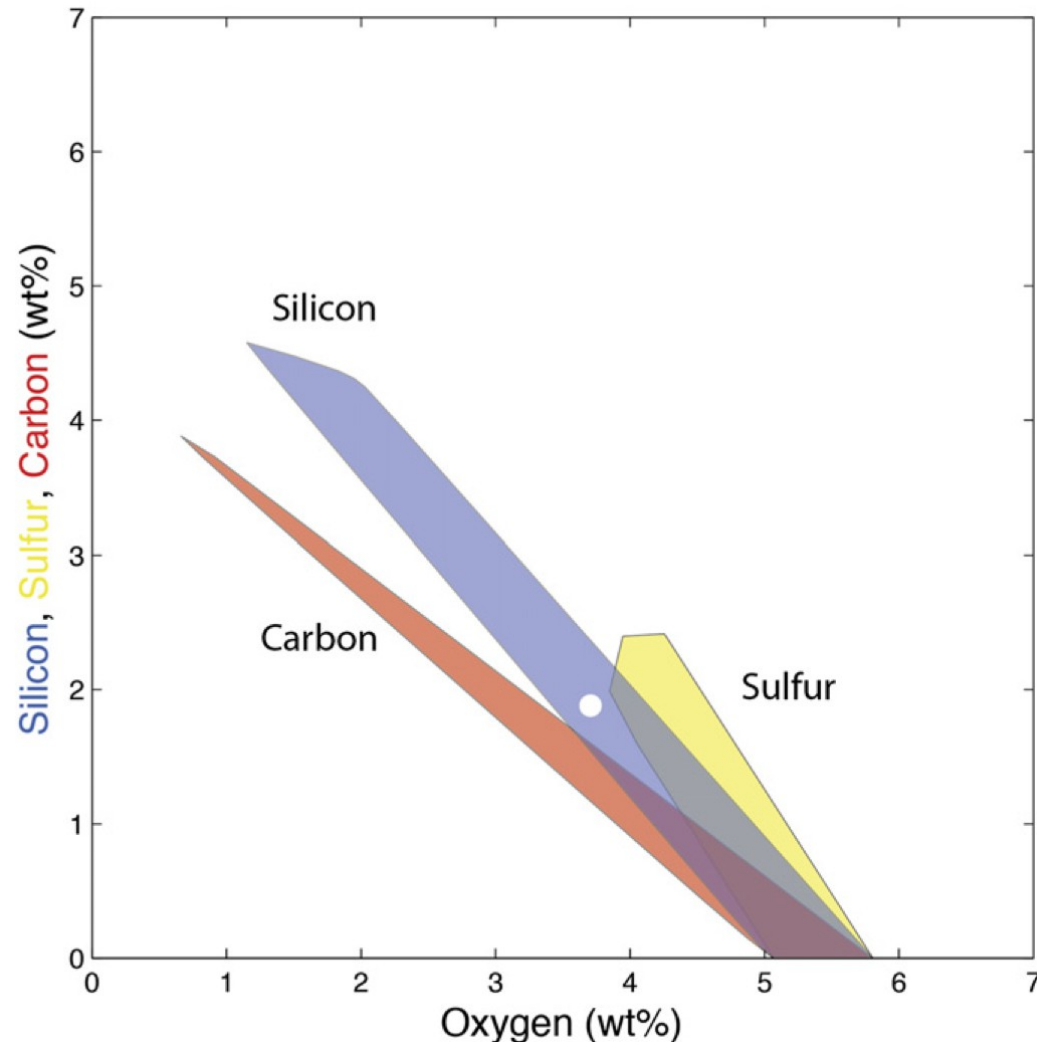
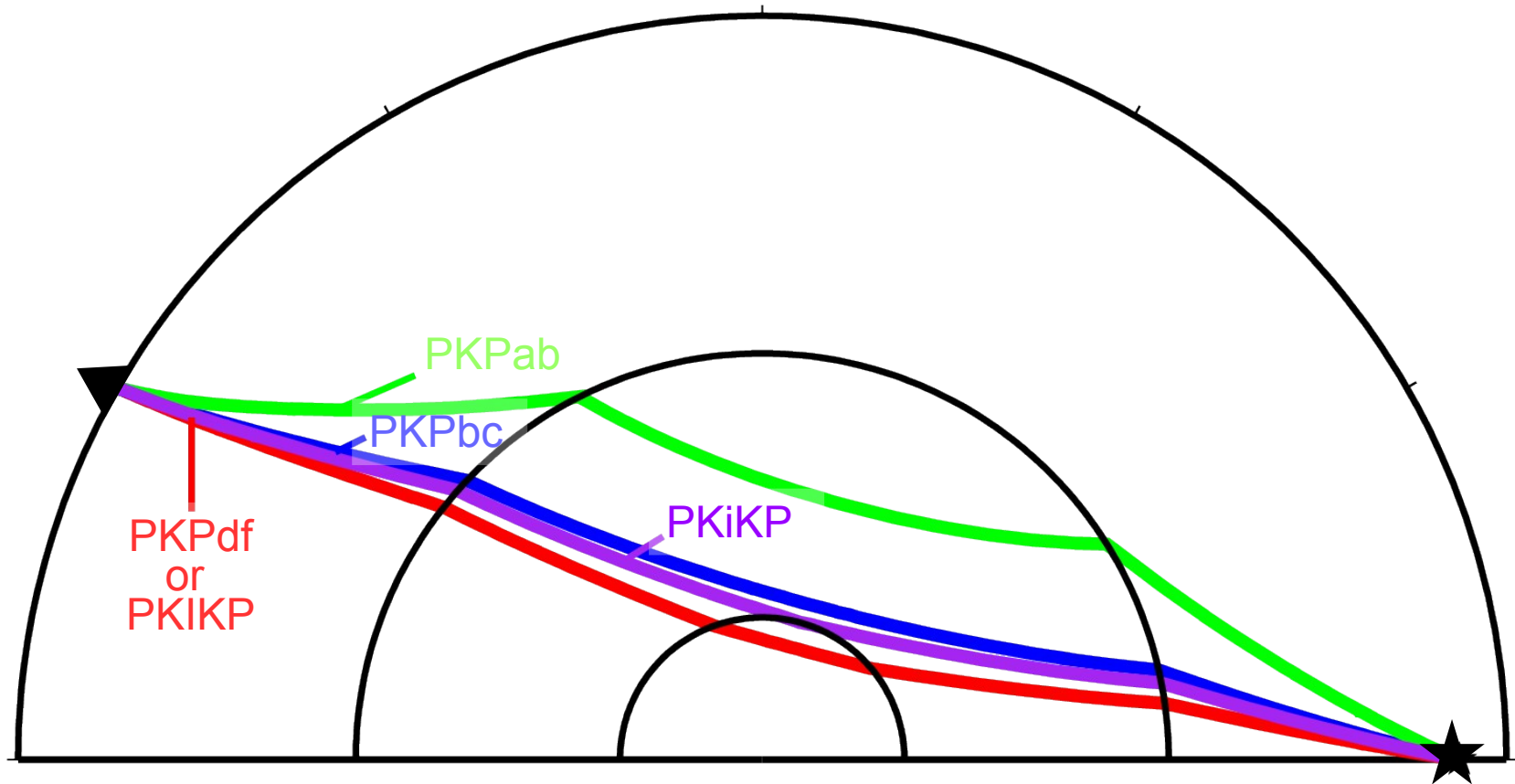
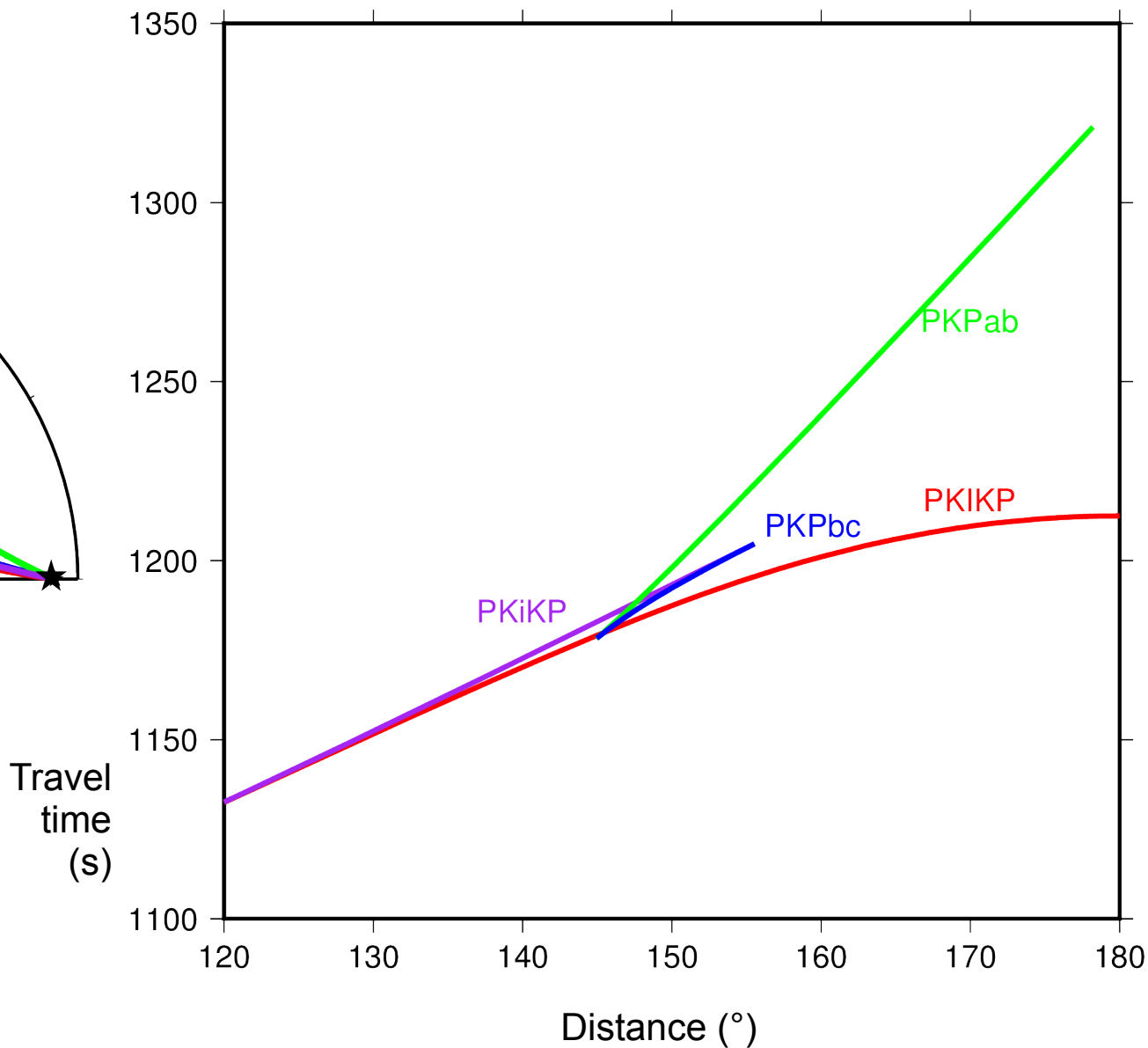
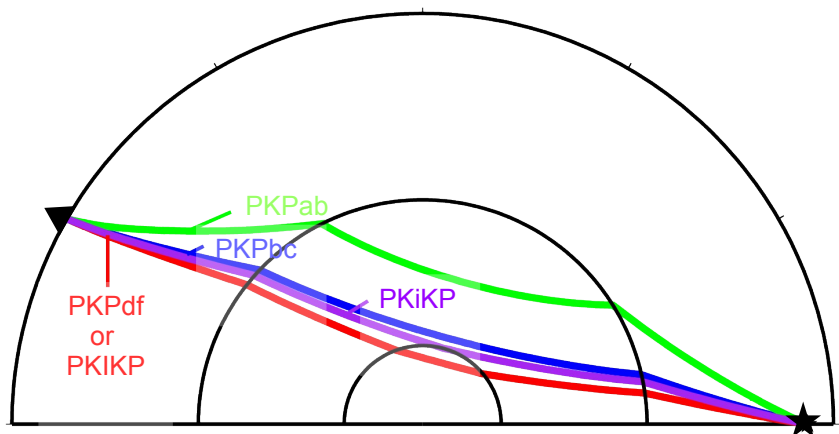


Fig 2. Range of core compositions compatible with seismic observations. Each shaded area represents the ternary solution space that satisfies the seismic density and bulk sound velocity at the top and bottom of the outer core ( $\text{Fe}_{94}\text{Ni}_6\text{-O-Si}$ , blue;  $\text{Fe}_{94}\text{Ni}_6\text{-O-C}$ , red; and  $\text{Fe}_{94}\text{Ni}_6\text{-O-S}$ , yellow). There is no solution for the other ternaries ( $\text{Fe}_{94}\text{Ni}_6\text{-Si-S}$ ,  $\text{Fe}_{94}\text{Ni}_6\text{-Si-C}$ , and  $\text{Fe}_{94}\text{Ni}_6\text{-S-C}$ ). This shows that oxygen is always required to match the seismic data. The best numerical fit is shown by the white circle corresponding to 3.7% O, 1.9% Si, 0% S, and 0% C.

# COMPRESSIONAL WAVES IN THE CORE



# COMPRESSIONAL WAVES IN THE CORE



# INNER CORE ANOMALIES

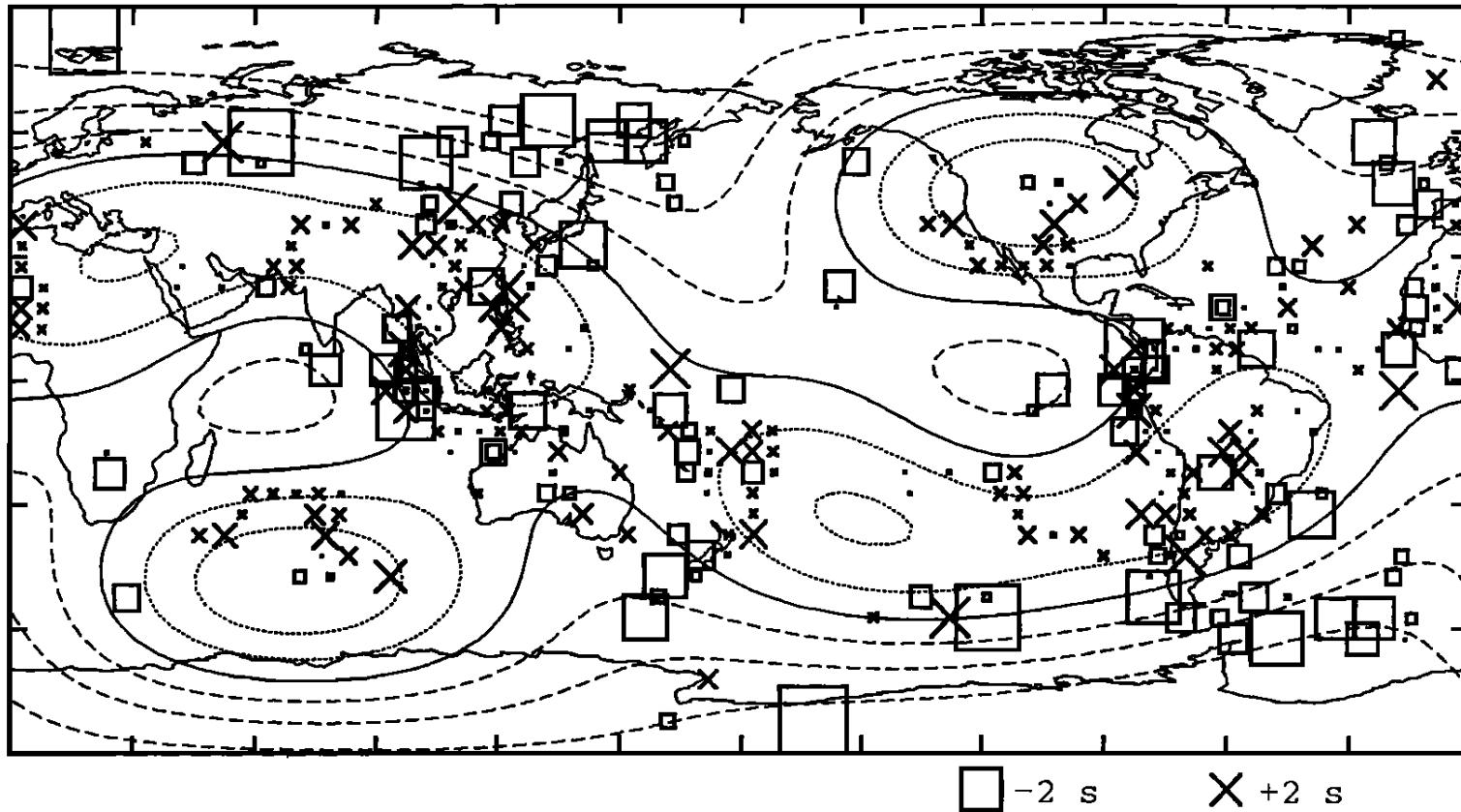


Fig. 1. Travel-time anomalies for nearly vertical rays ( $170^\circ - 180^\circ$ ) after correction for station anomalies and lower mantle and CMB structures. Each symbol is the average in a bin of a subdivision of 1654 equi-areal cells. Each residual is plotted both at the source and receiver locations. The spherical harmonic expansion truncated at degree 4 is shown by the contour lines; contour interval is 0.4 s.

# INNER CORE ANOMALIES

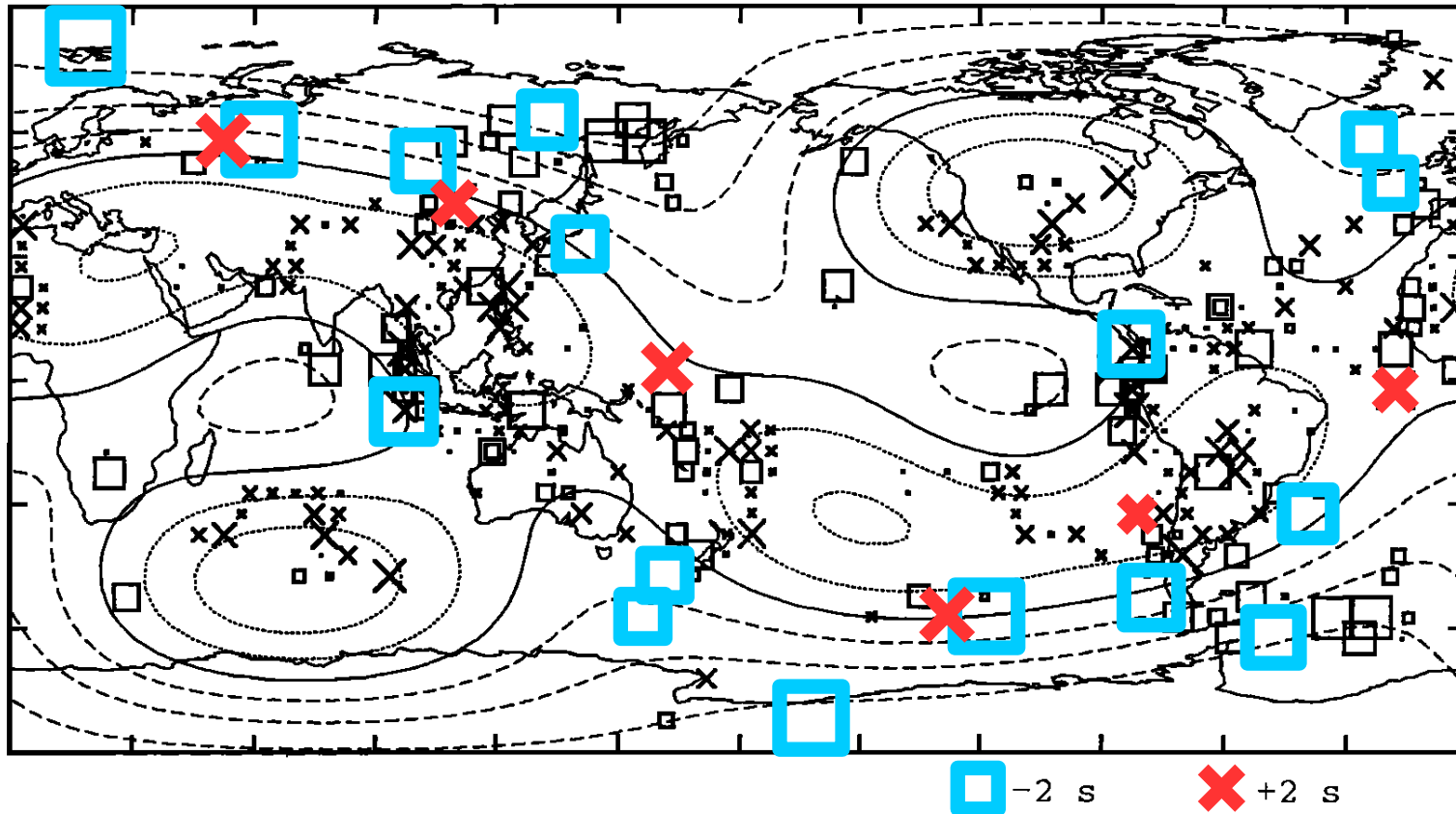


Fig. 1. Travel-time anomalies for nearly vertical rays ( $170^\circ - 180^\circ$ ) after correction for station anomalies and lower mantle and CMB structures. Each symbol is the average in a bin of a subdivision of 1654 equi-area cells. Each residual is plotted both at the source and receiver locations. The spherical harmonic expansion truncated at degree 4 is shown by the contour lines; contour interval is 0.4 s.

# INNER CORE ANOMALIES

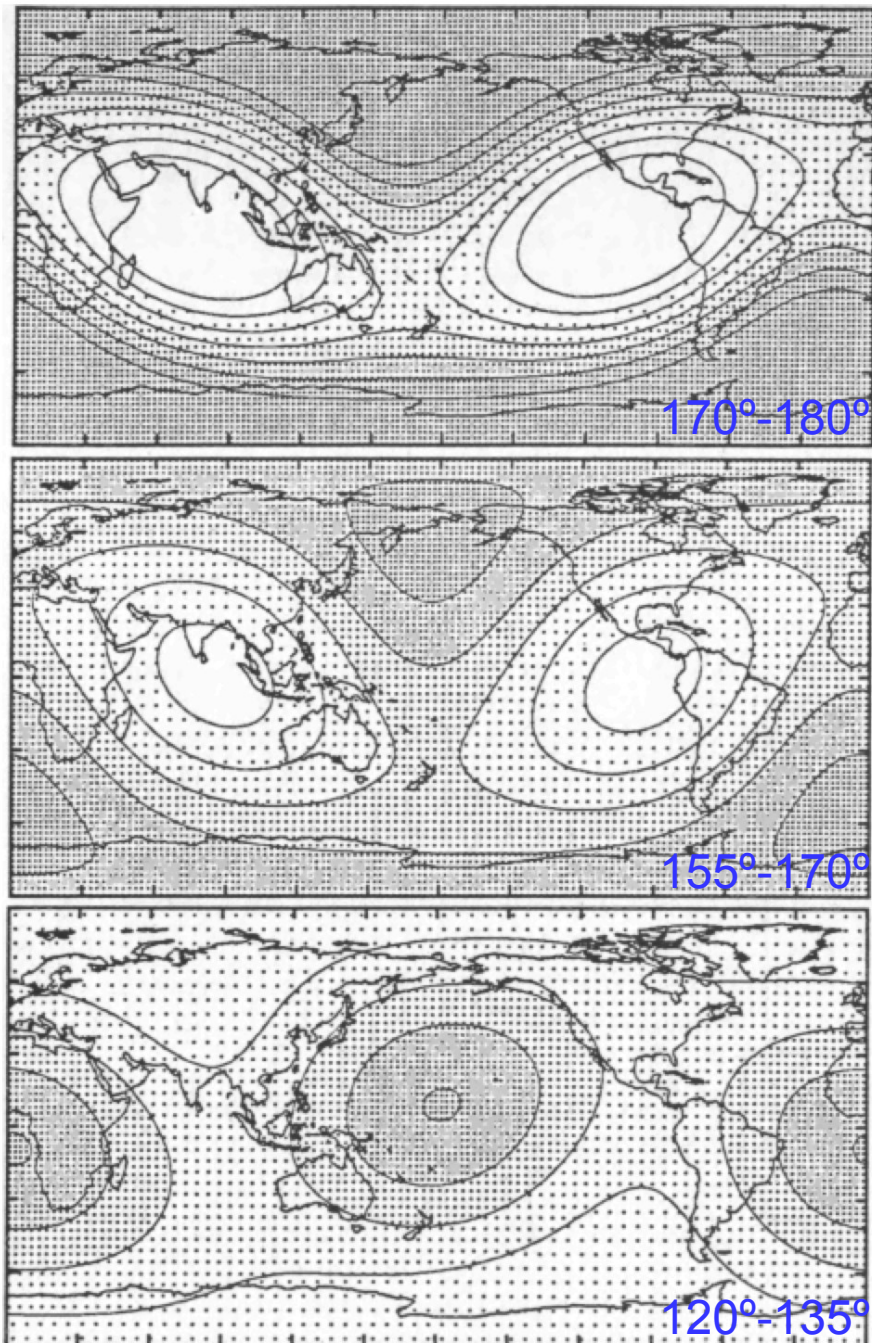


Table 1. Distance range subdivision

|    | Range       | Turning radius  | $N_{conn}$ |
|----|-------------|-----------------|------------|
| R1 | 110° – 120° | $R_{IC}$        | 2306       |
| R2 | 120° – 135° | $1200 - R_{IC}$ | 4997       |
| R3 | 135° – 155° | 880 – 1200      | –          |
| R4 | 155° – 170° | 370 – 880       | 2131       |
| R5 | 170° – 180° | 0 – 370         | 428        |

$R_{IC}$  is 1221.5 km in our model. All bottoming radii are approximate, they change slightly in different earth models. The last column ( $N_{conn}$ ) represents the number of summary connections deriving from the average of actual source-receiver paths connecting the same pair of grid cells.

Fig 2. Models for lateral heterogeneity at the top of the inner core. These patterns decrease in amplitude with depth as  $r^2$ . Only degree 2 of the expansion is shown. Top – model obtained using data from subset R5; middle – model from set R4; bottom – model from set R2. The scale is  $\pm 0.15$  km/s for all the plots to facilitate the comparison. Note that values in the top panel are by far out of scale: anomalies exceed 0.5 km/s.

-0.15km/s  +0.15km/s

# The inner core

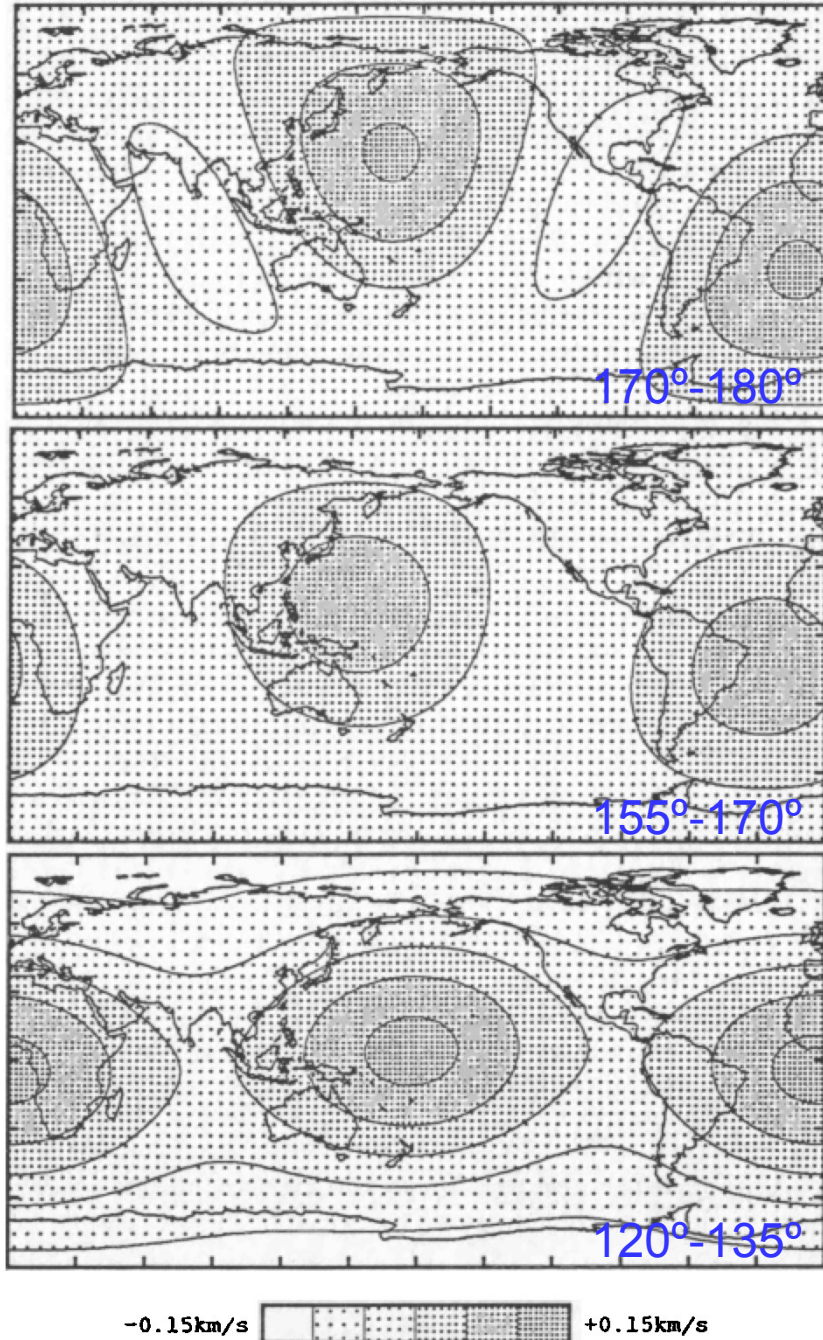
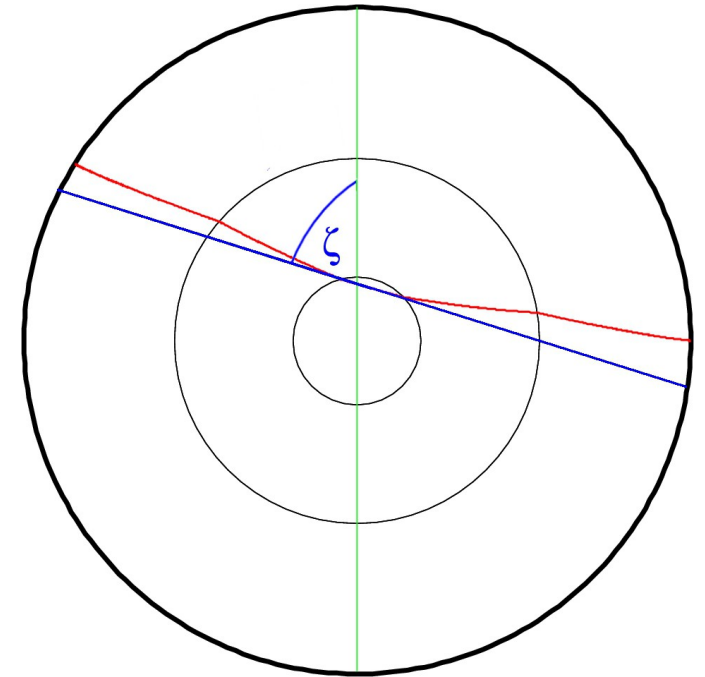
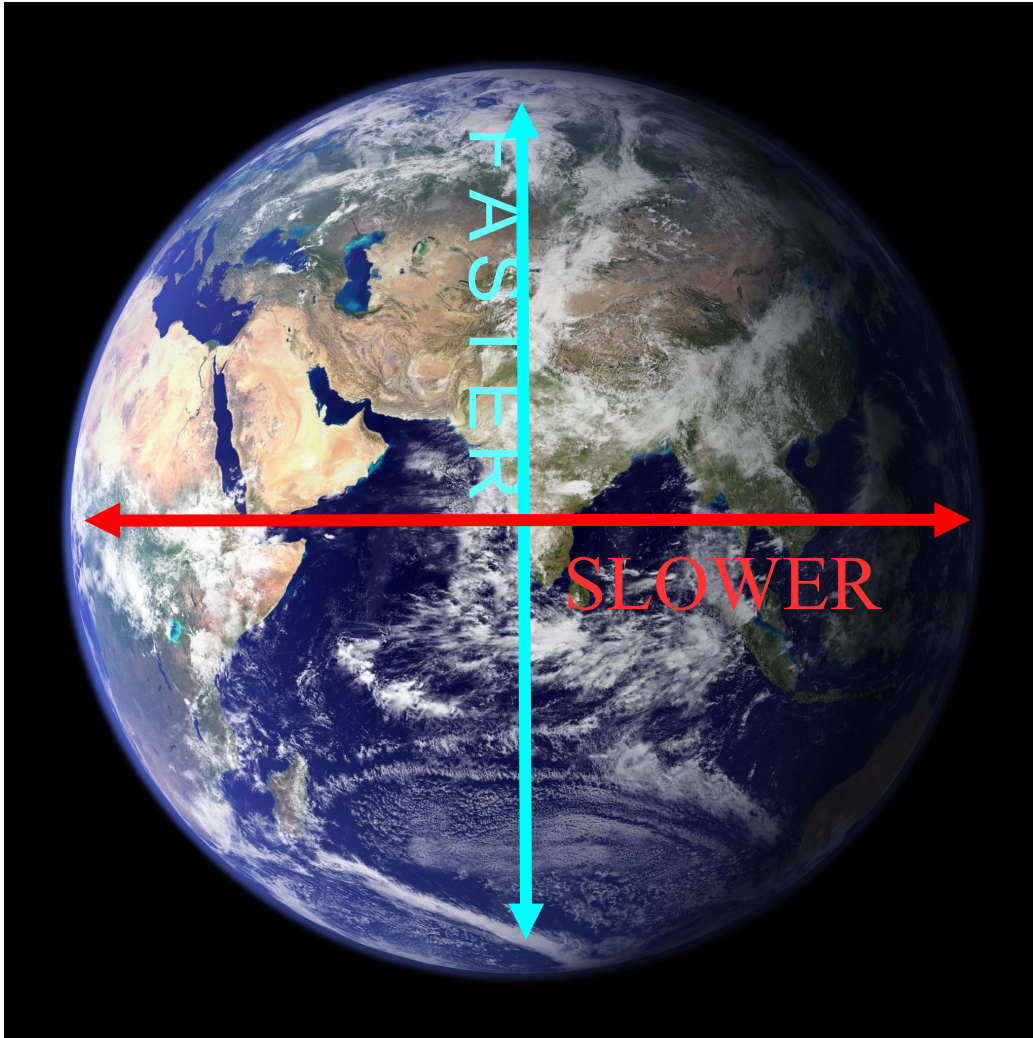


Fig. 4. Same as Figure 2, but corrected for anisotropy in the inner core. The three models, derived from the three independent datasets R5, R4 and R2, are now highly correlated.

# INNER CORE ANOMALIES



- To investigate anisotropy, use ray angle,  $\zeta$ .
- $\zeta$ : angle between the wave in the inner core and Earth's rotational axis.

# INNER CORE ANISOTROPY

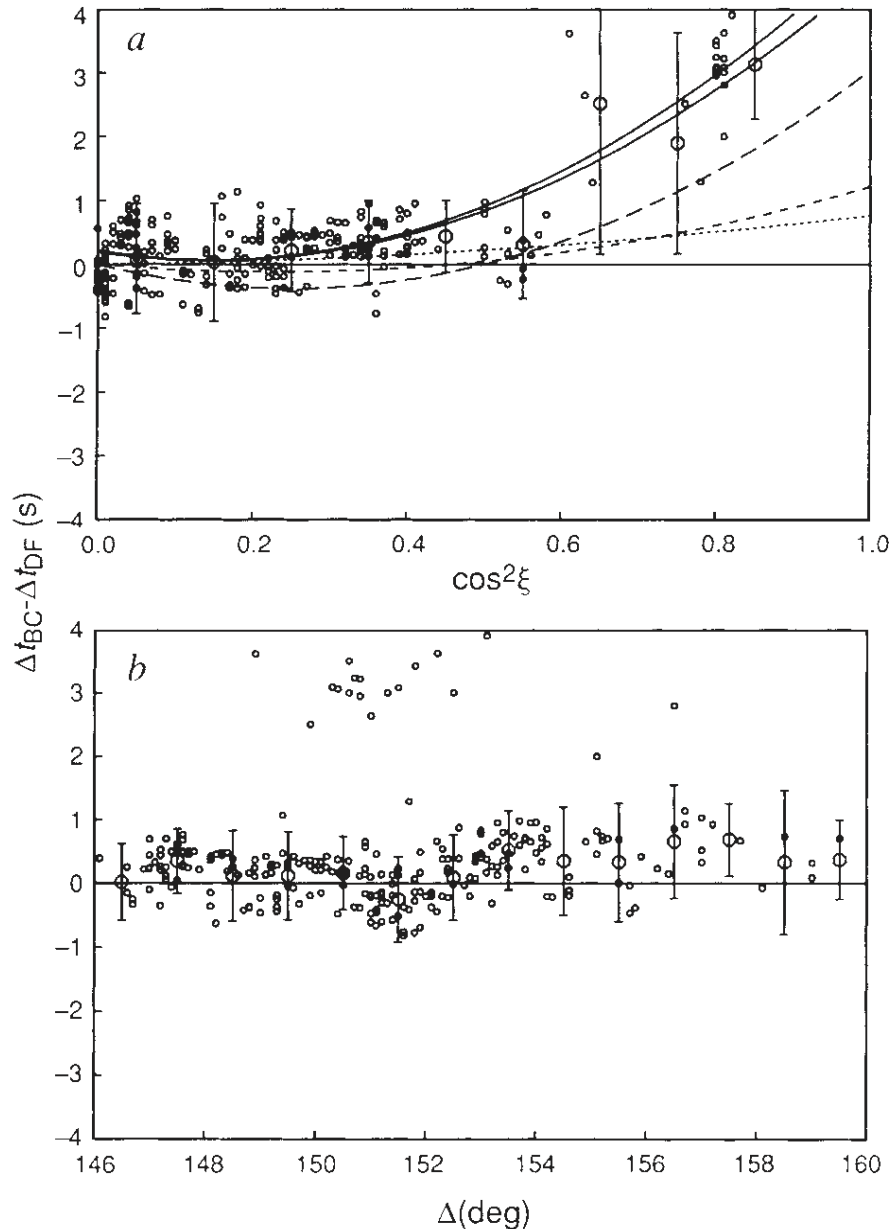


FIG. 2 Hand-picked differential travel-time residuals ( $P'_{BC} - P'_{DF}$ ) plotted with respect to  $\cos^2 \xi$  (a) and epicentral distance (b).

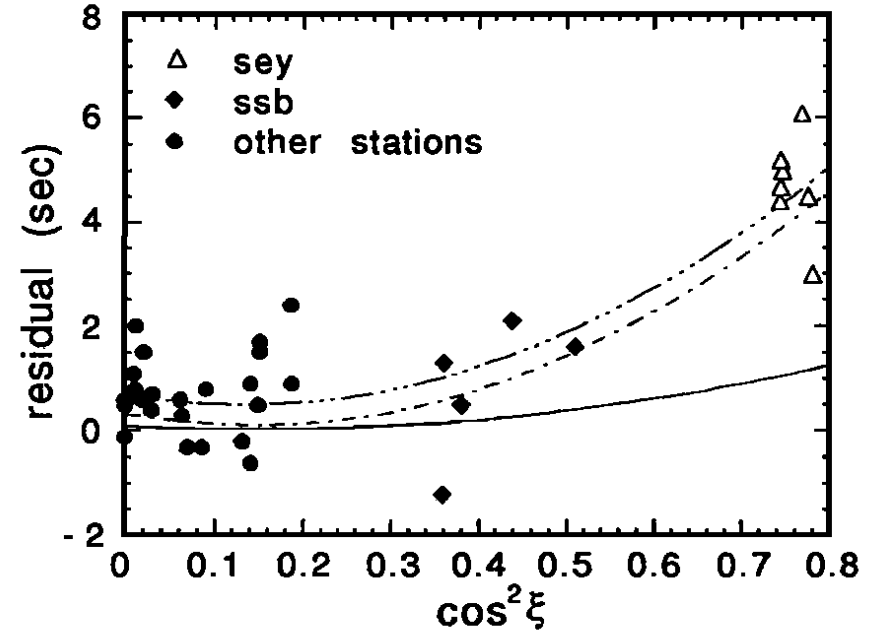
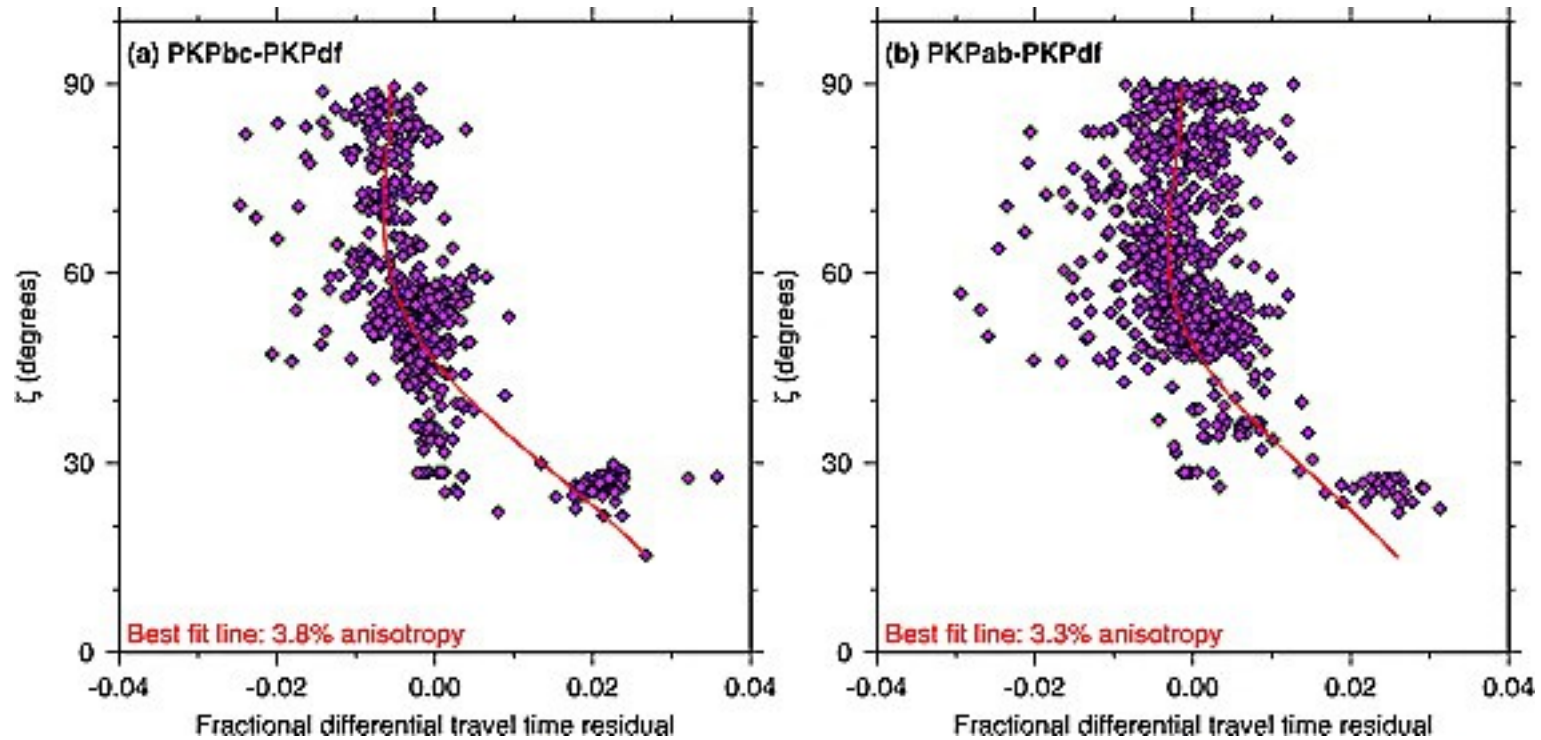


Figure 5. AB- DF residuals at epicentral distances larger than  $165^\circ$  as a function of  $\cos^2 \xi$ . The (· - ·) curve is calculated at a distance of  $172^\circ$  for Creager's (1992) uniform anisotropy model. The (— ···) curve is the same shifted upward by 0.5 sec to fit the data better. The solid line is the corresponding curve for Tromp's (1993) model.

Figure above from Vinnik et al, *Geophys. Res. Lett.*, 1994

Figures left from Creager, *Nature*, 1992

# THE INNER CORE





# THE INNER CORE

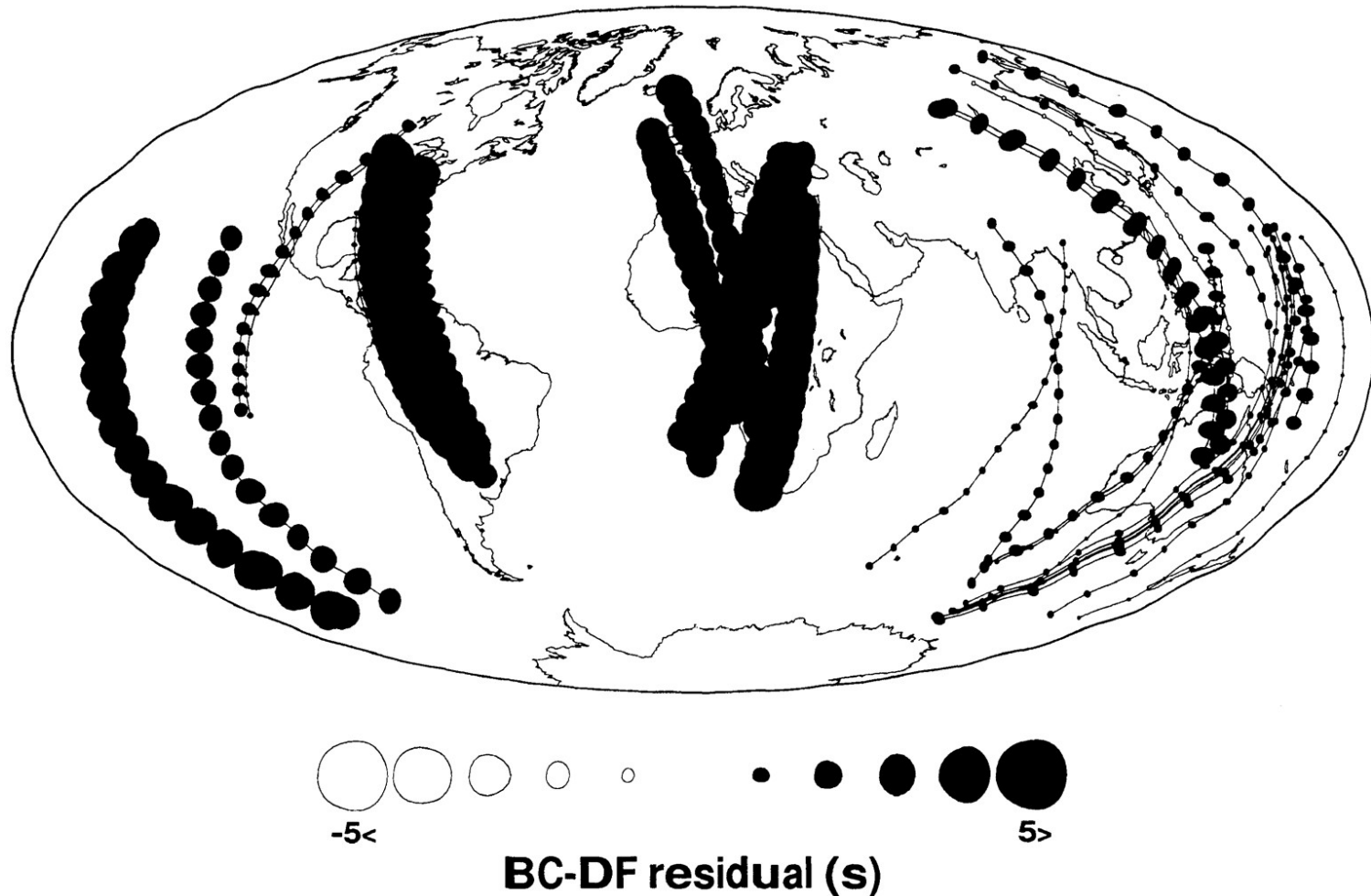
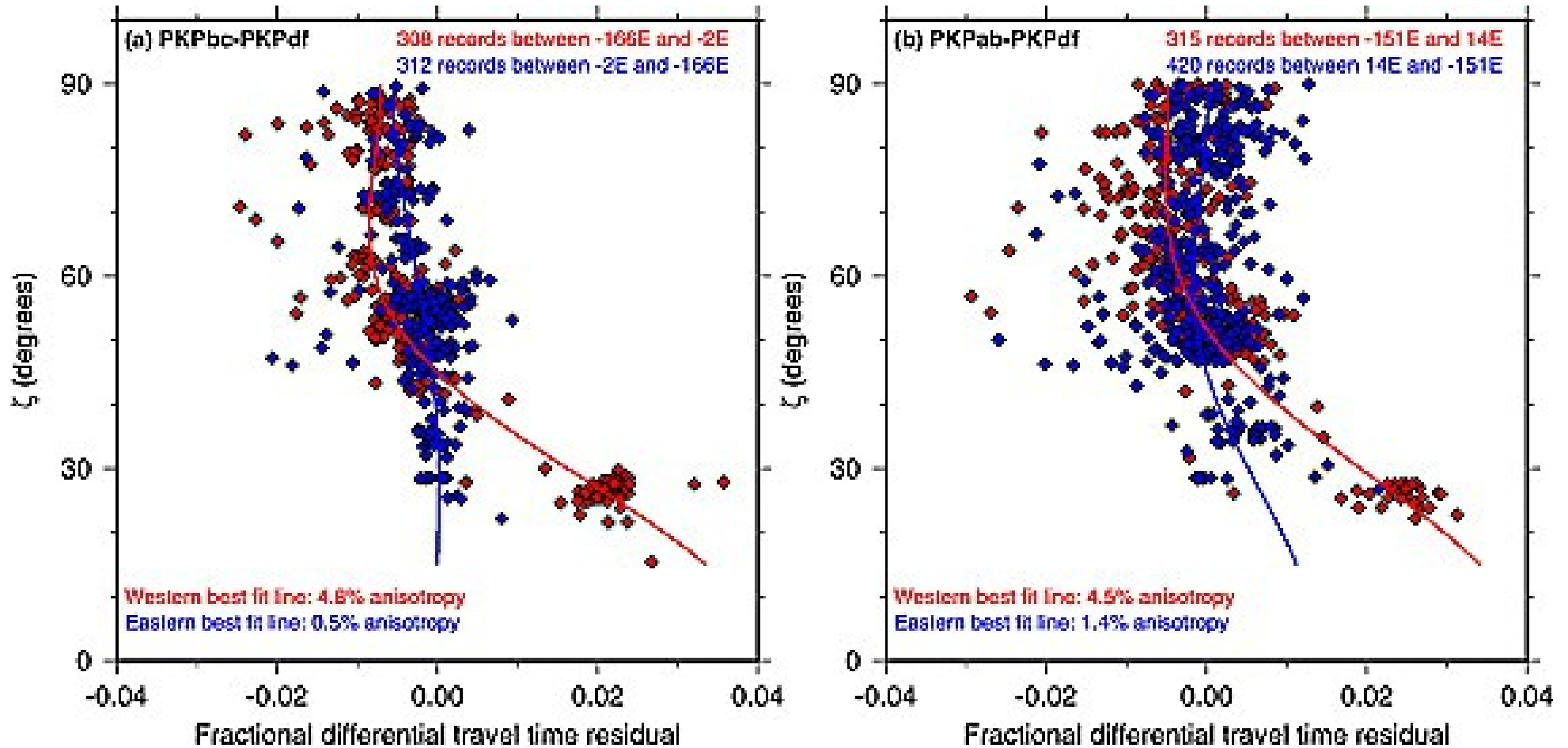
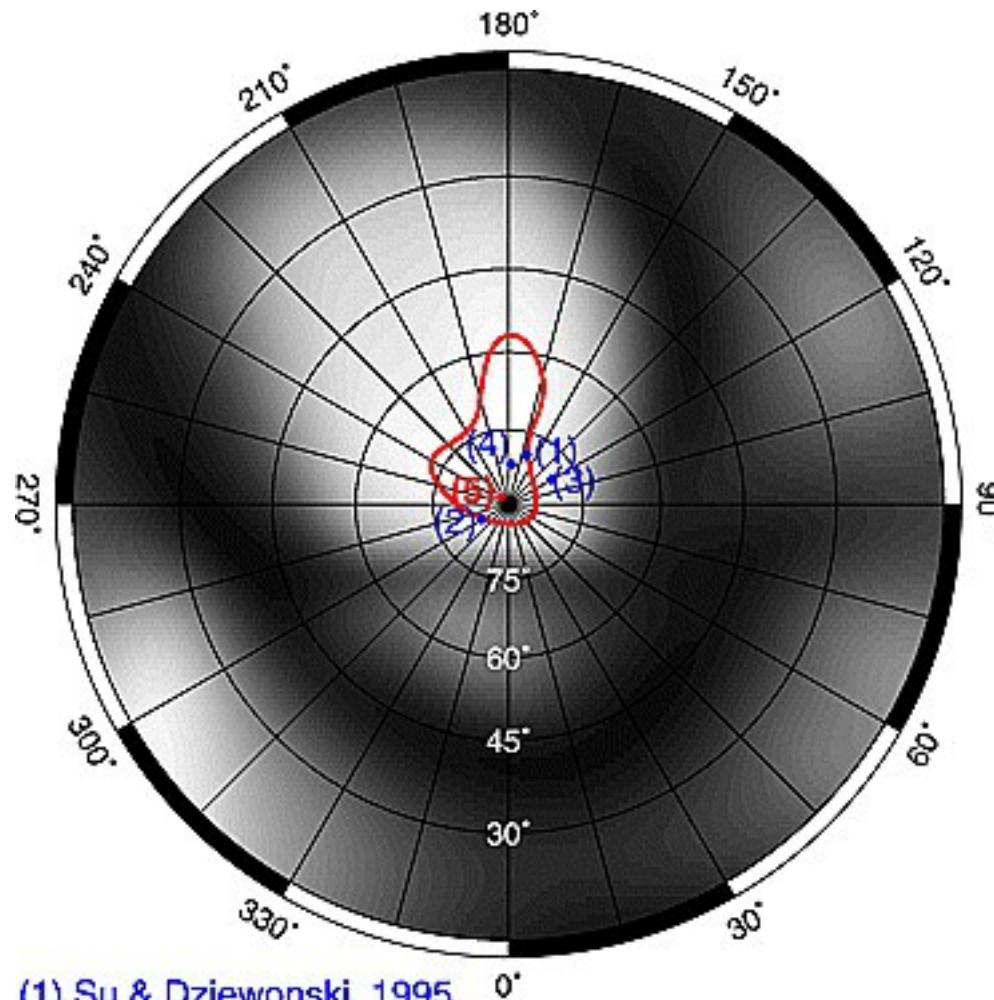


**Figure 10.** Geographical distribution of the BC–DF residuals for the polar paths. A chain of circles and lines indicate the portion of the DF ray that runs through the inner core. Solid and open circles represent positive and negative residuals, respectively. Their radii are proportional to the absolute values of the residuals. Note that the scale factor of the residuals is different from that of Figure 6. The map is a Hammer projection centered on  $(0^\circ, 0^\circ)$ .

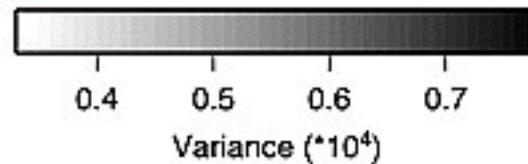
# THE INNER CORE



# THE INNER CORE



- (1) Su & Dziewonski, 1995
- (2) Shearer & Toy, 1991
- (3) McSweeney et al., 1997
- (4) Song & Richards, 1996
- (5) **This work**



# THE INNER CORE

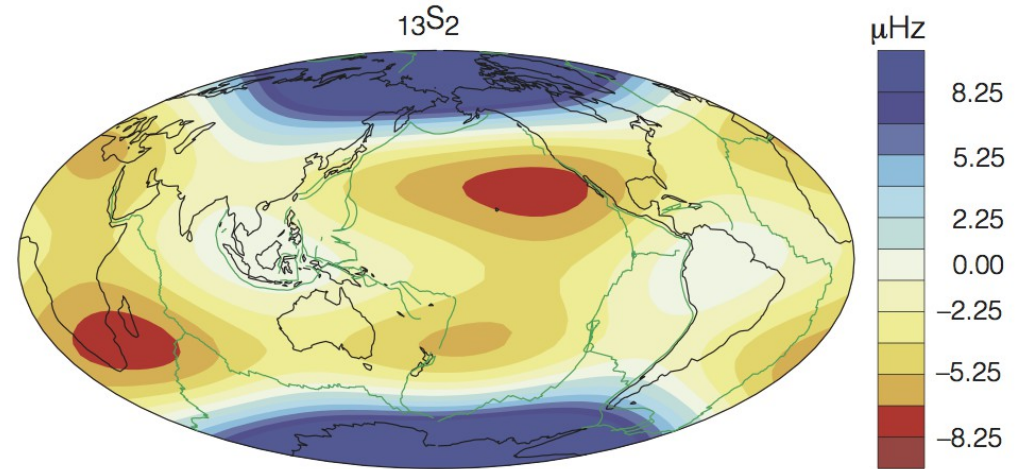
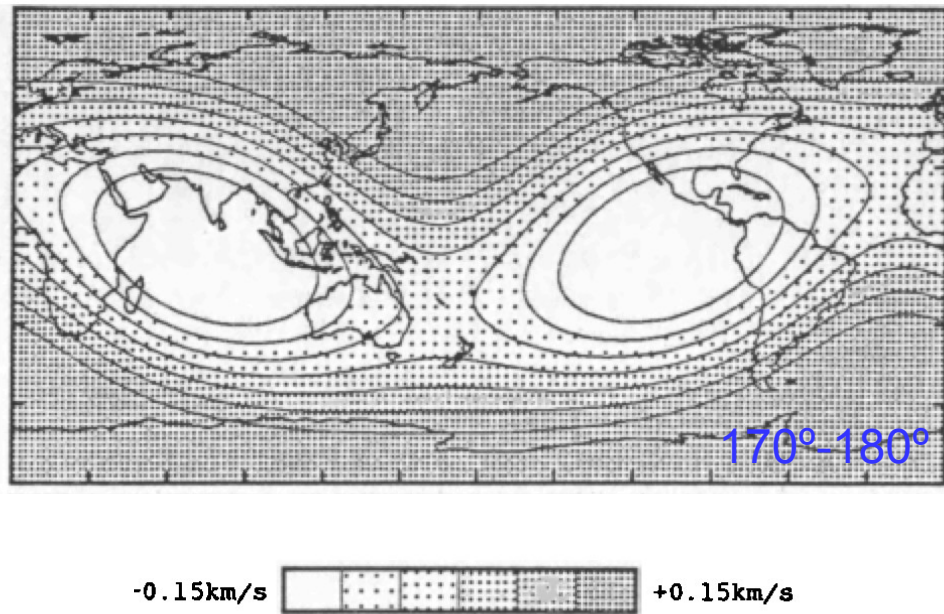


**Figure 1** Splitting functions for the two modes  $_{10}S_2$  and  $_{13}S_2$ . The effects of rotation and ellipticity have been removed before the inversion for structure coefficients (equation (2)). The splitting functions are very robust and the non-zonal patterns are very well aligned.

**Giardini *et al.* (1986); see Woodhouse *et al.* (this issue).**

# Modes and the inner core

Inner core anisotropy causes splitting of core sensitive modes. See the introduction to splitting in Seismology 2: Introduction to normal modes

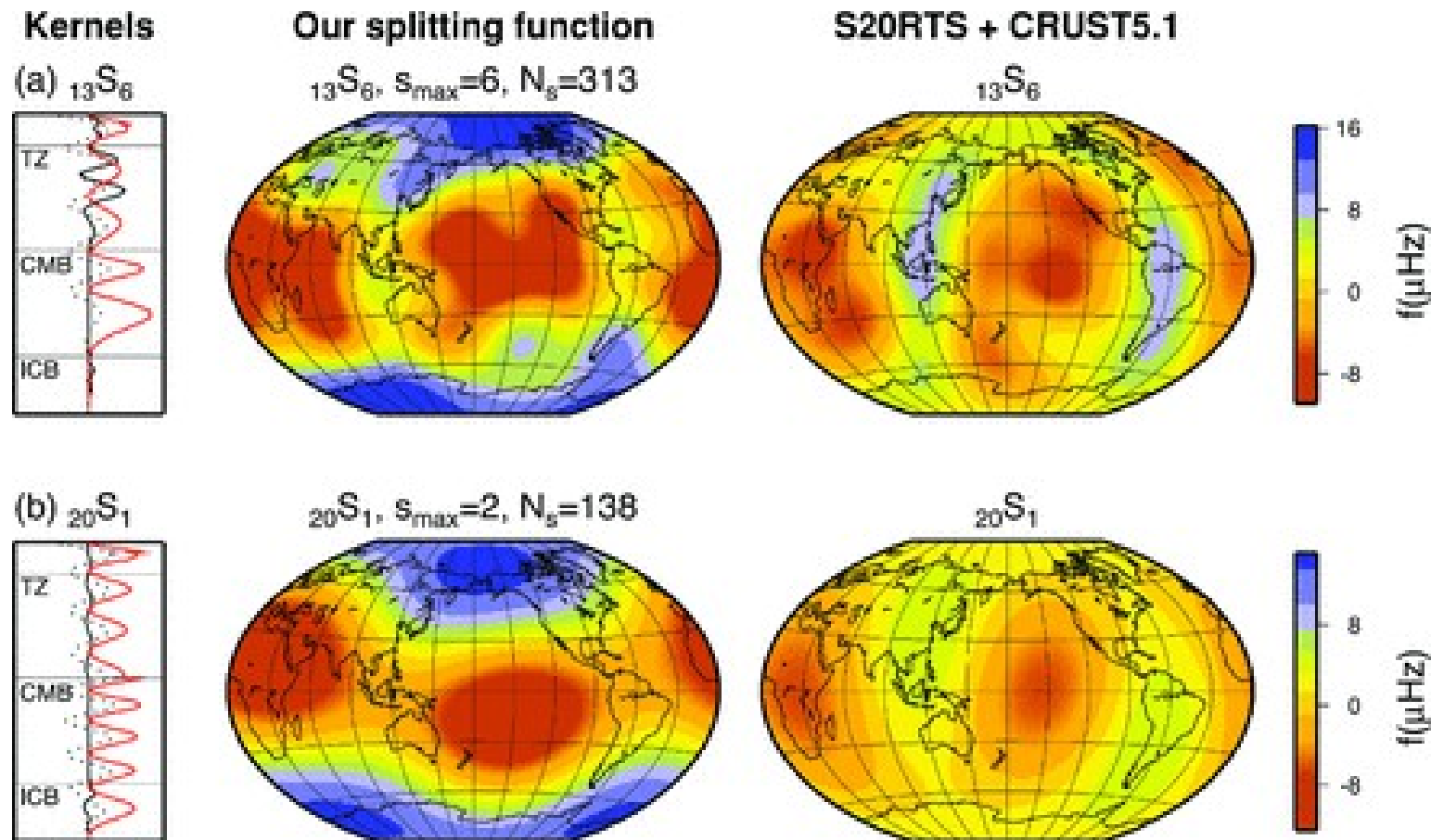


Figure 10. Our splitting function observations for two inner-core sensitive modes which have not been measured before. Also shown are the S20RTS + CRUST5.1 predictions and the sensitivity kernels, where the solid black line is  $v_s$ , the solid red line is  $v_p$  and the dotted line is  $\rho$ .

# MODE MODELS OF INNER CORE ANISOTROPY

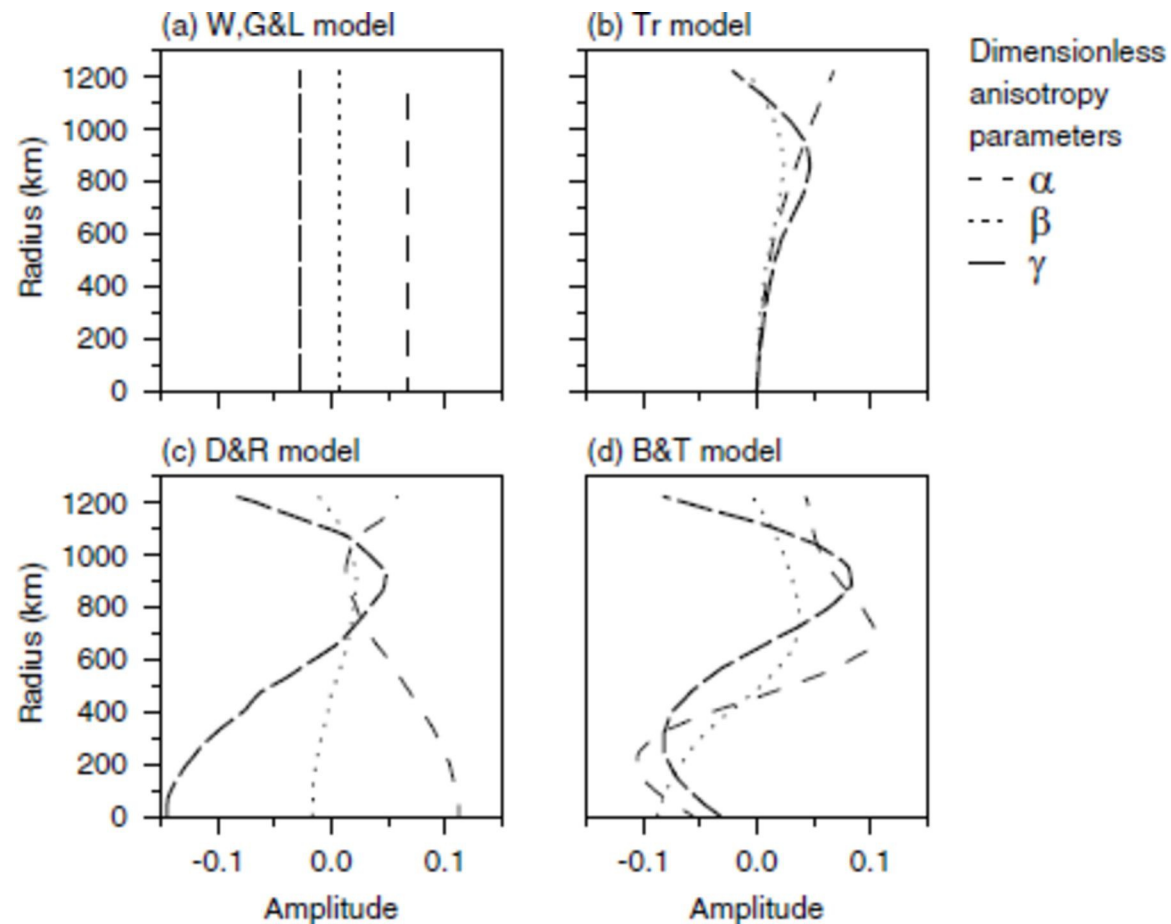
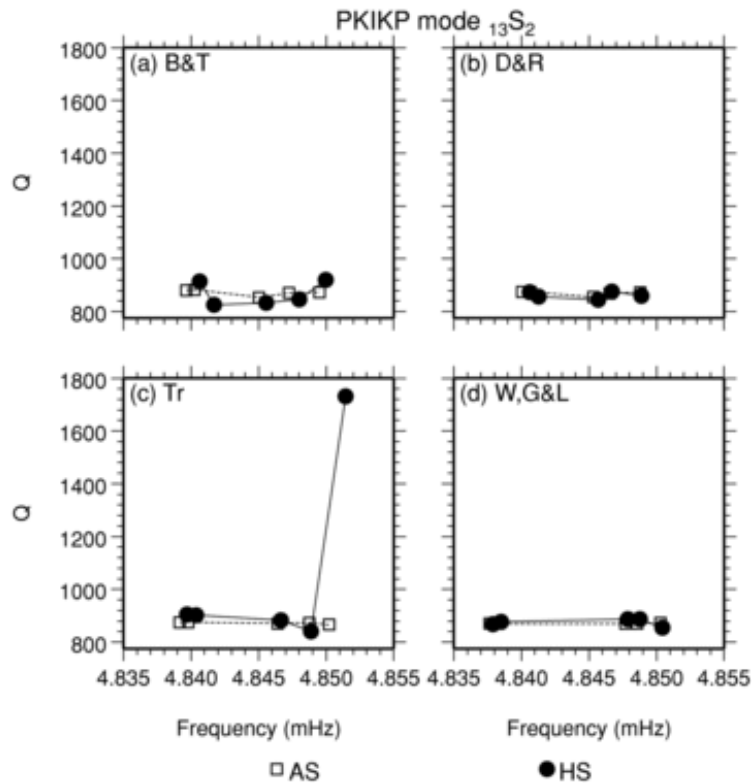
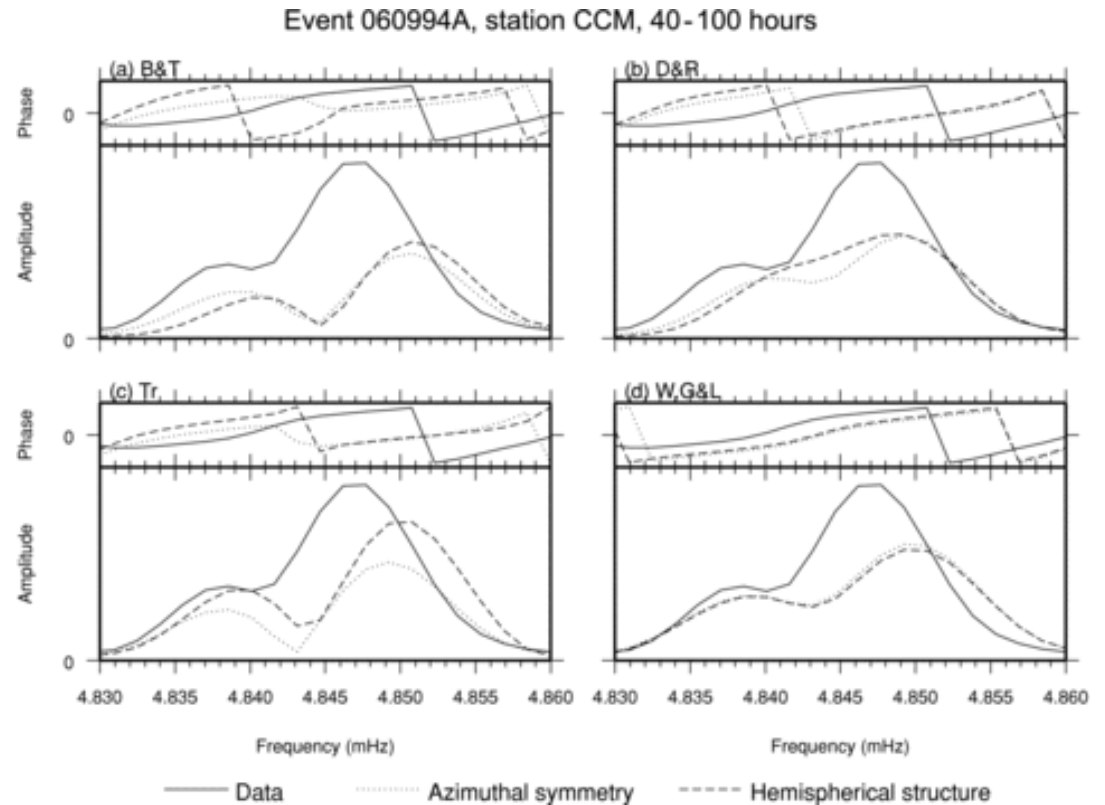


Figure 1. Comparison of different inner core anisotropy models in terms of the parameters  $\alpha$ ,  $\beta$  and  $\gamma$  (see eq. 1 for definitions) for the (a) W,G&L (Woodhouse *et al.* 1986), (b) Tr (Tromp 1993), (c) D&R (Durek & Romanowicz 1999) and (d) B&T (Beghein & Trampert 2003) models.

# MODES AND INNER CORE ANISOTROPY



**Figure 8.** Frequency and quality factor of PKIKP mode  ${}_{13}S_2$  when the inner core model is azimuthally symmetric (AS, open square) or contains hemispherical structure (HS, solid circle) for the (a) B&T model, (b) D&R model, (c) Tr model and (d) W,G&L model. Mantle heterogeneities, rotation and ellipticity and coupling with mantle sensitive modes have been included in these calculations.



**Figure 9.** Data (solid line) and synthetic seismograms for PKIKP mode  ${}_{13}S_2$  when the inner core is azimuthally symmetric (AS, dotted line) or contains hemispherical anisotropic structure (HS, dashed line) for event 060994A. The inner core anisotropy models used are the: (a) B&T model, (b) D&R model, (c) Tr model and (d) W,G&L model.

# MODES AND THE INNER CORE AND ...

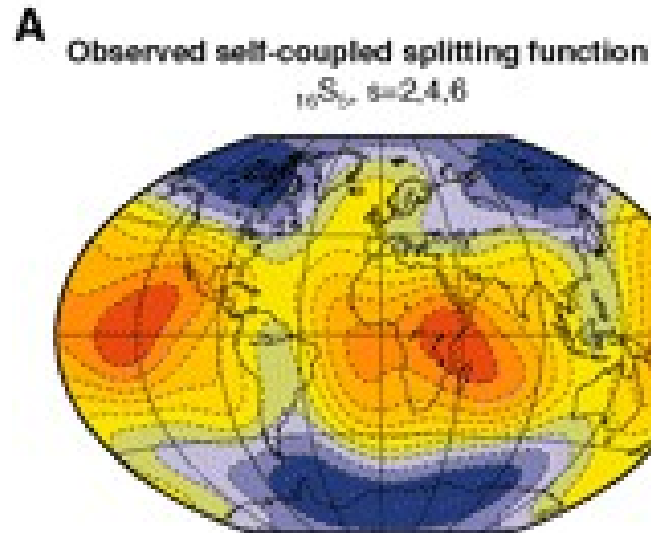
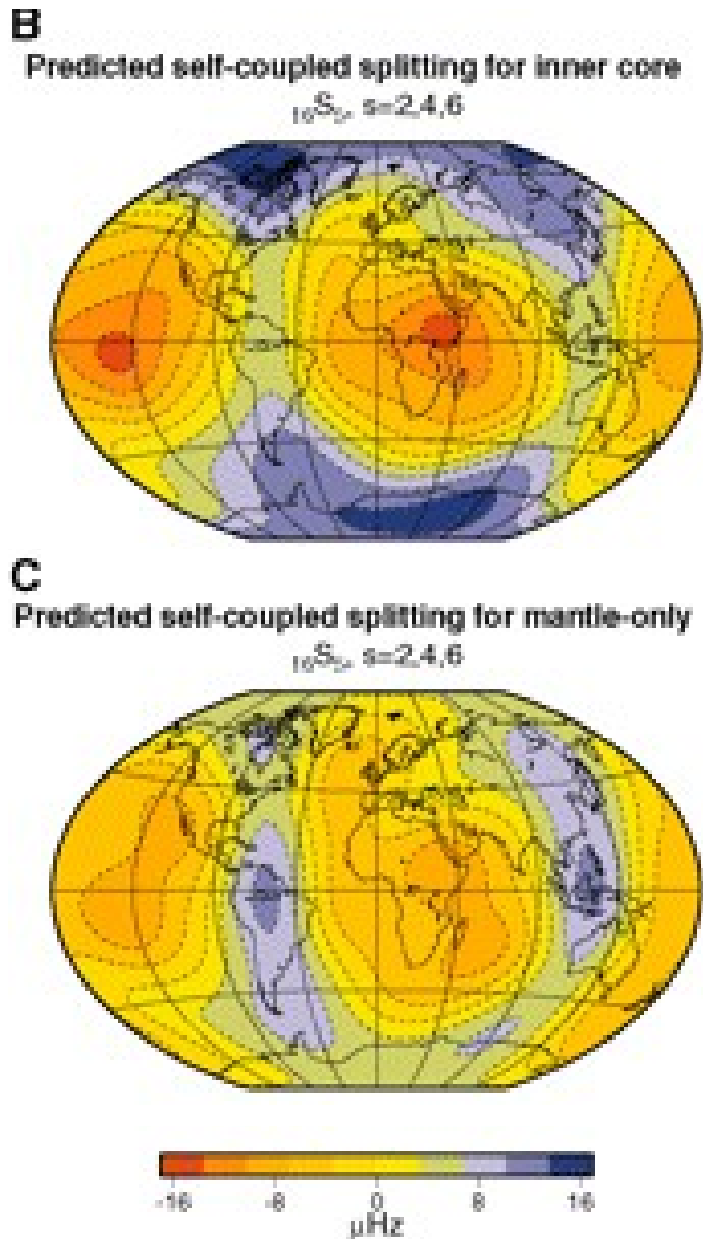
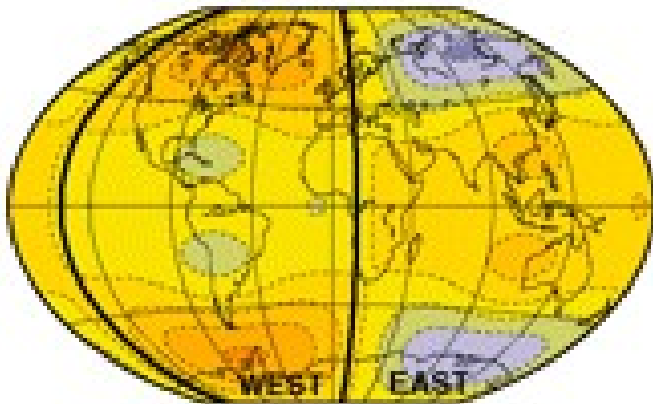


Fig. 1: Observed and predicted splitting functions for the mode pair  ${}_{16}S_5$  and . (A) Observed splitting function using self-coupling only for  ${}_{16}S_5$  showing typical zonal splitting. (B) Predicted self-coupled splitting function for a mantle model and a cylindrically anisotropic inner core model (12). (C) Predicted self-coupled splitting function for mantle-only model S20RTS (31). (D) Observed cross-coupled splitting function showing antisymmetric splitting, which changes sign across Africa. (E) Predicted cross-coupled splitting function for anisotropy only between hemisphere boundaries at  $151^\circ\text{W}$  and  $14^\circ\text{E}$ . (F) Predicted cross-coupled splitting function for mantle-only structure. Thick lines denote the hemisphere boundaries found from body wave observations (Fig. 3).  $s$  is the angular order of the observed structure.

# MODES AND THE INNER CORE AND HEMISPHERES!

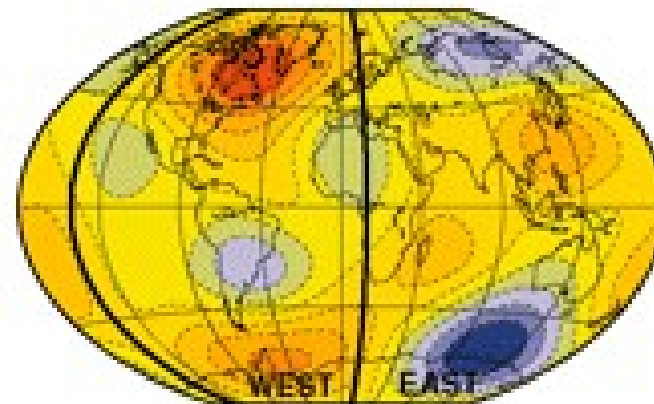
**E**  
Predicted cross-coupled splitting for inner core

$${}_{16}S_5 \sim {}_{17}S_4^j, s=1,3,5$$



**D**  
Observed cross-coupled splitting function

$${}_{16}S_5 \sim {}_{17}S_4^j, s=1,3,5$$



**F**  
Predicted cross-coupled splitting for mantle-only

$${}_{16}S_5 \sim {}_{17}S_4^j, s=1,3,5$$

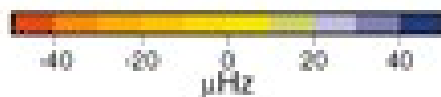
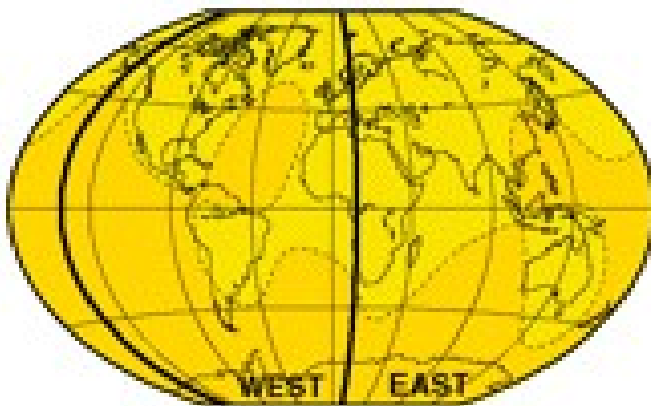
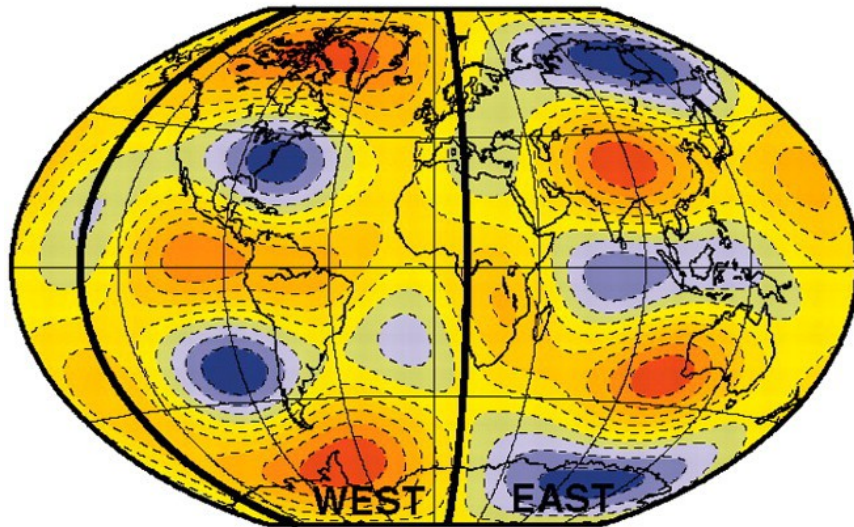


Fig. 1: Observed and predicted splitting functions for the mode pair  ${}_{16}S_5$  and  ${}_{17}S_4^j$ . (A) Observed splitting function using self-coupling only for  ${}_{16}S_5$  showing typical zonal splitting. (B) Predicted self-coupled splitting function for a mantle model and a cylindrically anisotropic inner core model (12). (C) Predicted self-coupled splitting function for mantle-only model S20RTS (31). (D) Observed cross-coupled splitting function showing antisymmetric splitting, which changes sign across Africa. (E) Predicted cross-coupled splitting function for anisotropy only between hemisphere boundaries at  $151^\circ\text{W}$  and  $14^\circ\text{E}$ . (F) Predicted cross-coupled splitting function for mantle-only structure. Thick lines denote the hemisphere boundaries found from body wave observations (Fig. 3).  $s$  is the angular order of the observed structure.

# MODES AND THE INNER CORE

**A** Observed cross-coupled splitting function

$${}_8S_{5-5}S_{10}^J, s=5$$



**B** Observed cross-coupled splitting function

$${}_{14}S_{4-11}S_7, s=3,5$$

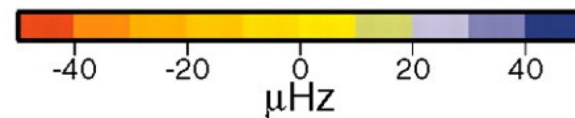
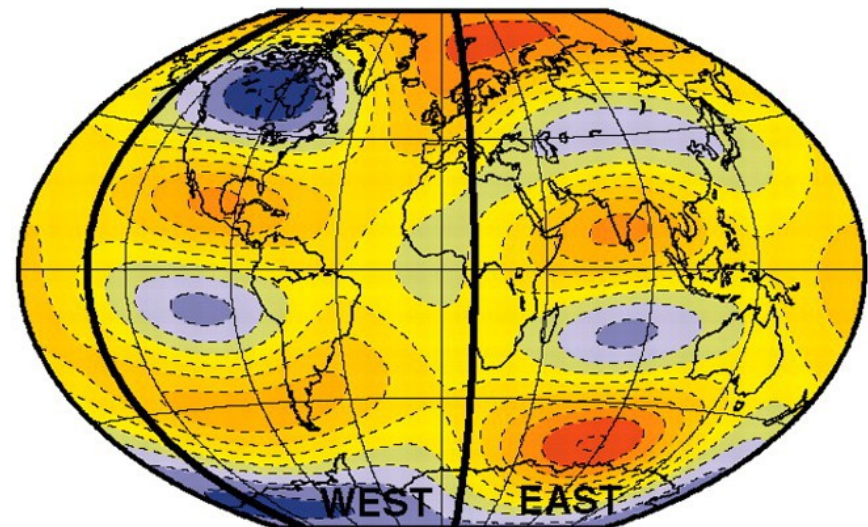


Fig. 2: Observed cross-coupled splitting functions for mode pairs (A)  ${}_8S_{5-5}S_{10}^J$  and (B)  ${}_{14}S_{4-11}S_7$

From Deuss et al, *Science.*, 2010

# MODES AND THE INNER CORE

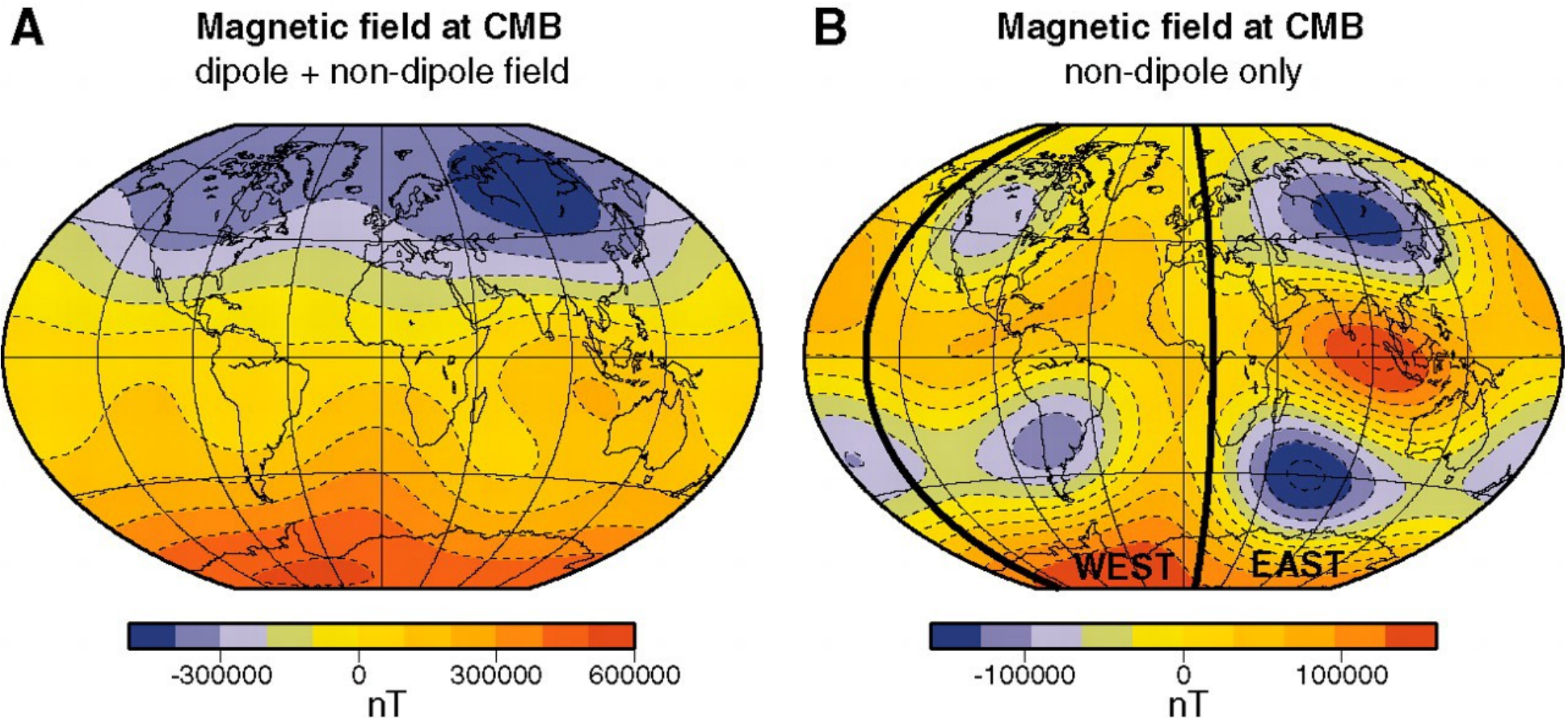
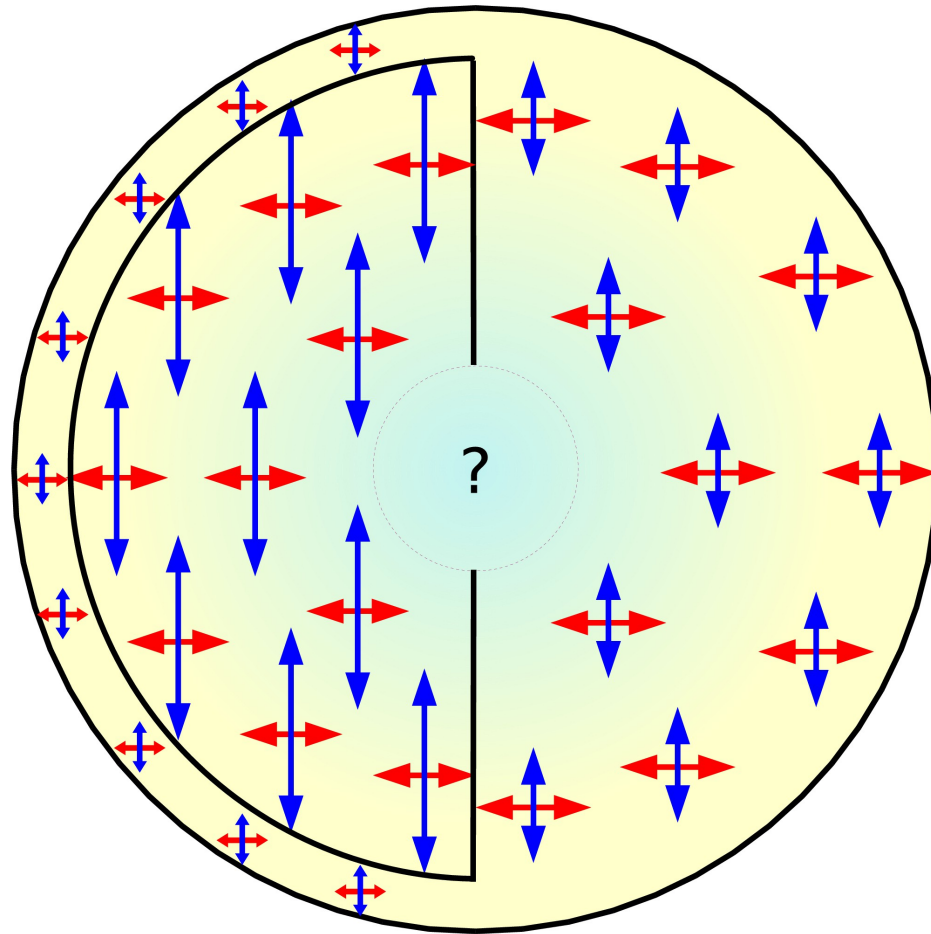


Fig. 4: Observed radial component of the Earth's magnetic field at the CMB, averaged over the last 5 million years (27). (A) The total magnetic field is dominated by the dipole component; the non-dipole field is also included. (B) The non-dipole component of the field shows four increased negative flux patches. These flux patches are also seen in the current-day magnetic field (fig. S7) and correspond to the locations of maximum hemispherical variations in seismic anisotropy (Figs. 1D and 2, A and B).

# INNER CORE ANISOTropy

- Anisotropy may be due to crystalline alignment, produced by magnetic or thermal gradients.
- Structure may develop during or after crystallization
- There may be larger scale structures preferentially aligned in one direction.



More  
anisotropic  
western  
hemisphere

Less  
anisotropic  
eastern  
hemisphere

# INNER CORE ANISOTROPY

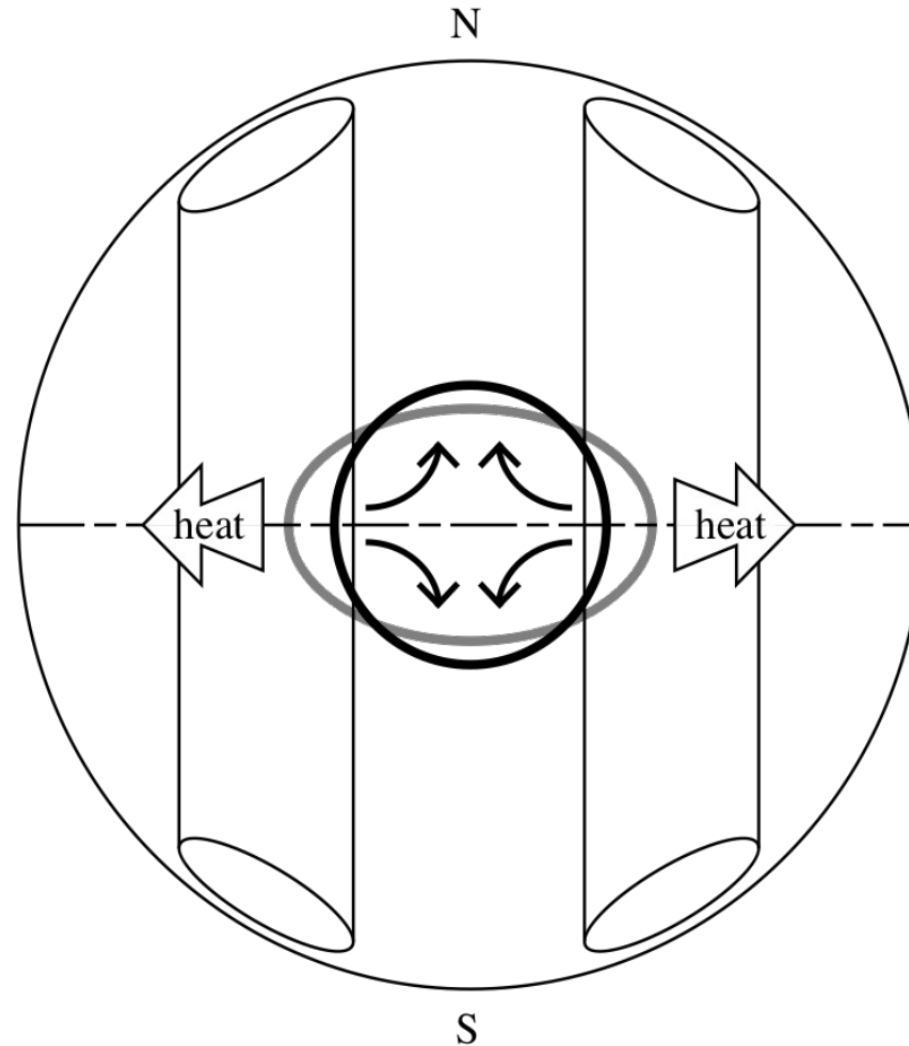
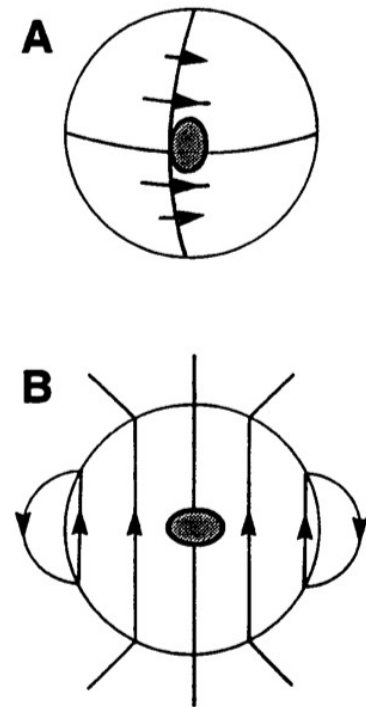


**Figure 3.** A conceptual picture of the Yoshida *et al* model [25]. Columnar convection formed under the strong influence of the Coriolis force transports heat more in the equatorial region than in the polar regions. The anisotropic heat transfer gives rise to anisotropic growth of the inner core, which, in turn, produces flow in the inner core to keep the state of isostatic equilibrium.

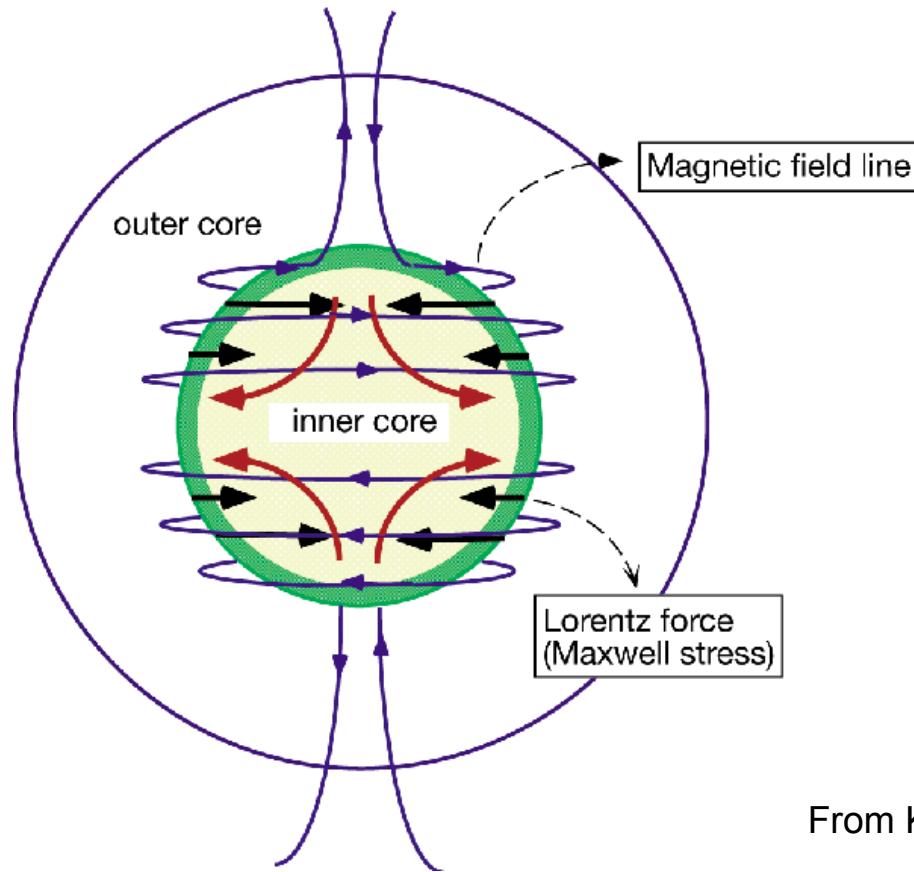
# INNER CORE ANISOTROPY

“Anisotropy of the inner core of the Earth is proposed to result from the lattice preferred orientation of anisotropic iron crystals during their solidification in the presence of a magnetic field. The resultant seismic anisotropy is related to the geometry of the magnetic field in the core.”

**Fig. 3.** Schematic diagrams showing the geometry of the magnetic field and the predicted anisotropy of compressional wave velocities in the inner core (magnetic field lines are indicated by the thin lines with arrows, and the anisotropic compressional wave velocities are shown by the ellipsoids). The anisotropic magnetic susceptibility and elasticity relevant to  $\epsilon$ -Fe are assumed. The rotation axis is north-south. **(A)** Toroidal field. **(B)** Poloidal field. The seismological observations (the fast direction parallel to the rotation axis) are consistent with the dominance of the toroidal field in the core, which supports a strong field model of the geodynamo.



# INNER CORE ANISOTROPY



From Karato, *Nature*, 1999

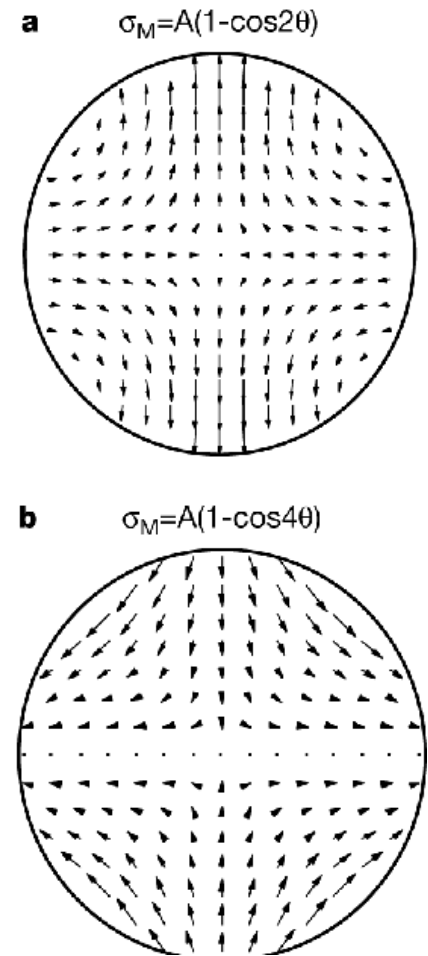
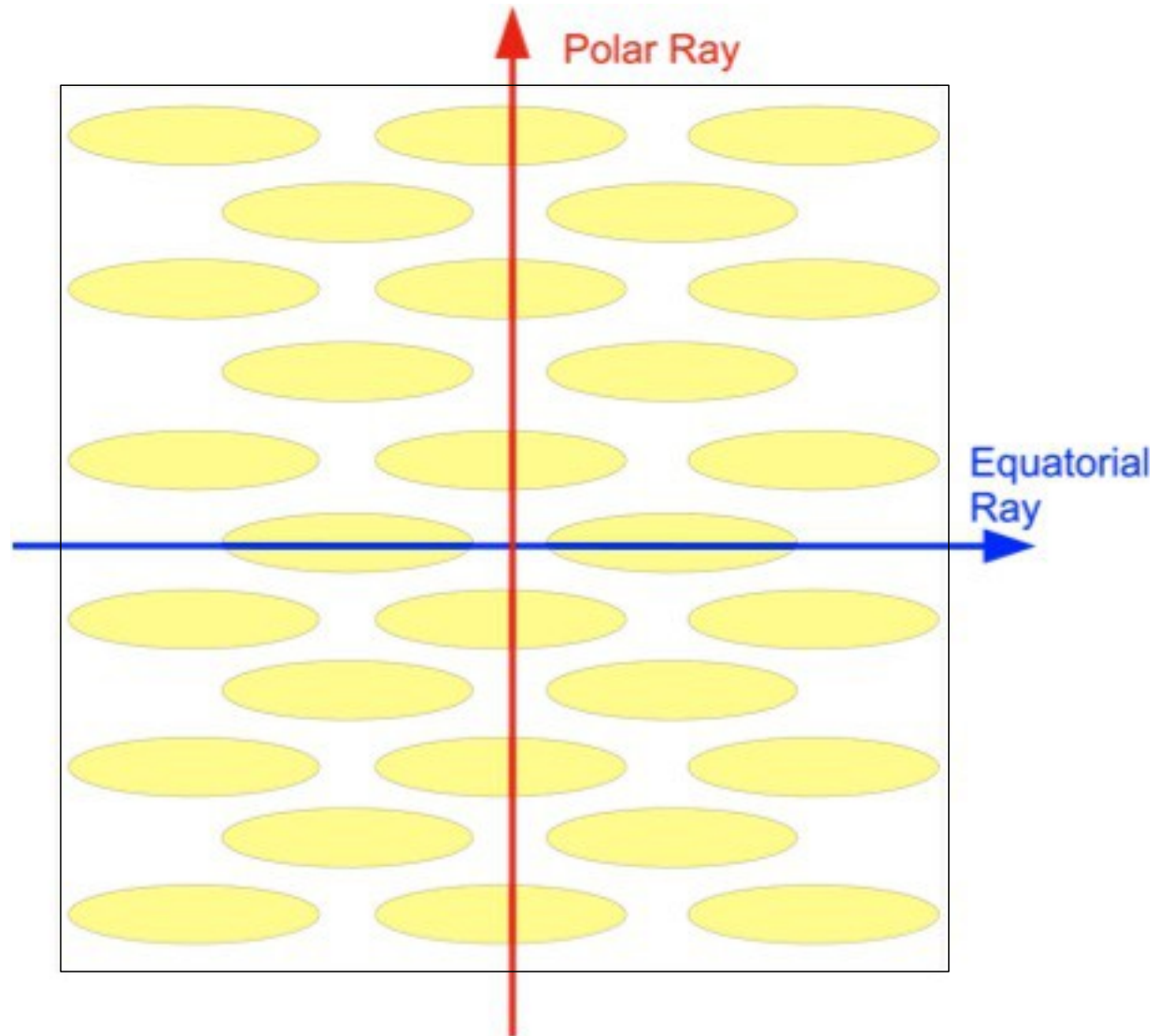


Figure 2. Flow velocity vectors in a meridional plane are shown. The geometry of the flow field is determined by the geometry of the magnetic field at the inner–outer core boundary. The flow field corresponding to the Maxwell stress of (panel a)  $\sigma_M(\theta) = A(1 - \cos 2\theta)$  (corresponding to the symmetric toroidal field) and (panel b)  $\sigma_M(\theta) = A(1 - \cos 4\theta)$  (corresponding to the antisymmetric toroidal field) are shown.

Figure 1. The dynamics of the outer portion of the inner core (dark-green, thin layer) is dominated by the direct effects of the Lorentz force (the Maxwell stress). The dynamics in the deep portions are controlled by the force balance between the pressure gradient and the viscous force, with a constraint imposed by the boundary conditions near the surface of the inner core which are dominated by the Maxwell stress. The Lorentz force (the Maxwell stress) caused by the toroidal magnetic field squeezes inner-core materials towards the rotation axis, and causes a flow from strong-field regions to weak-field regions. The flow pattern is sensitive to the geometry of the magnetic field (see Fig. 2). Black arrows, Lorentz force; red arrows, flow directions; blue lines with arrows, magnetic field lines.

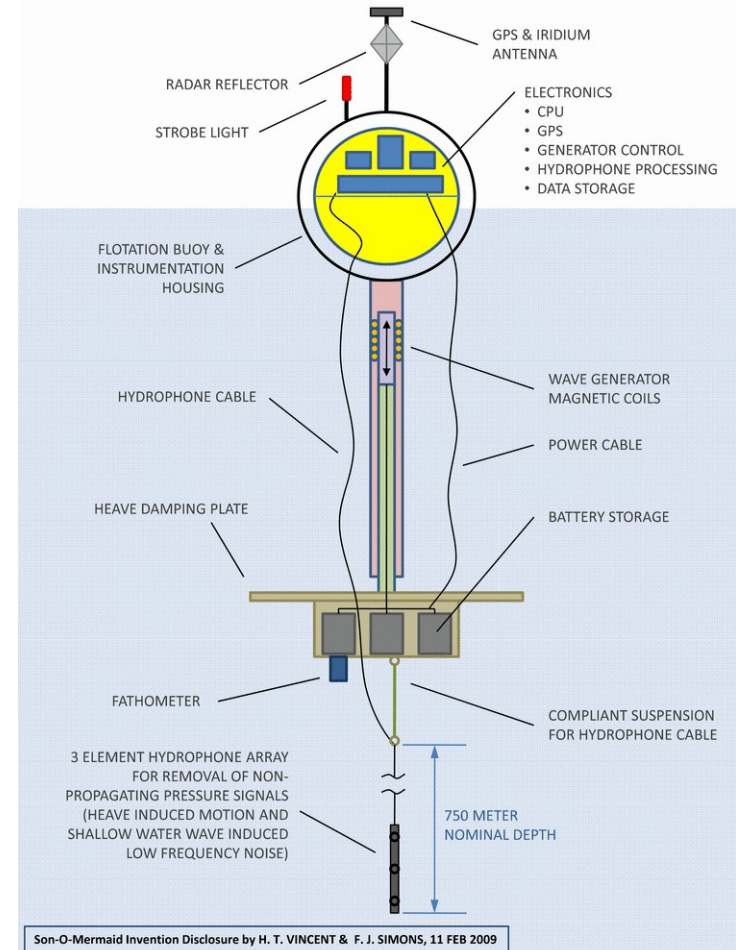
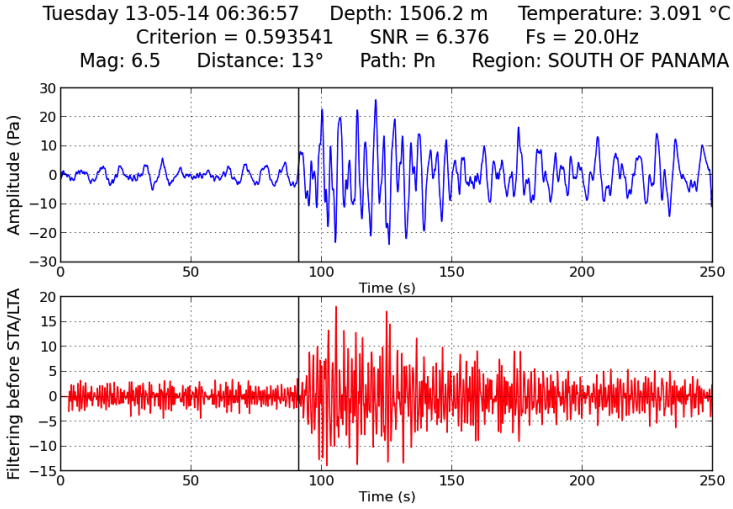
# INNER CORE ANISOTROPY



after Cormier and Li, 2002

# BRIEF DETOUR TO THE OCEANS

Mermaid project:  
<https://www.geoazur.fr/GLOBALSEIS/LatestNews/index.html>



Son-of-mermaid project:  
<http://geoweb.princeton.edu/people/simons/MERMAID.html>

# INNER CORE ROTATION?



From Glatzmaier &  
Roberts, *Nature*, 1995

“This model rate, about  $5^\circ \text{ yr}^{-1}$ , seemed fast enough to Xiaodong Song and me (both of us seismologists), to warrant a search for seismological indications.”

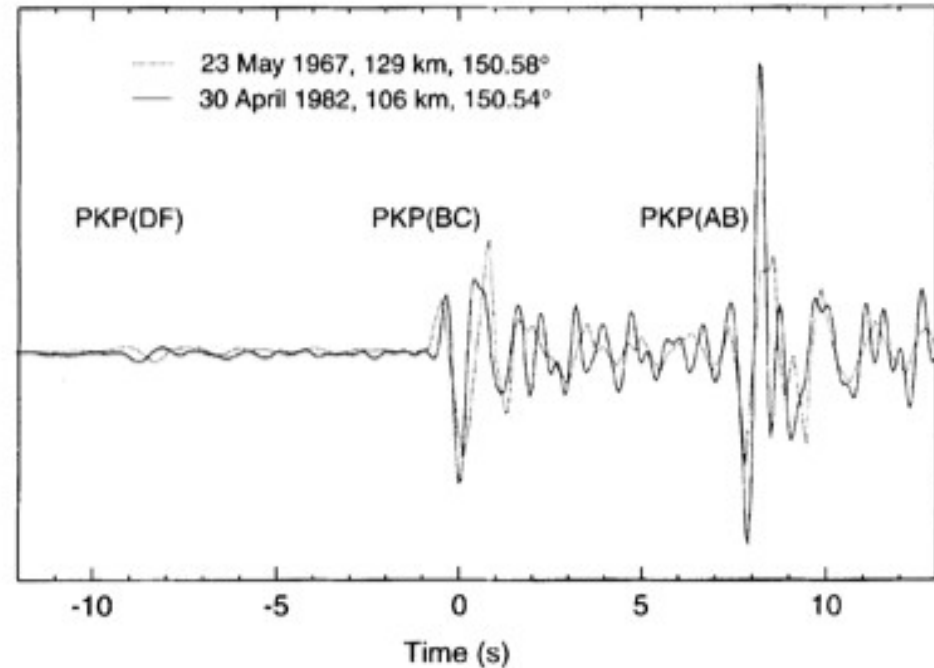


FIG. 2 An overlay of two short-period PKP seismograms from earthquakes that occurred 15 years apart at almost the same location in South Sandwich Islands, as recorded at College, Alaska (COL). Event locations in this study are taken from the Earthquake Data Reports of the US Geological Survey.

Quote from Richards,  
*Astronomy & Geophysics*, 2000;  
Seismograms from  
Song & Richards, *Nature*, 1996

# INNER CORE ROTATION?

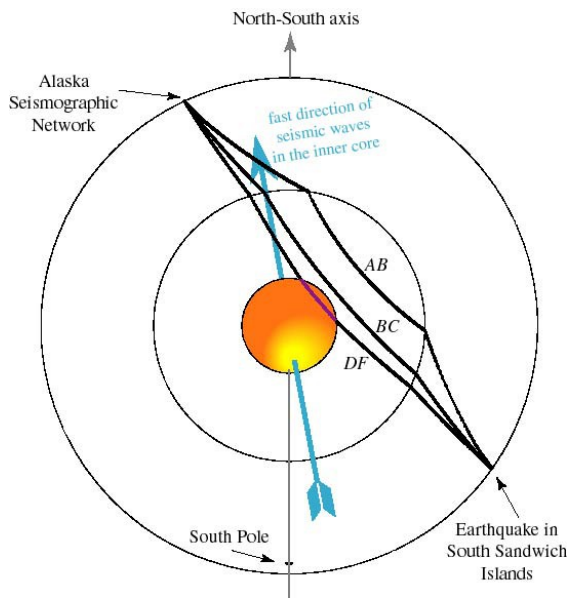


Figure from  
<https://www.ideo.columbia.edu/~richards/Jefflec.html>

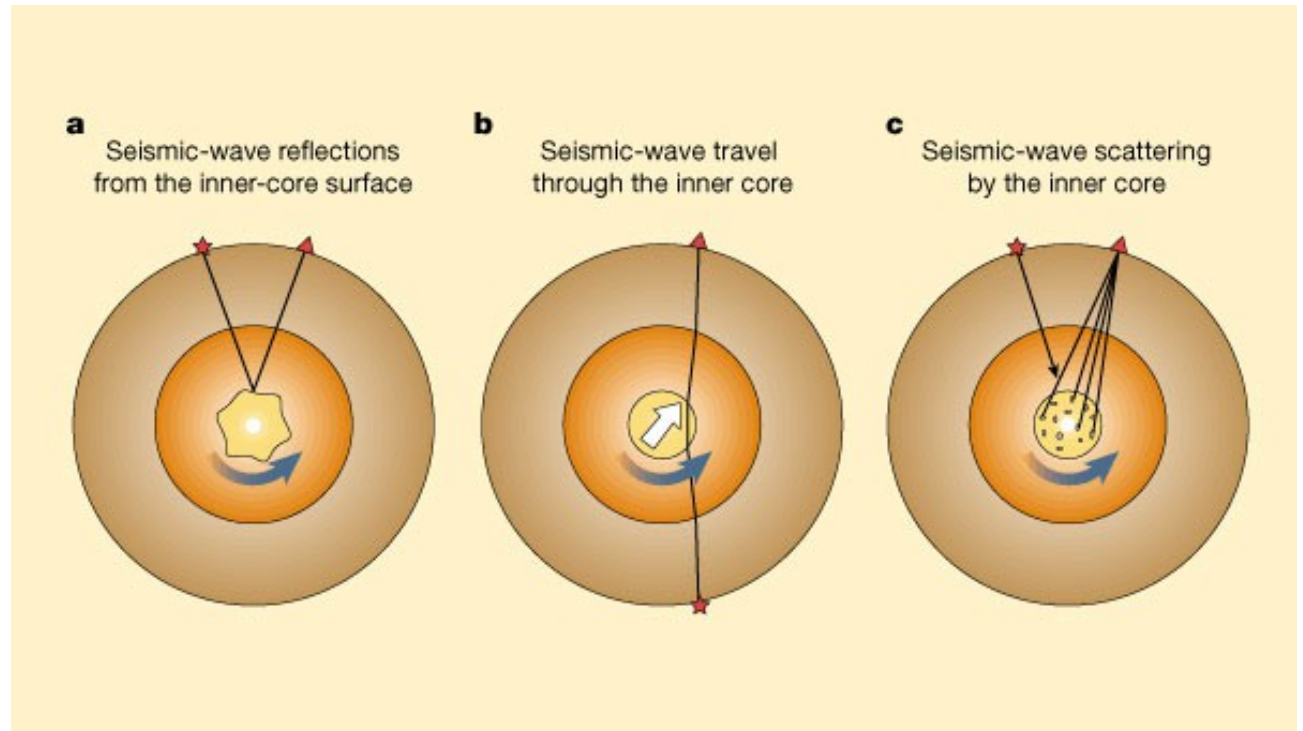
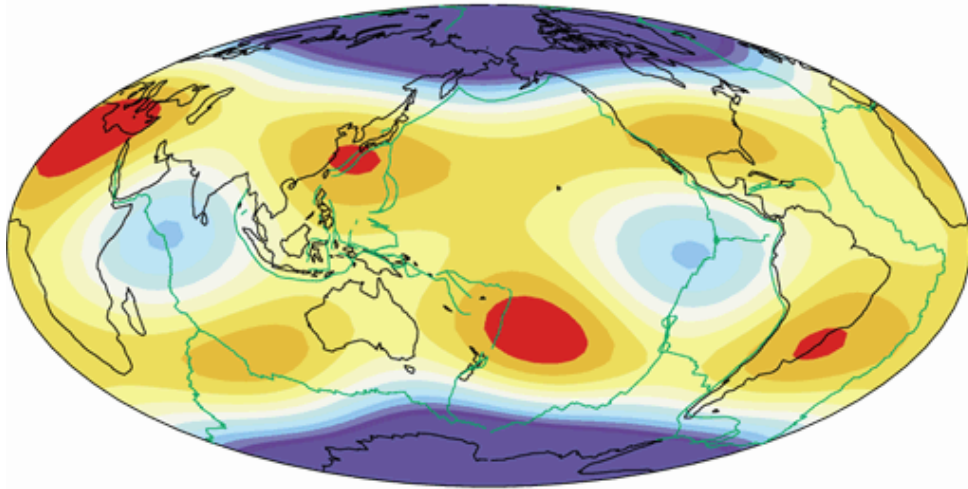


Figure from Nataf, *Nature* 2000

# INNER CORE ROTATION?

$^{13}\text{S}_2$  recent (1996 $\pm$ 2)



$^{13}\text{S}_2$  old (1981 $\pm$ 4)

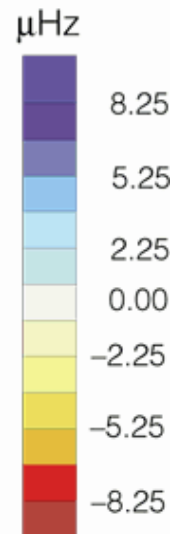
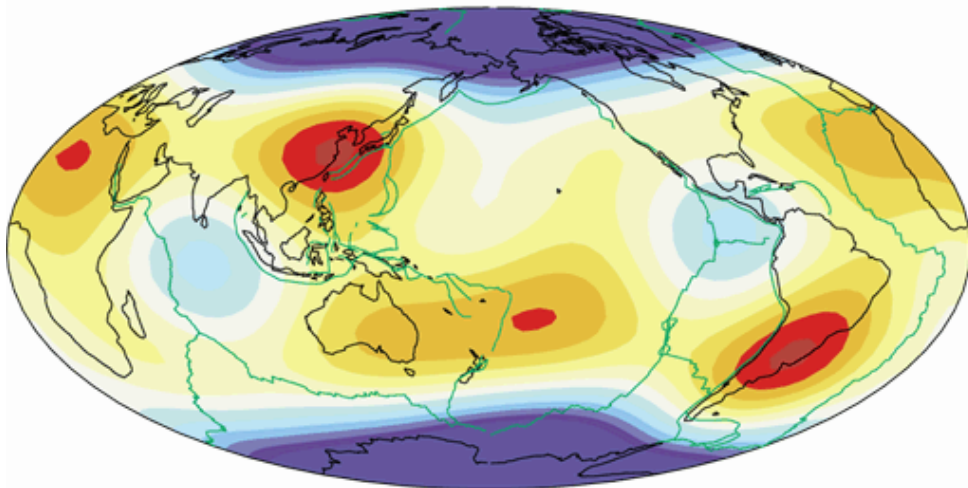


Figure 2. Panel **a** uses recent events from the years 1996  $\pm$  2, and panel **b** uses earlier events from the years 1981  $\pm$  4. The effects of rotation and ellipticity have been removed before the inversion for structure coefficients, and the contribution of the mantle<sup>31</sup> has been removed. The anomalies shown are due to structure in the inner core. A westward rotation of the lower map about the vertical axis of  $4.5^\circ$  optimally aligns it with the upper map. Provided that our mantle correction is accurate, this comparison implies a westward inner-core rotation of  $0.3^\circ$  per year.

Laske & Masters, *Nature*, 1999

# INNER CORE ROTATION?

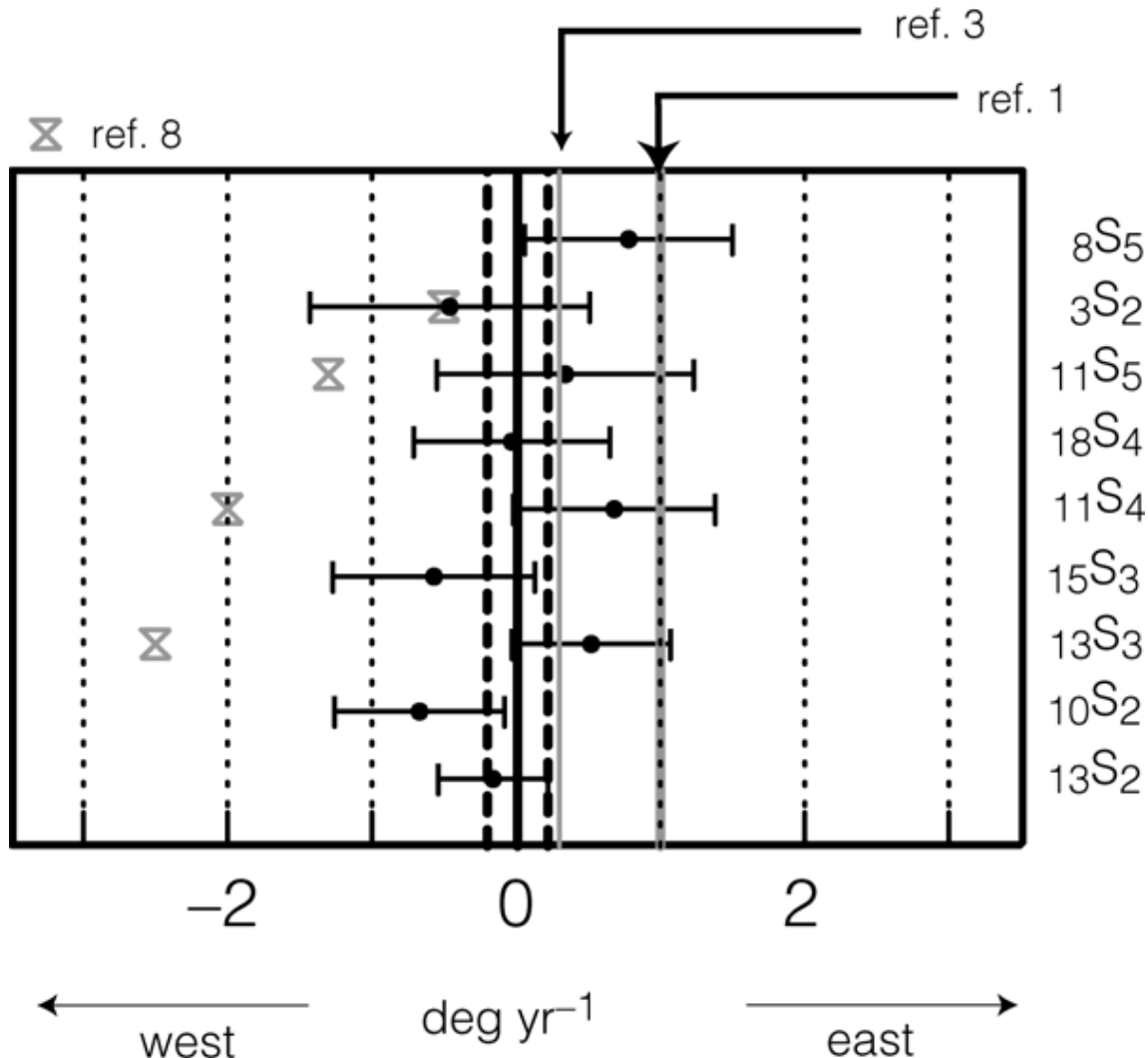
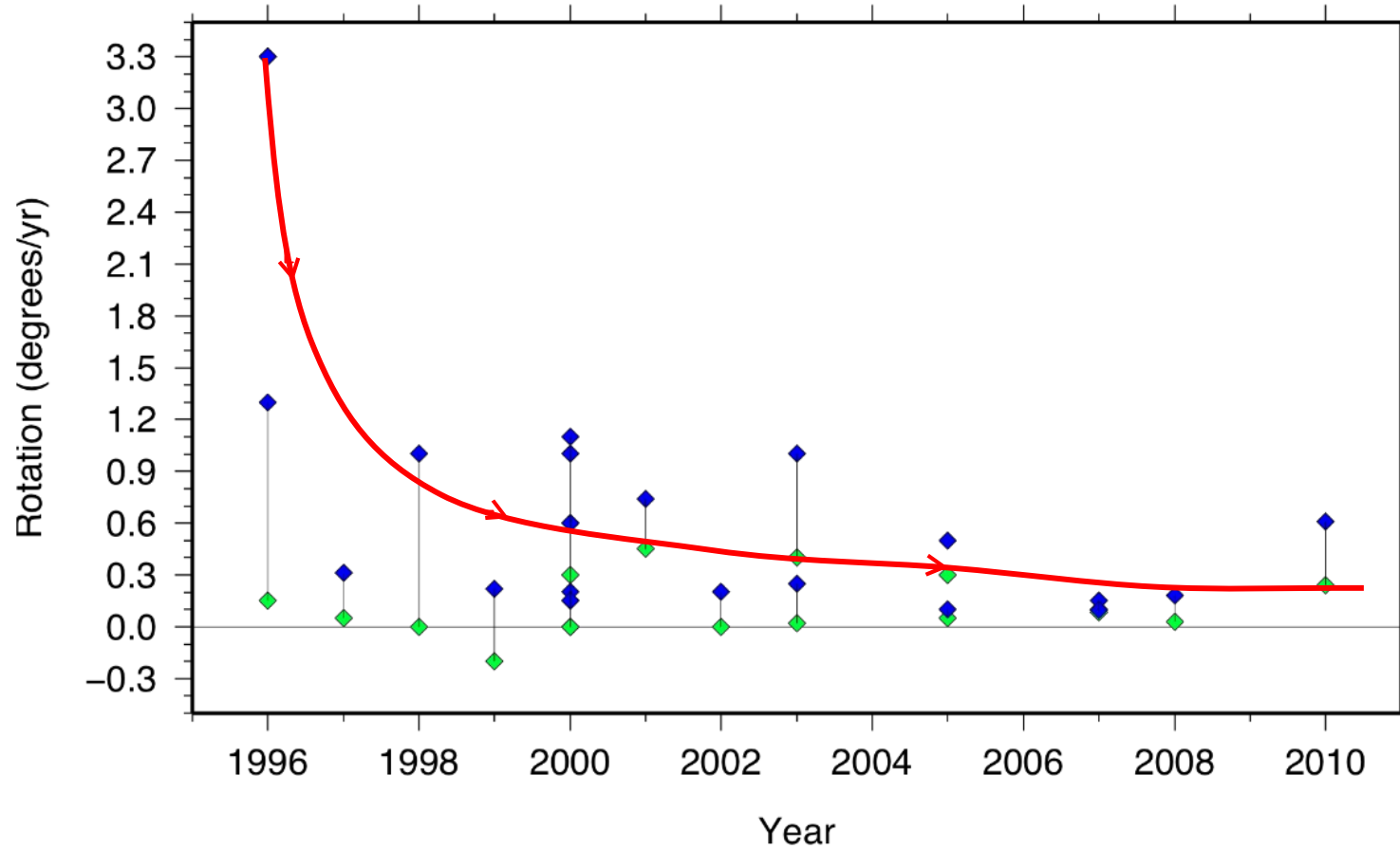
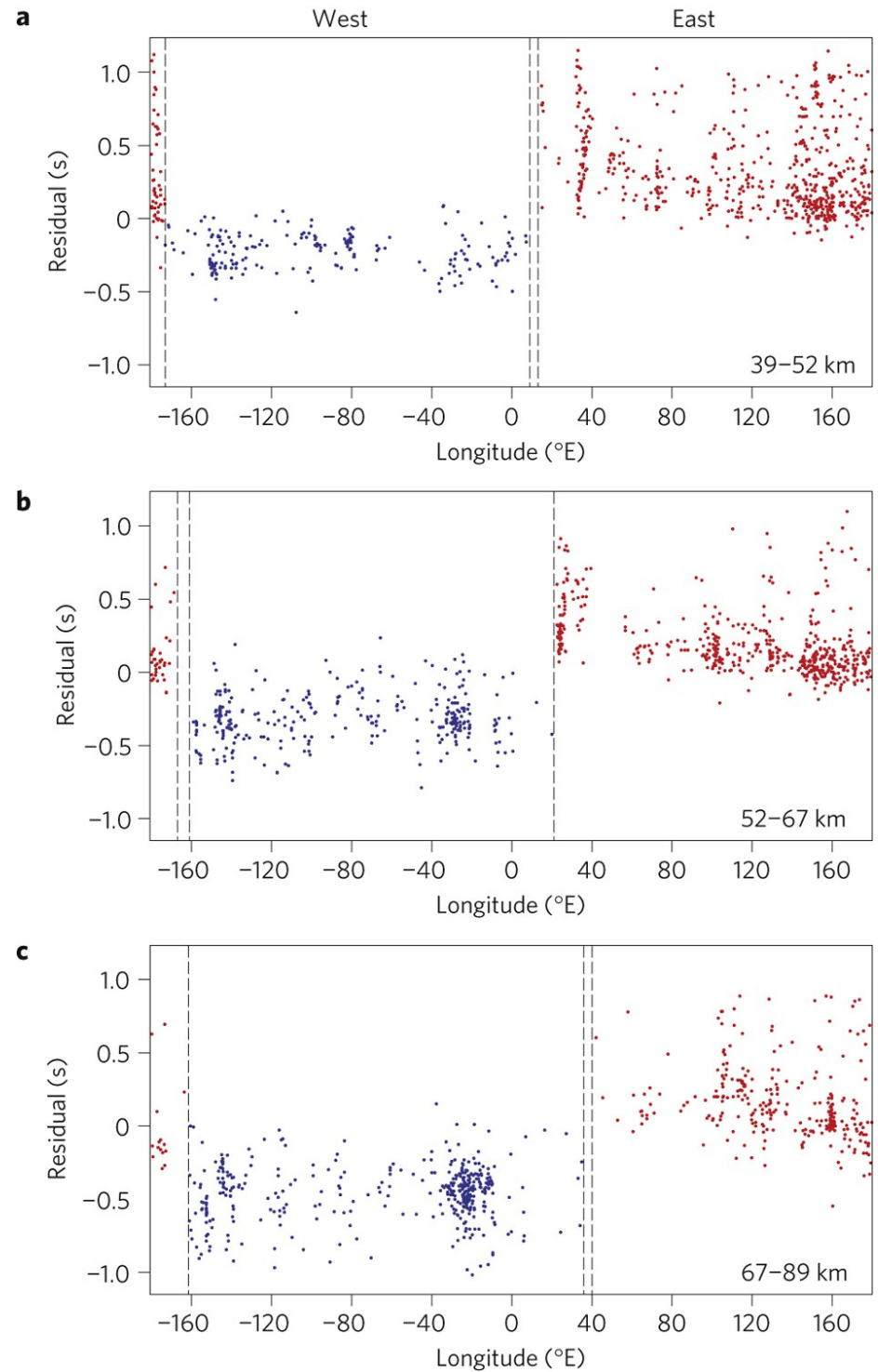
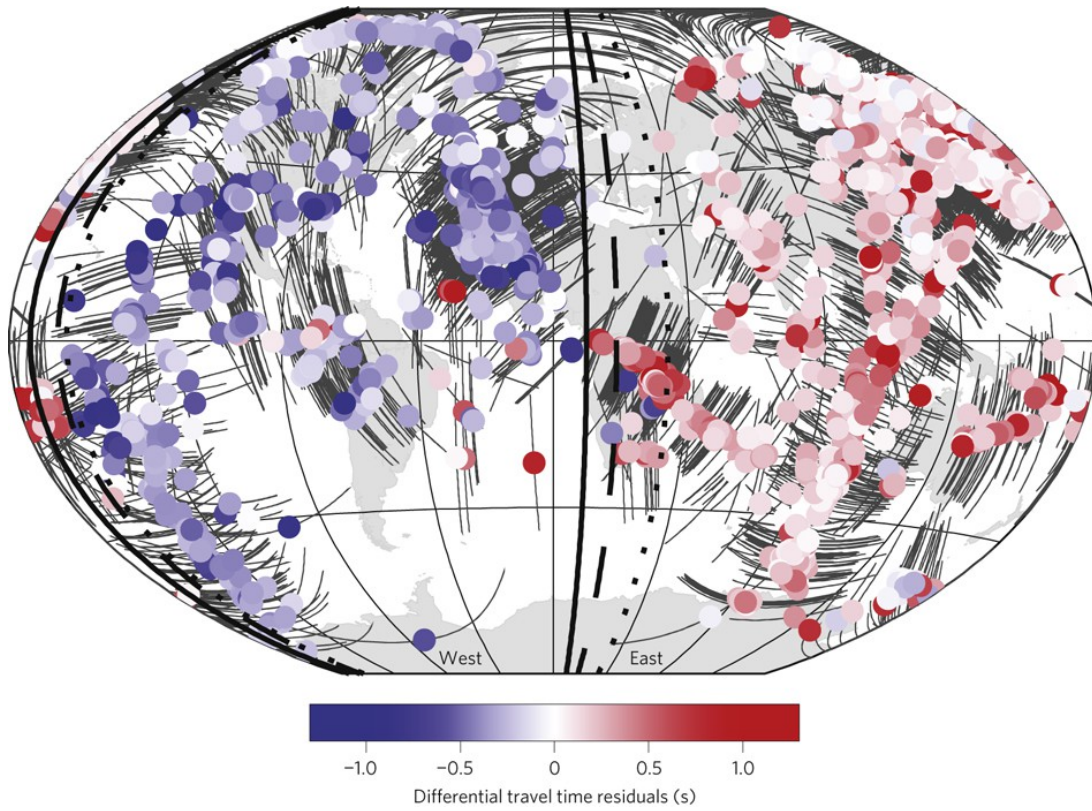


Figure 4. Also shown is the mean rotation rate,  $0.01 - 0.21 \text{ deg yr}^{-1}$ , obtained from averaging over all modes. Dashed lines mark the error bars of the average. The hour-glass symbols mark the results of a recent mode study<sup>8</sup>, and two grey vertical lines stand for the superrotations found in recent body-wave studies<sup>1, 3</sup>. Our data are marginally consistent with a superrotation of  $0.3^\circ$  per year, though a superrotation of  $1^\circ$  per year is clearly inconsistent for most of the modes. See Table 1 for event abbreviations.

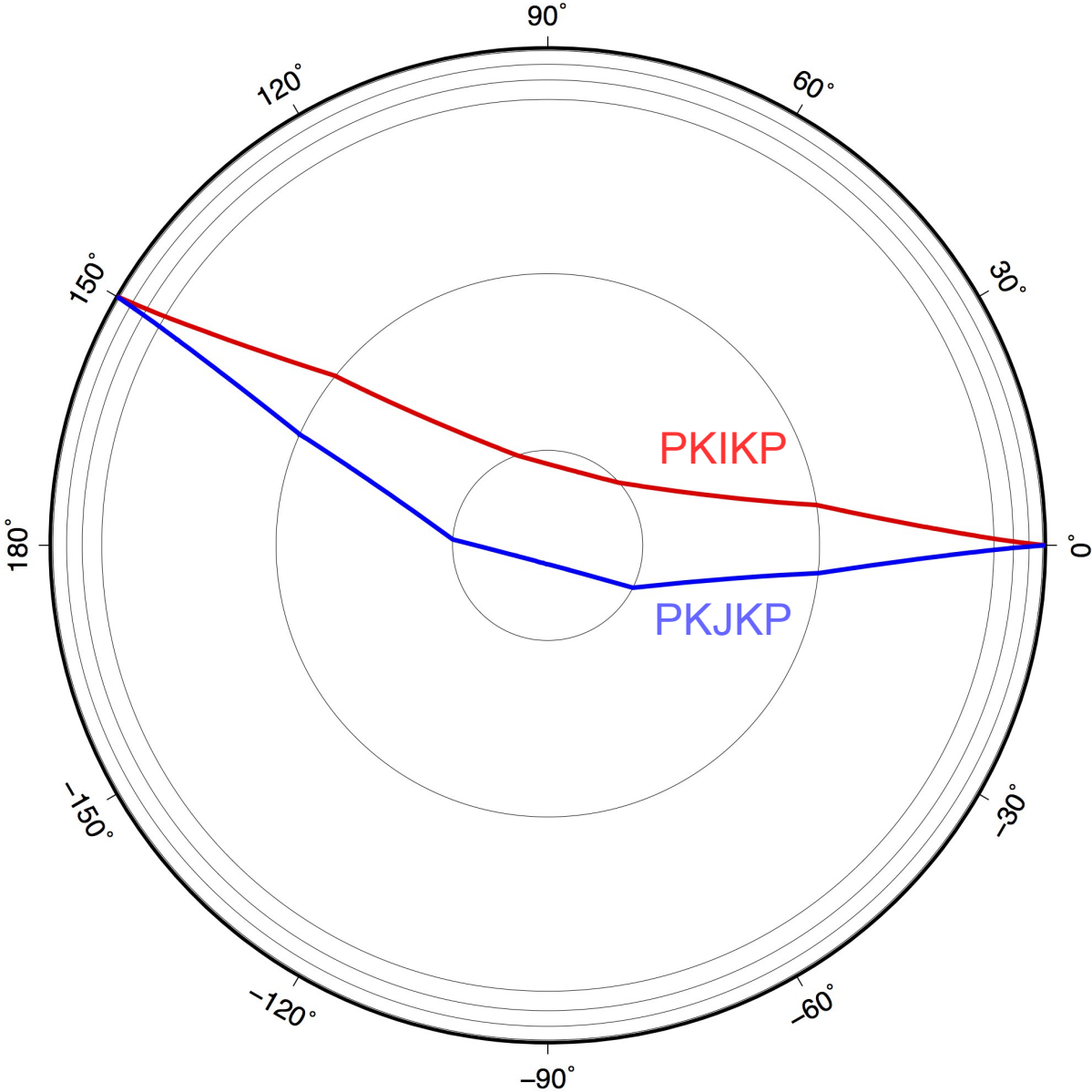
# INNER CORE ROTATION?



# INNER CORE ROTATION?

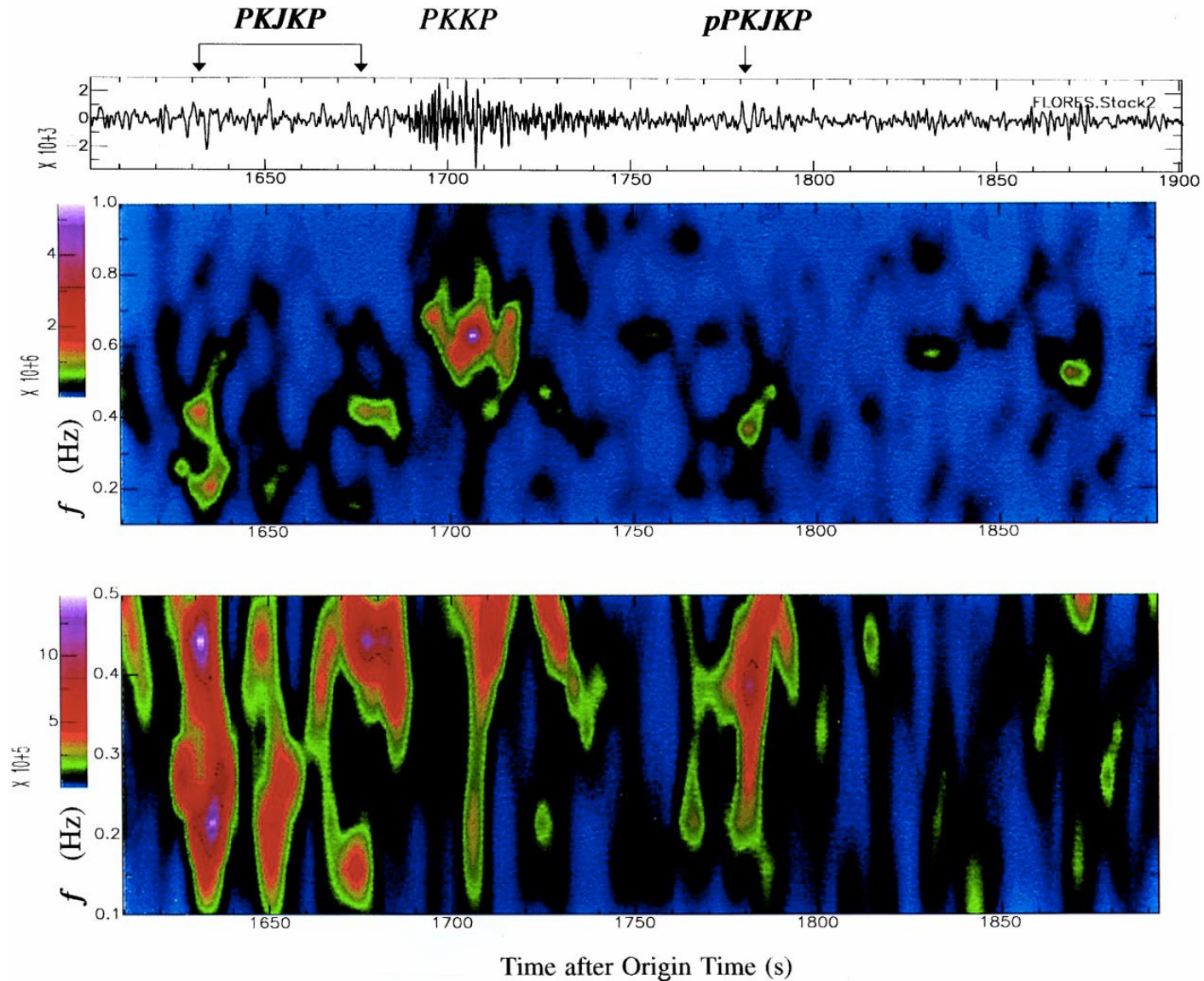


# PKJKP

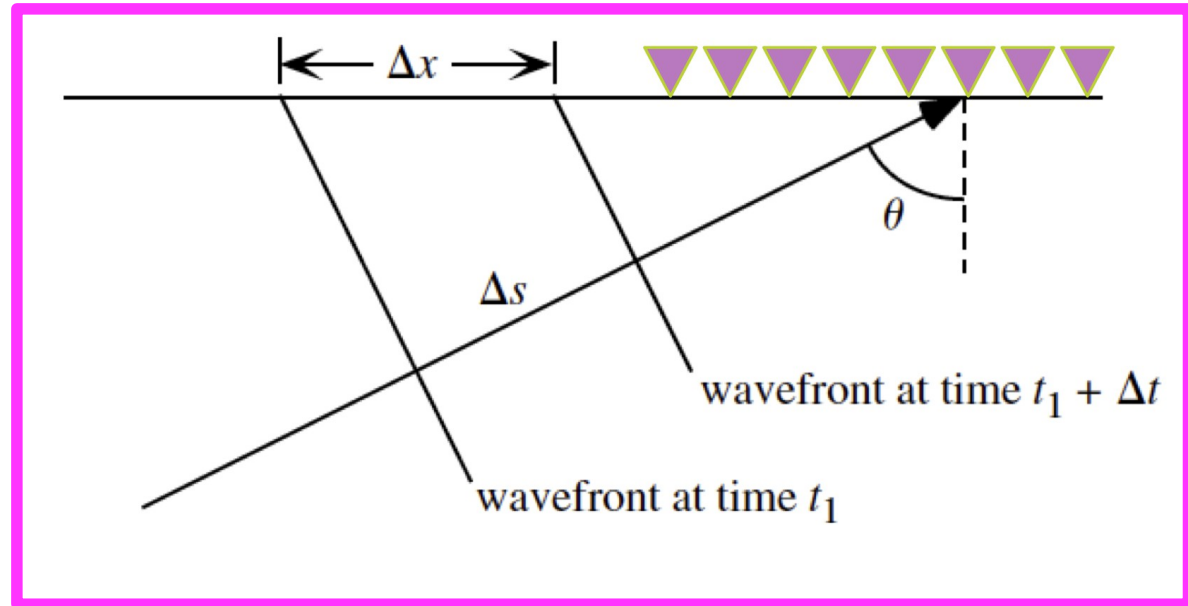
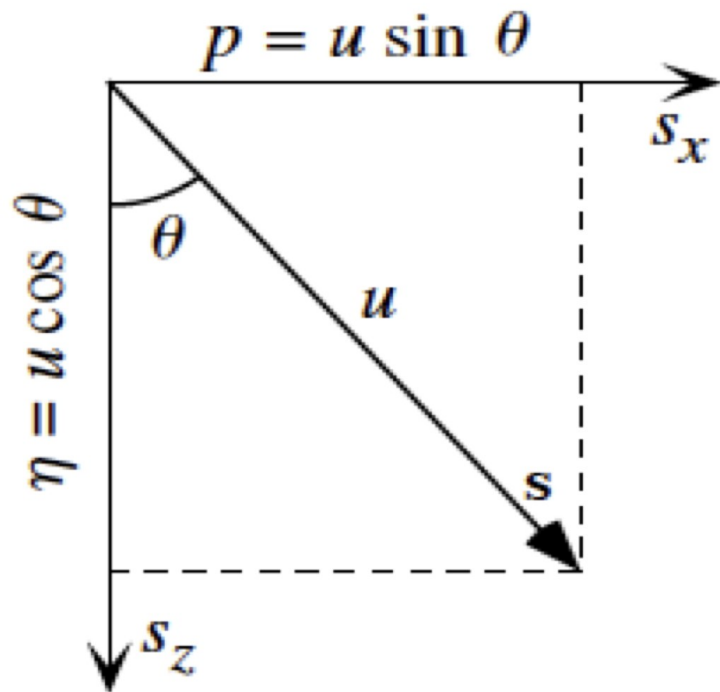


# PKJKP

“Note that the phase pPKJKP is clearly observable in the time domain.”



# Horizontal & vertical slownesses



- Slowness:  $u = 1 / c$
- Horizontal slowness:  $p = \Delta T / \Delta X$
- Vertical slowness:  $\eta = (u^2 - p^2)^{1/2}$

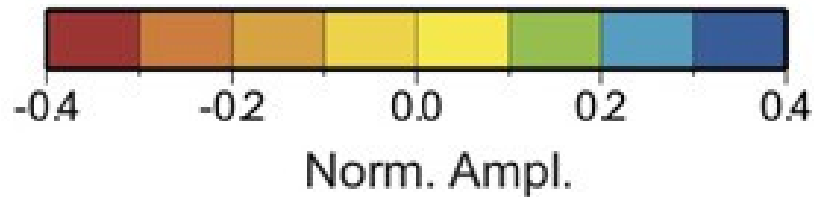
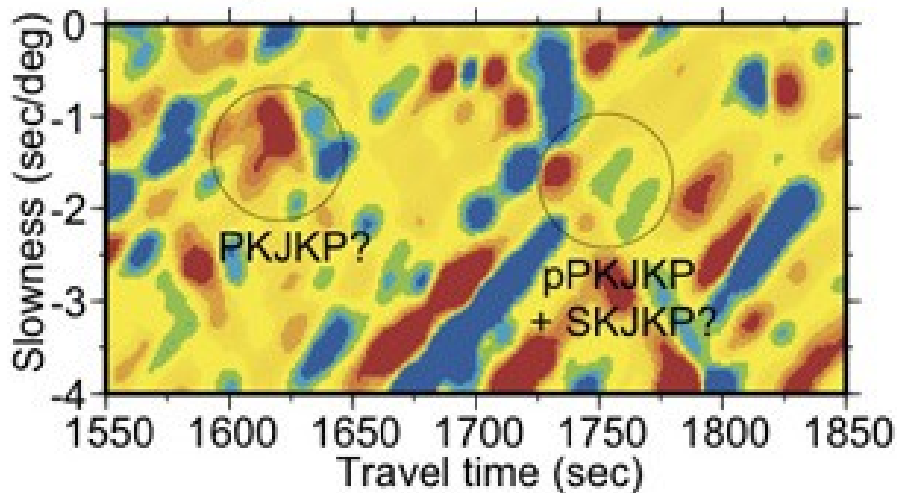
- We can measure how quickly a wave sweeps across a small, dense array of seismometers

figures from Shearer, 2009

# PKJKP

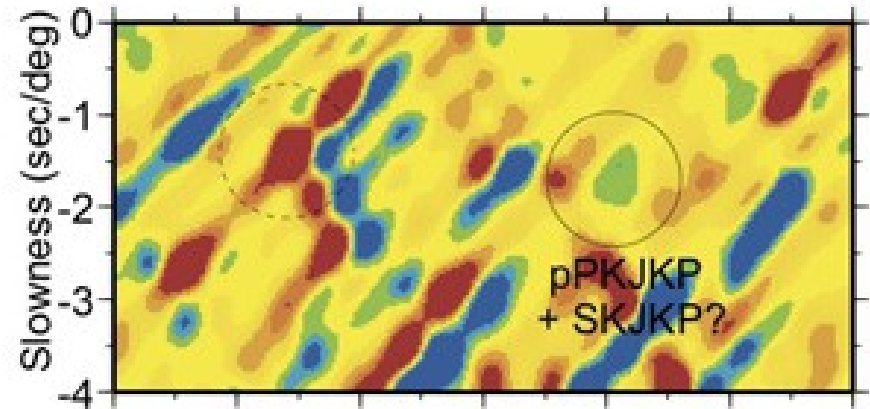
## Observation

Phase weighted stack for Flores Sea 17 June 1996

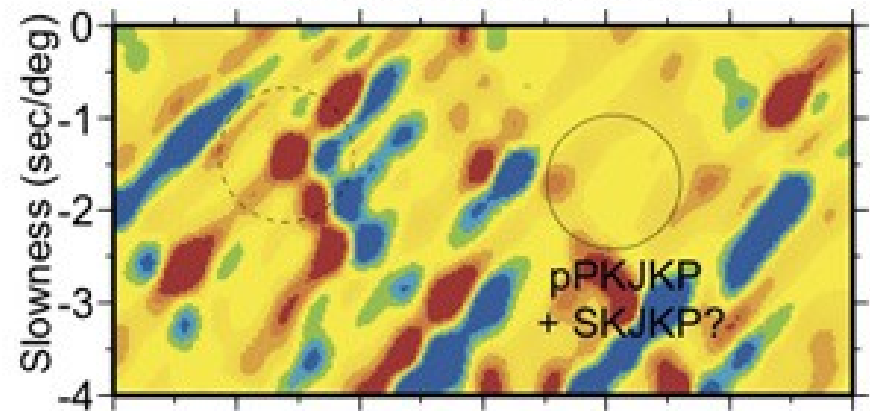


## Modelling interpretation

Modes solid inner core



Modes fluid inner core



# PKJKP

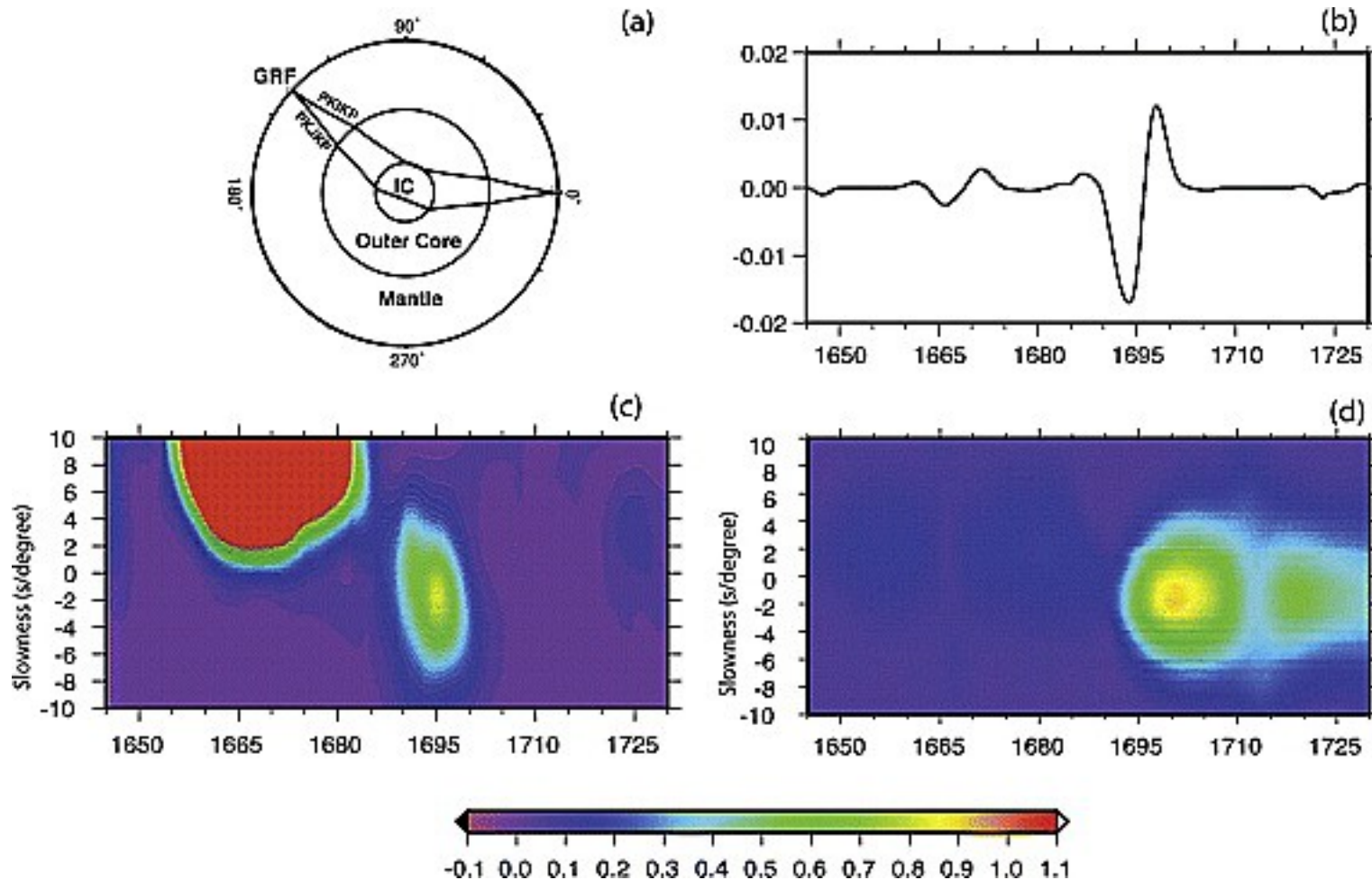


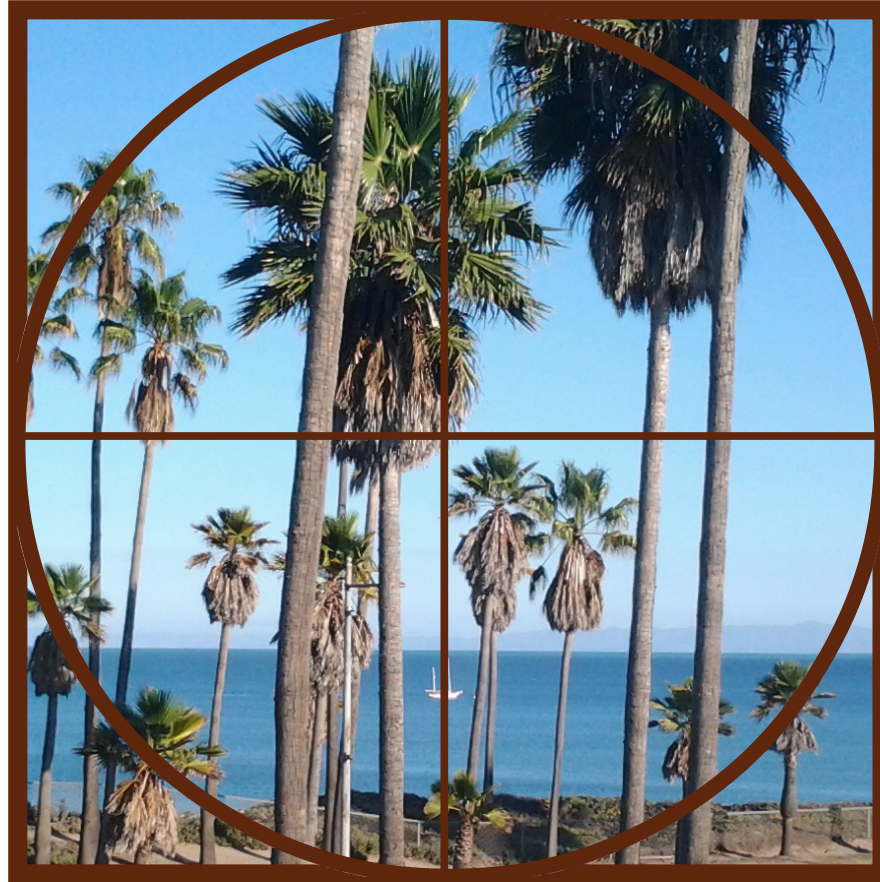
Figure 1. (a) Ray paths of PKJKP and PKIKP. The event epicenter and GRF seismic array are indicated by a star and a square, respectively. (b) Stacked waveform of PKJKP corresponding to the energy maximum in Figure 1c. (c) Observed vespagram for PKJKP in the slowness and travel time domain. The energy level is amplified 40 times. The slowness of the energy maximum is  $\sim -1.6$  s/deg, close to the PREM prediction of  $-1.43$  s/deg. The arrival time is also compatible with PREM (1695 sec for the maximum energy, compared to a prediction of 1690 sec for the high frequency onset of the pulse). (d) Synthetic differential vespagram. Both PKJKP and pPKJKP are visible after the interfering mantle phases have been removed. The estimated slownesses are both  $-1.4$  s/deg, which are the same as the predictions based on PREM [Dziewonski and Anderson, 1981].

# INNER CORE TRANSLATION



Animation courtesy of Zack Geballe and Elizabeth Day

# THE OUTER CORE



# THE OUTER CORE

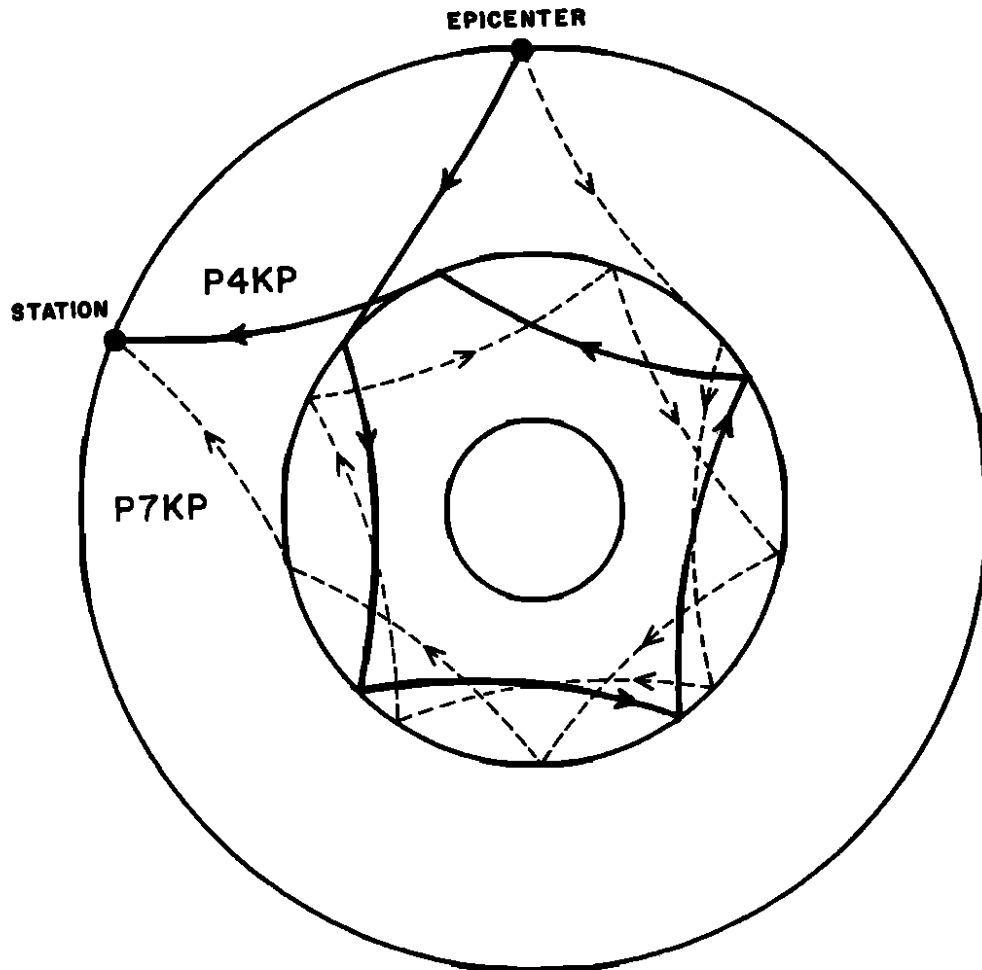


Fig. 1. Ray paths for *P4KP* and *P7KP*. Note that both rays emerge at an epicentral distance of about  $70^\circ$ .

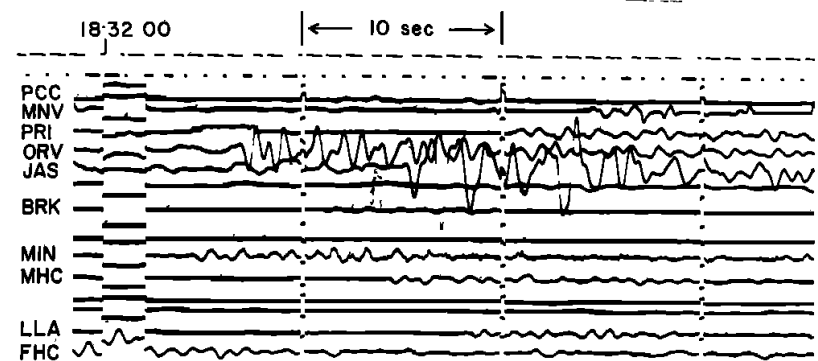


Fig. 3a. The *P4KP* recorded across the University of California Berkeley network from the Sea of Okhotsk earthquake. Distances to selected stations are PRI ( $61.1^\circ$ ), ORV ( $58.2^\circ$ ), JAS ( $59.9^\circ$ ), BRK ( $59.0^\circ$ ), and FHC ( $56.0^\circ$ ).

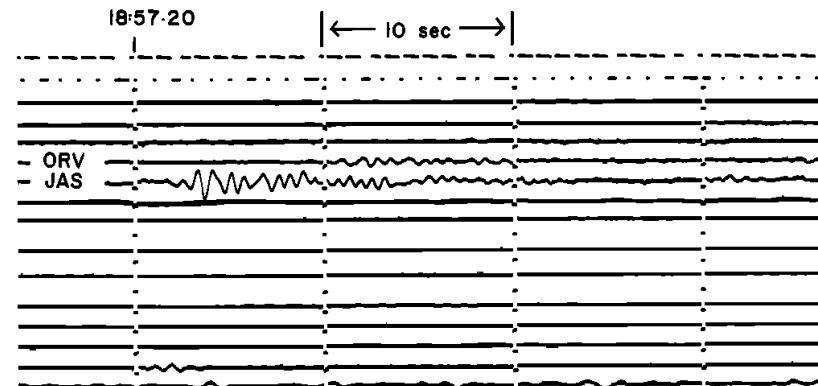
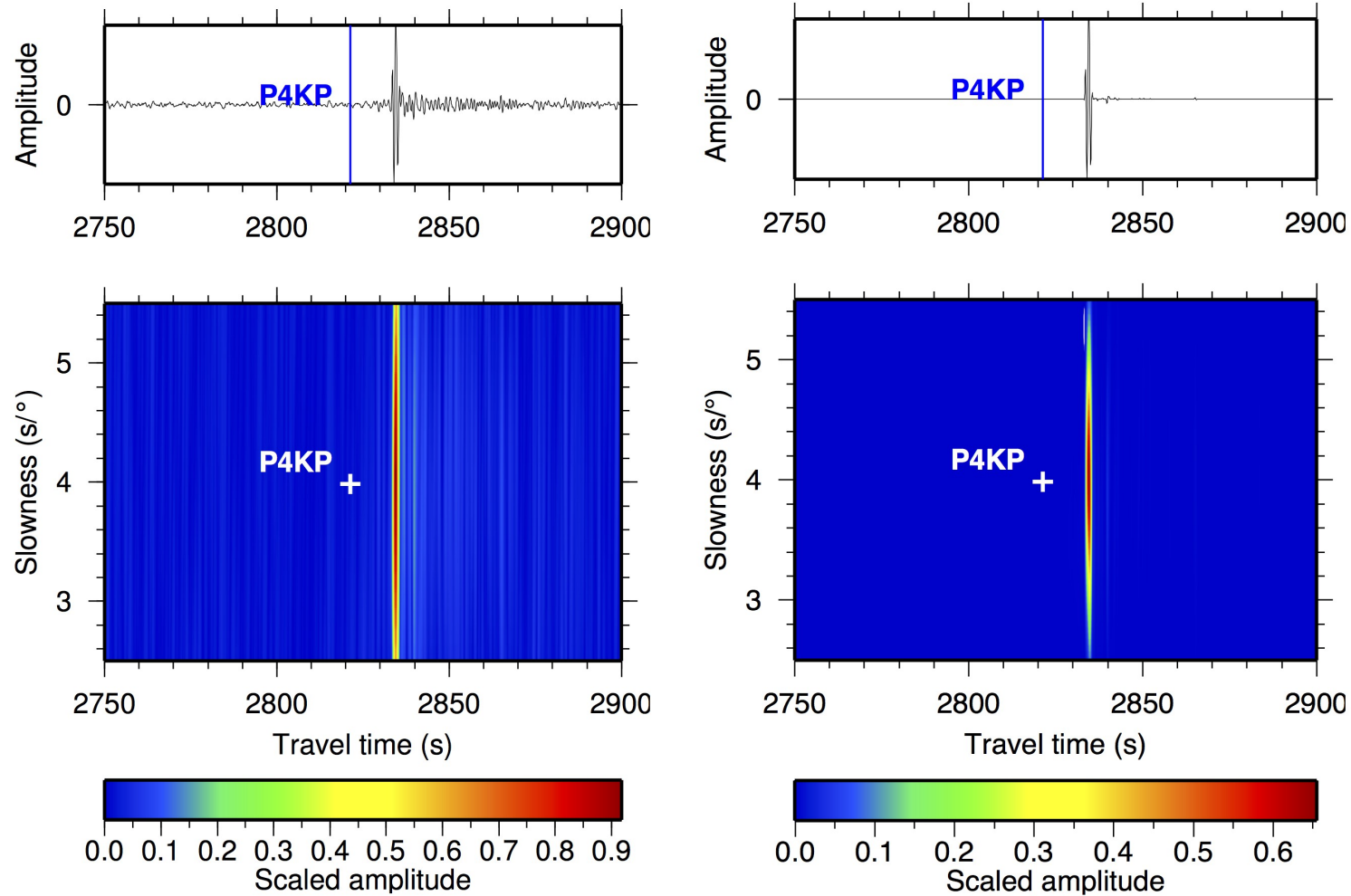


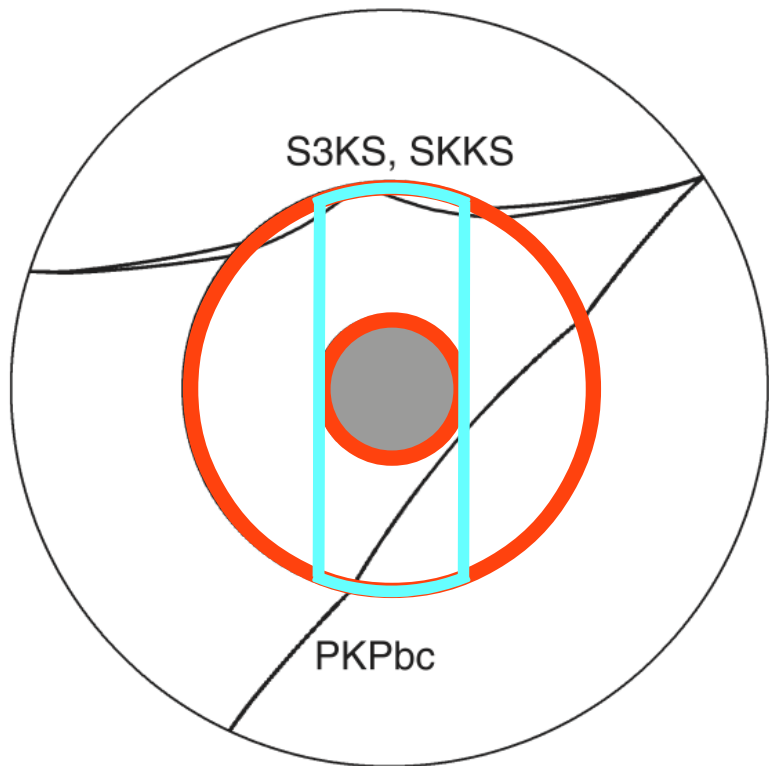
Fig. 3b. The *P7KP* at the Berkeley network from the Sea of Okhotsk earthquake.

# THE OUTER CORE

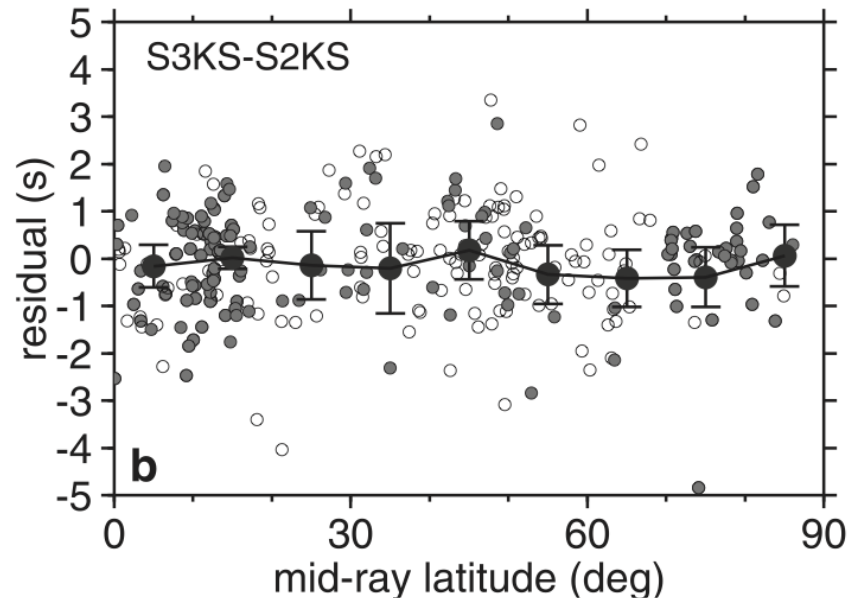


# THE OUTER CORE

Is there structure in the tangent cylinder?



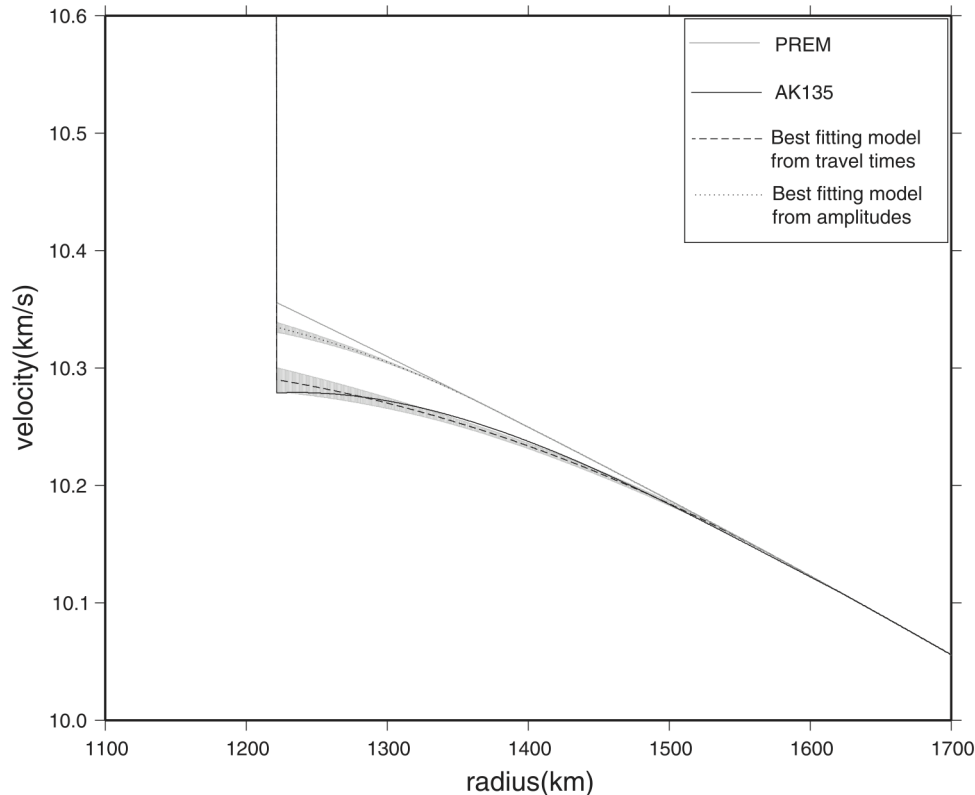
**Figure 1.** Scheme showing the phases used for the study of the liquid core: PKPbc, for the study of the structure inside the tangent cylinder; S3KS-SKKS, for the study of the polar caps.



**Figure 3.** Search for polar caps in the liquid core from S3KS-SKKS travel time anomalies. [...] (b) residuals [from PREM] after correction for the mean trend [as a function of distance], plotted as a function of the absolute value of the mid-ray latitude, and mean value inside  $10^\circ$ -latitude windows, with  $2\sigma$ -error bars. No anomaly can be detected near the poles or beneath the equatorial bulge.

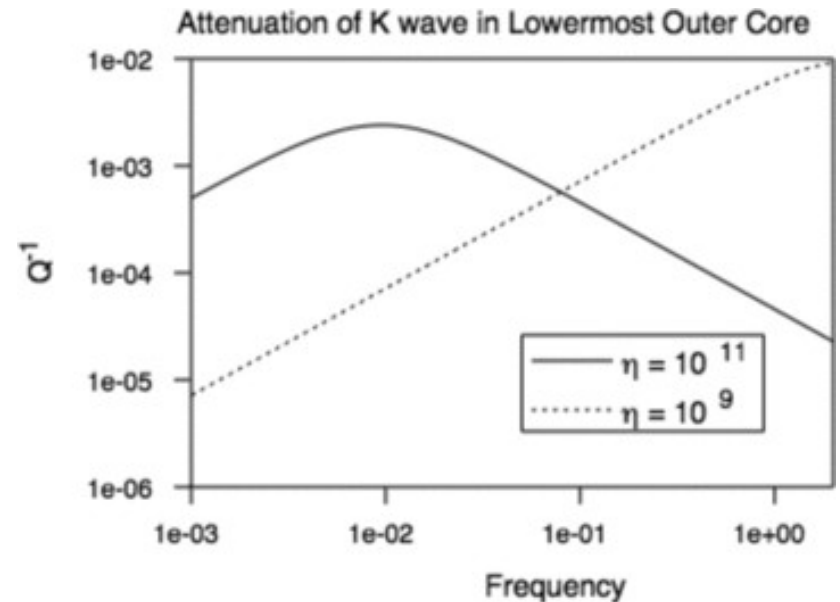
# THE OUTER CORE

Is there structure at the bottom of the OC? “F-layer”



**Figure 7.** The best fitting model from the differential times ( $PKP_{Cdiff} - PKP_{DF}$ ) and from the amplitude ratios ( $PKP_{Cdiff}/PKP_{DF}$ ). The top gray curve is for PREM, the bottom black curve is for AK135, the black dashed curve with gray shaded region is the best fitting model with one standard deviation from the differential times, and the dotted black curve with gray shaded region is our best fitting model with one standard deviation from the amplitude ratios with inner core  $Q = 400$  discussed in section 4.2.

Figure from Zou et al, *J. Geophys. Res.*, (2008).



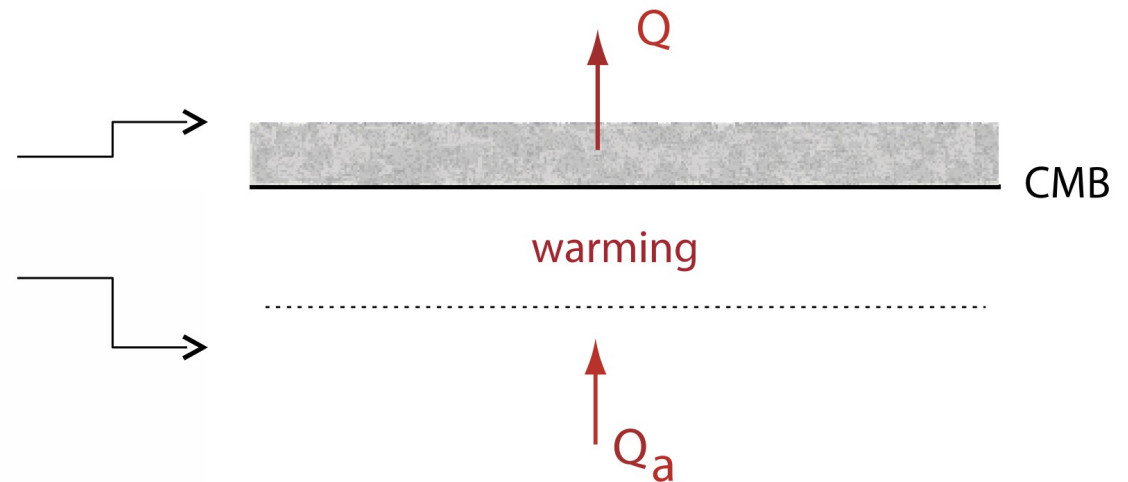
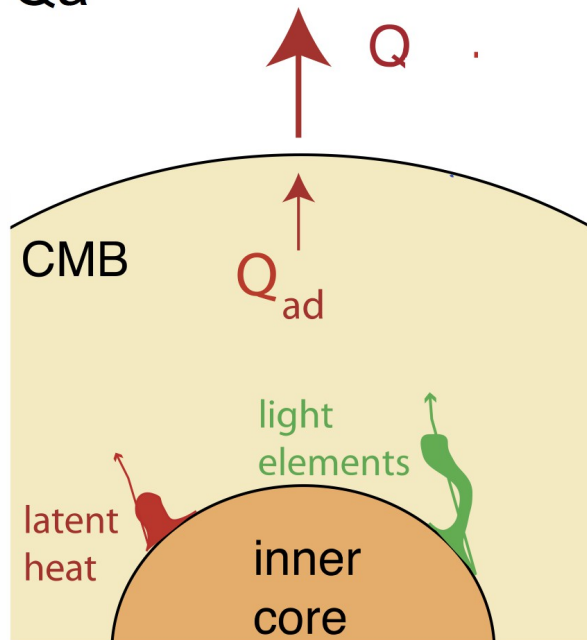
**Figure 4.** The viscoelastic attenuation factor predicted for compressional waves in the lowermost outer core from the  $\eta = 10^9$  and  $10^{11}$  viscosity models.

Figure from Cormier, *Geophys. J. Int.*, (2009).

(this slide taken from Bruce's lecture yesterday)

# Convection in the Core

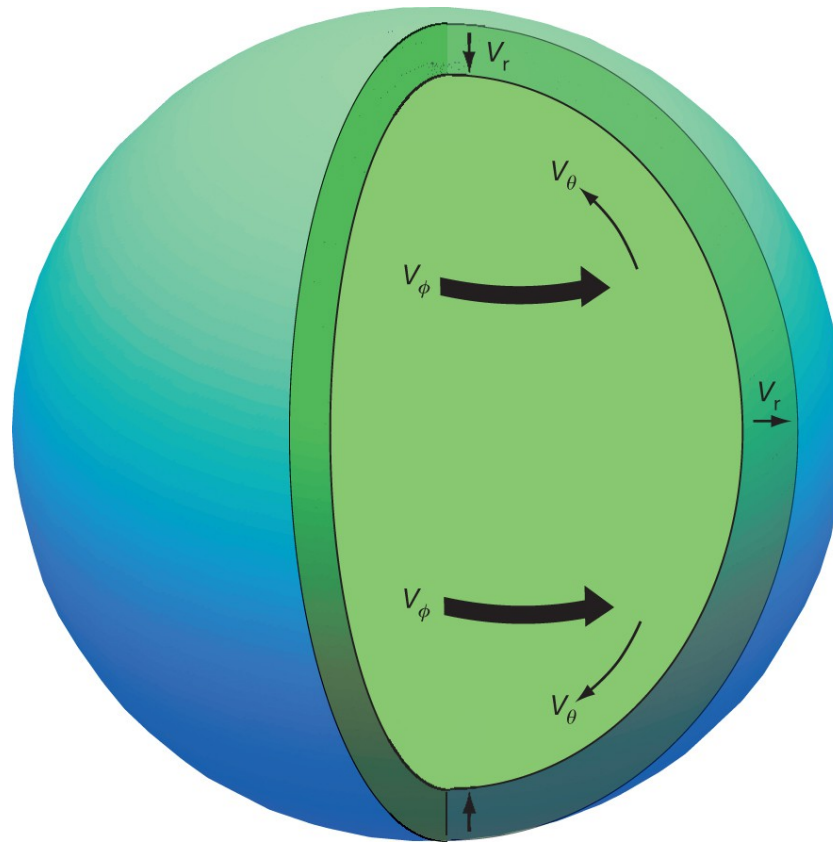
$$Q < Q_a$$



## Options

- i) compositional buoyancy mixes warm fluid
- ii) thermally stratified layer develops  
( -> compositional instability)

# THE OUTER CORE



Radial motion  $V_r$  causes a pressure perturbation, which drives an azimuthal flow  $V_\phi$  in the stratified layer. The presence of a radial magnetic field opposes  $V_\phi$  and induces a meridional flow  $V_\theta$ . The fluid velocities reverse direction over a full cycle of the wave.

# THE OUTER CORE

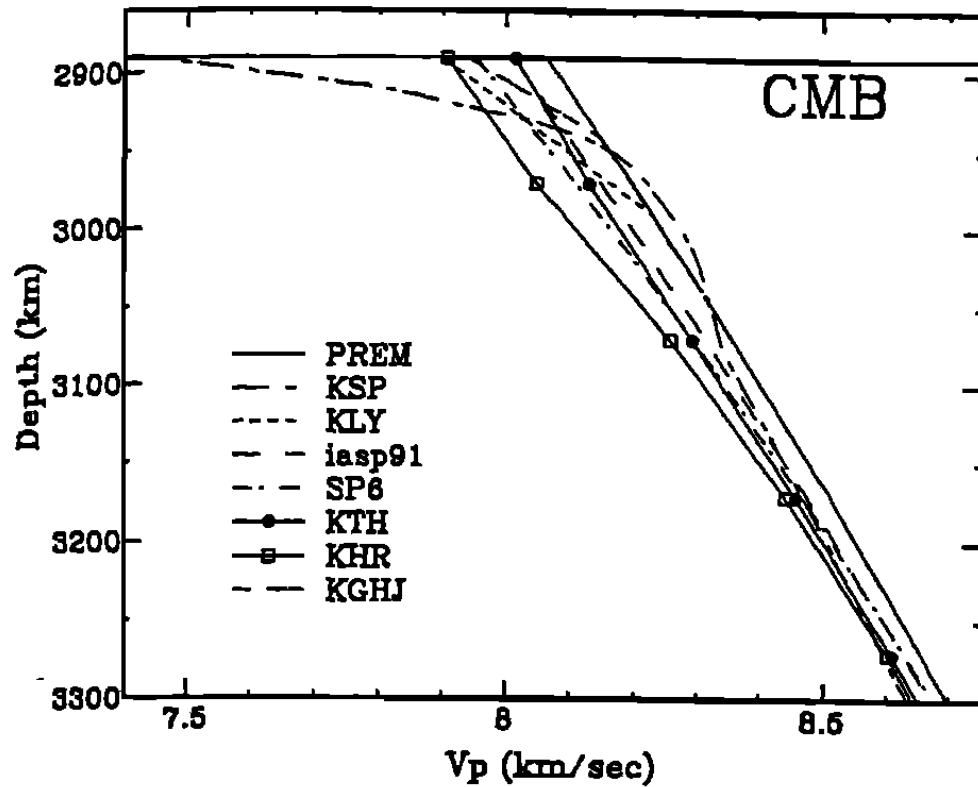


Fig. 4.  $V_p$  profiles of the outermost 400 km of the outer core. (Model names described in text).

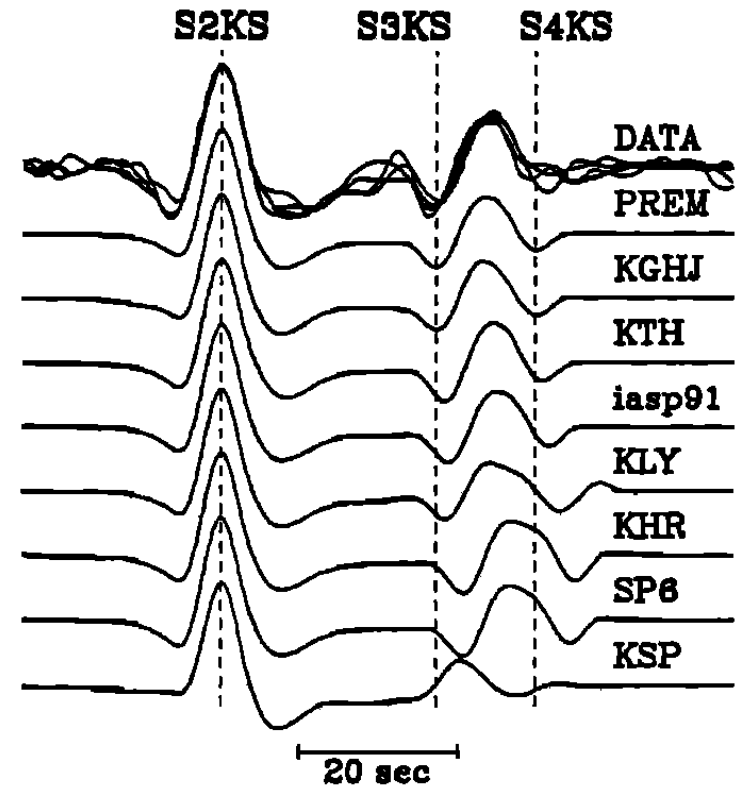
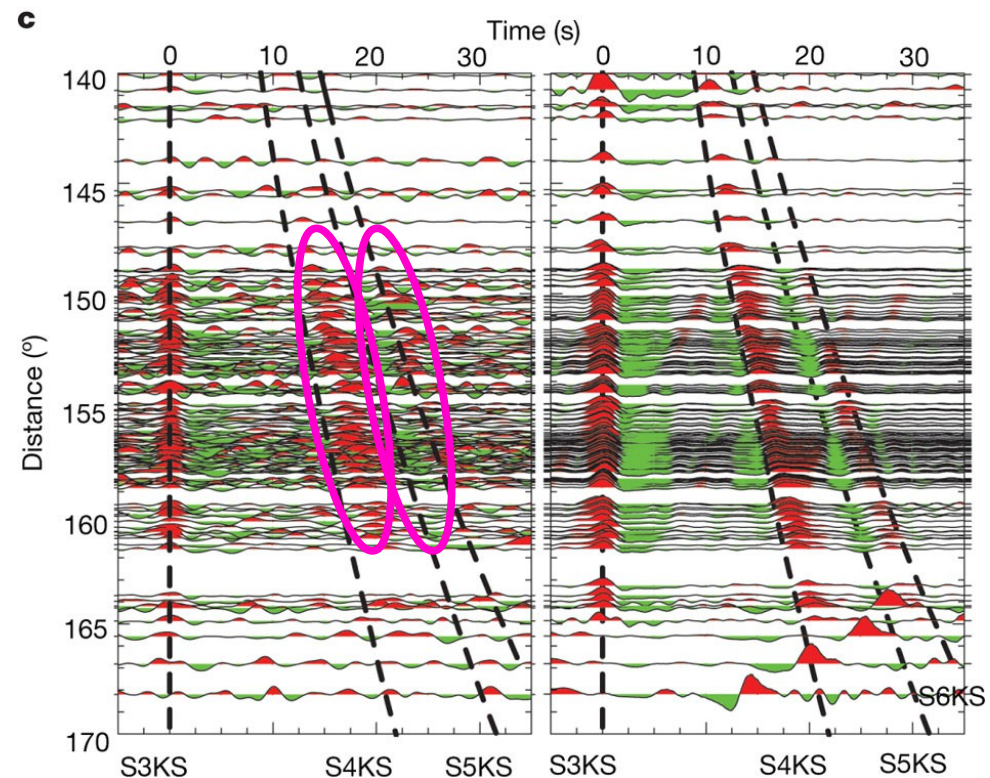
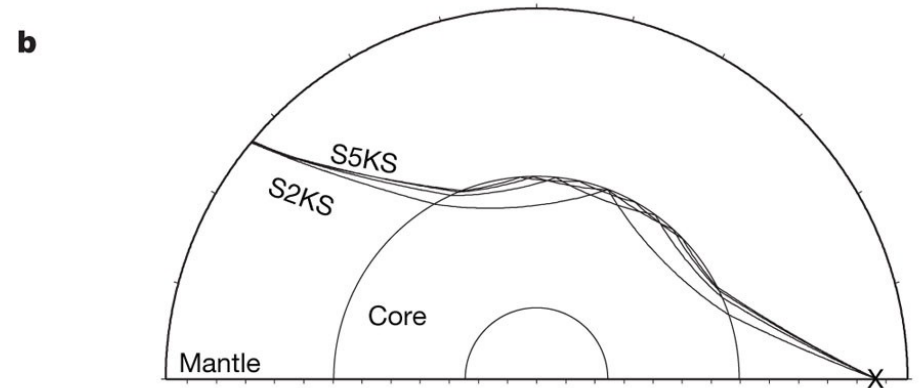
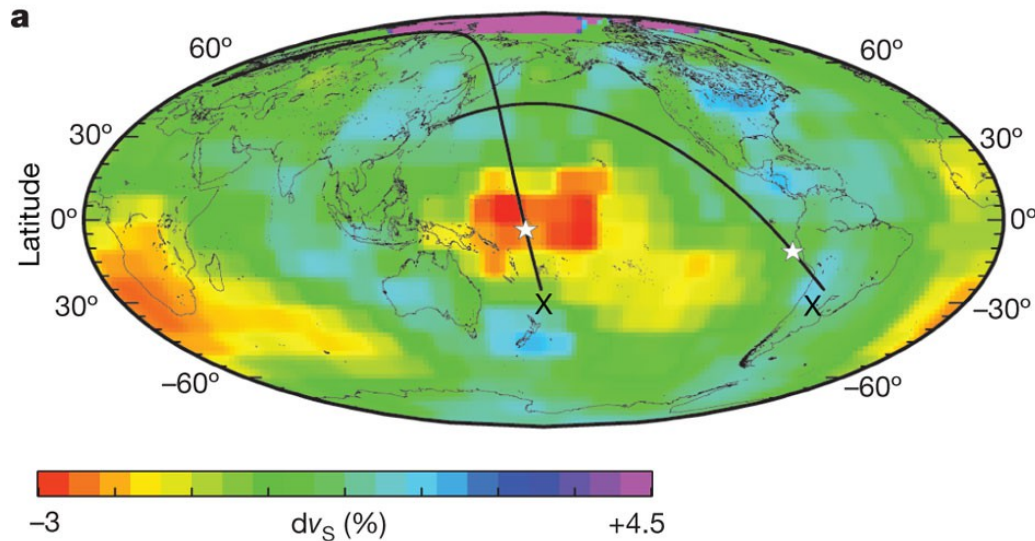


Fig. 5. Java Sea event data and synthetics near 141°.

# THE OUTER CORE



**a**, Sources (X) are subduction-zone earthquakes in South America (Argentina) and the southwest Pacific Ocean (Fiji) recorded by seismic arrays in Japan (~120 stations) and in Europe (~190 stations). The ray paths are superimposed on tomography maps (SB10L18) of shear-wave speed variations,  $dv_s$ , at 2,770 km in the lowermost mantle<sup>26</sup>. White stars indicate representative core entry points of S3KS. **b**,  $SmKS$  ray paths travel across the mantle as shear waves, but across the core as compressional waves. In the core, they reflect  $m - 1$  times from the underside of the CMB. **c**, Record section of observed (left, recorded by European stations) and predicted (right)  $SmKS$  arrivals from the Fiji earthquake. Arrivals and synthetics are aligned on S3KS (0 s), and the Preliminary Reference Earth Model<sup>13</sup> (PREM) predicted successive  $SmKS$  arrivals shown by dashed lines. Reflectivity synthetics for PREM (right) show that S4KS and S5KS are delayed. S2KS, which arrives before S3KS, is not shown, for clarity. PcPPKiKS is the prominent low-slowness arrival in the synthetics at 163–170°, not observable in the data.

# THE OUTER CORE

“The similarity of all admissible outer core models to PREM in terms of velocity and velocity gradient suggest that its underlying assumptions of homogeneity and adiabaticity are valid. This argues against the presence of an anomalous layer at the top of the core, as suggested in some previous studies.”

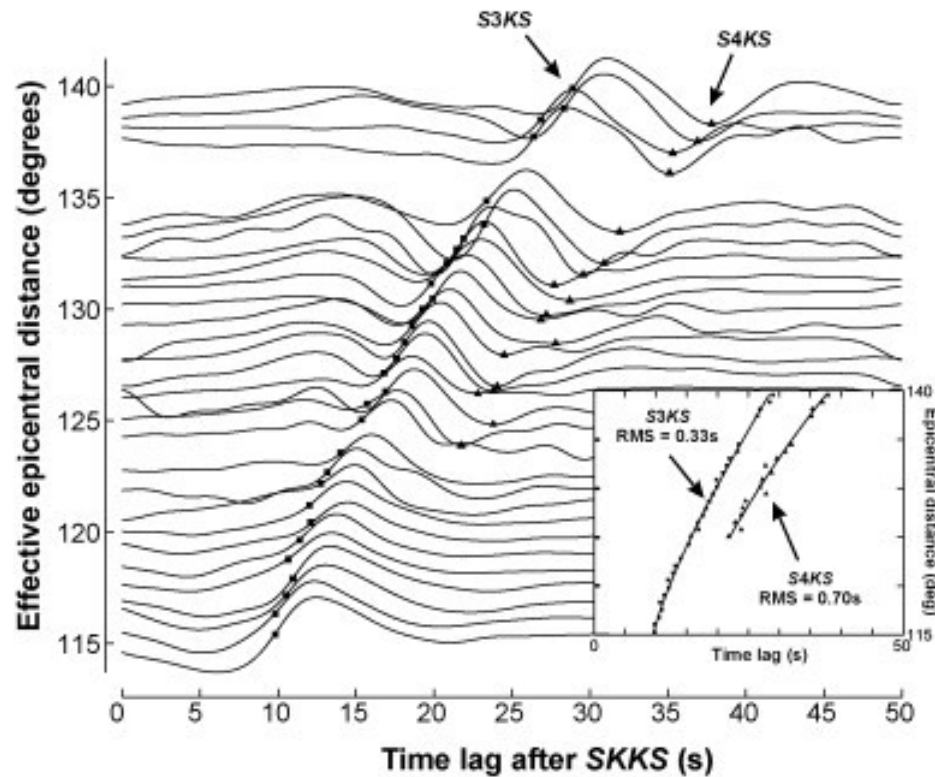


Fig. 4. Stacked empirical transfer function (ETF) profile. Epicentral distance is computed for a reference focal depth of 500 km. Symbols indicate arrival-time picks (snapped to waveforms) for S3KS and S4KS phases, relative to SKKS. Inset shows the fit of the derived moveout curves to these picks, along with the corresponding root-mean-squared (RMS) scatter for each phase. Errorbars are very small and indicate 98% confidence limits based on bootstrap resampling.

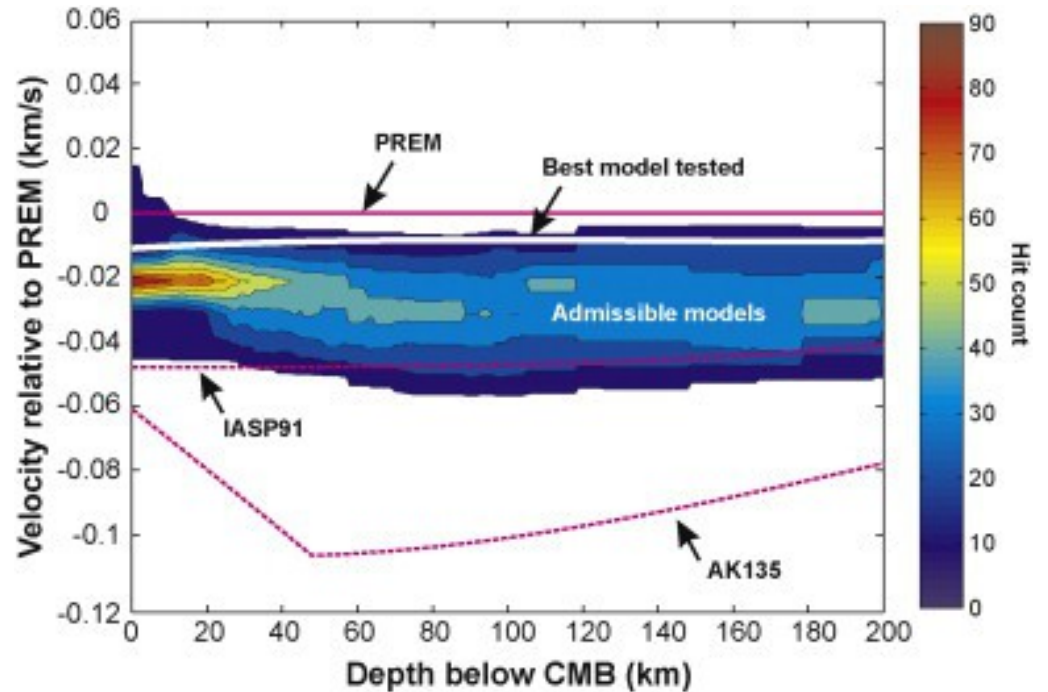


Fig. 7. Velocity models in the outermost core, plotted with respect to PREM. Admissible models (contoured region) are generally intermediate in velocity between IASP91 (Kennett and Engdahl, 1991) and PREM (Dziewonski and Anderson, 1981). The best model tested has velocity 8.05 km/s at the core–mantle boundary (CMB) and perturbation thickness 150 km, with a velocity gradient very similar to PREM. Model AK135 (Kennett et al., 1995) shows significantly lower velocity in the outermost core. Contours indicate hit count of the admissible velocity models for bins sized 0.01 km/s by 1 km sized bins.

From Alexandrakis & Eaton, *Phys. Earth Planet. Int.*, 2010